

ABSTRACT

KIETHER, WILLIAM JAY. Application of Sculptured Thin Film Technology to Metal Oxide Gas Sensors. (Under the direction of Dr. H. Troy Nagle.)

The main goal of this research has been the application of glancing angle deposition (GLAD) techniques to create highly porous sculptured thin films (STF) structures for use as gas sensors. The glancing angle technique utilizes physical vapor depositions at highly oblique ($>70^\circ$) angles of incidence to form porous film structures. Process conditions including the deposition rate, rotation speed, and flux angle were investigated to produce pillar and chevron formations.

Control of the anatase/rutile percentages in TiO_2 gas sensors is critical for design and development. Thin films were deposited using reactive e-beam evaporation with a titanium source melt at various partial pressures of oxygen and argon. Post deposition anneal studies were conducted in air from 150-900 °C. The combination of reactive evaporation at high oxygen partial pressures and low temperature (150 °C) anneals in air formed films with the highest percentage of anatase. Depositions at lower oxygen partial pressures yielded films with a higher percentage of rutile, which supports the role of oxygen vacancies as nucleation centers for the anatase to rutile transformation. Higher temperature annealing produced rutile films as expected from the thermodynamics of the TiO_2 system. After the formation of anatase STF structures, the films displayed a high degree of temperature stability during subsequent annealing. Anatase structures were still evident even after annealing at 1200 °C in air.

The GLAD technique produces films with preferred crystal orientations which differ based on the deposition angle. A series of experiments looked at the effect of the angle of incidence, the deposition conditions, and the substrate material on the crystal structure of the STF structures. The titanium films show a dependence of the crystalline structure on the angle of incidence for both as-deposited films and after oxidation at 900 °C in air.

A conductive MOS sensor was designed based on an anatase chevron formation. Following the fabrication of a sensor test chamber, the sensor response was characterized versus temperature for inert, oxidizing, and reducing atmospheres.

Application of Sculptured Thin Film Technology to Metal Oxide Gas Sensors

By
William Jay Kiether

**A dissertation submitted to the Graduate Faculty of
North Carolina State University
in partial fulfillment of the
requirements for the Degree of
Doctor of Philosophy**

ELECTRICAL ENGINEERING

Raleigh, North Carolina

2007

APPROVED BY:

Dr. C. Richard Guarnieri

Dr. John J. Hren

Dr. Richard T. Kuehn

Dr. H. Troy Nagle
Chair of Advisory Committee

Dr. John F. Muth

This dissertation is dedicated to my mother,

Joyce F. Kiether

You never gave up on me.

And to two people who inspired so many others their whole lives,

my father and his cousin,

Pastor W^m. J. Kiether (1922-1993)

Rev. Dr. Walter R. Wietzke (1922-2007)

BIOGRAPHY

William Jay Kiether was born on August 3, 1965 in Pittsburgh, Pennsylvania, a fact which explains his lifelong passion of the Steelers, Pirates and Penguins. He graduated in 1988 from Trinity University in San Antonio, Texas with a B.S. in Engineering Science with concentrations in electrical and mechanical engineering. He was a participant in the 1988 SERS internship at Argonne National Lab investigating the effects of large scale magnetohydrodynamics. After working with a defense industry consultant, he enrolled at North Carolina State University. He received a Master's of Science in 1995 with a double major in Electrical Engineering and Mechanical Engineering studying temperature control of rapid thermal chemical vapor deposition (RTCVD). Additional research interests include RTCVD uniformity and equipment development, cluster tool technology, and *in-situ* doping of semiconductor thin films. He has also worked for start-up companies in the fields of semiconductor dopant sources and atmospheric plasma systems. This doctoral degree culminates several years of work in the Electrical, Materials Science, and Biomedical Engineering disciplines.

ACKNOWLEDGMENTS

I wish to thank the following people for all the help and support throughout this endeavor as I chased my dreams:

First and foremost, my family for being there for me.

To Dr. Dick Kuehn and Dr. John Hren, thanks for sticking through to the end, the numerous discussions over the years, and the steady wisdom.

To Dr. John Muth, thanks for joining me for the last leg of the journey, the use of your lab, and the insights of a project manager on keeping the goals in perspective.

To Dr. J.P. Maria, thanks for allowing me carte blanche to use your lab and equipment. I could not have finished without your help, or that of your students. In terms of mixing both chemistry and accomplishment, you have the strongest group I have ever worked with.

To Dr. Dick Guarnieri, thanks for being the biggest factor in pushing me through to the end, the multitude of lab experience passed on, and teaching me the proper way to tell time (step one, learn how a clock works; step two, write it up or it didn't happen!)

To Dr. Troy Nagle, thank you for giving me the opportunity to finish, chairing my committee, all the guidance and support, and not giving up on me. I truly appreciate what you did to help me accomplish this goal.

To Chuck Mooney, Joan O'Sullivan, Joe Mathews, Stefan Ufer, Dr. Jerry Cuomo, and the rest of the NCSU laboratory staff and management, thanks for the opportunity to do an experimental thesis, the research at NCSU would be impossible without your tireless efforts and support.

To the students in RBII during my early days, thanks for sharing the initial fun.

To the students in JP's group, Cuomo's group, and Hren's group and the many others I have interacted with over the years, thanks for sharing the efforts and the later fun.

To Chris Oldham, for providing a bit of sanity through the toughest times.

And finally, to Dr. John Hauser: Although I was unable to get past all of the hoops and finish this when I should have, I will always owe you a debt of gratitude for giving me the initial opportunity, the tremendous experience of developing RTP-2 and the Cluster Tools, and most of all, teaching me what research is really about -- The courage and initiative to follow the data even when it doesn't lead down the path originally intended. The tangential paths are often the most rewarding.

TABLE OF CONTENTS

LIST OF TABLES.....	vii
LIST OF FIGURES.....	viii
1. Sensor Fundamentals.....	1
1.1 The Electronic Nose.....	1
1.2 Metal Oxide Sensor Fundamentals.....	2
1.3 The TiO ₂ Materials System.....	6
1.4 Goals of the Sculptured Thin Film MOS Sensor Development.....	7
2. Review Of Sculptured Thin Films.....	8
2.1 Summary of PVD Techniques.....	10
2.2 Evolution of Oblique Angle Deposition Techniques.....	19
2.3 Growth Dynamics of Sculptured Thin Films.....	31
2.4 Advanced Sculptured Thin Film Techniques.....	57
2.4.1 Capping Layer.....	57
2.4.2 Tilt Angle Manipulation.....	60
2.4.3 Phi Sweep Method.....	62
2.5 Conclusions.....	65
3. Morphological Control Of TiO ₂ Sculptured Thin Films.....	67
3.1 Introduction to Morphology.....	67
3.2 The Titania System.....	68
3.3 Titania Morphology Experimental Design.....	74
3.4 Titania Morphology Results and Discussion.....	76
3.5 Titania Morphology Conclusions and Future Work.....	89
4. Effect of Annealing On the Structure And Morphology Of STF Films.....	90
4.1 Introduction to Annealing.....	90
4.1.1 Annealing and Crystal Structure.....	91
4.1.2 Effects of Glancing Angle Deposition on Crystal Texture.....	94
4.1.3 Annealing Effects on STF Structures.....	96
4.1.4 Thermal Oxidation of Sculptured Thin Films.....	101
4.2 Annealing Experimental Design.....	105
4.3 Annealing Experiments Results and Discussion.....	109
4.4 Annealing Conclusions and Future Work.....	127
5. Sensor Formation Using Sculptured Thin Films.....	130

5.1 Titania Gas Sensors.....	131
5.2 Sculptured Thin Film as Gas Sensors.....	132
5.3 Sensor Design.....	141
5.4 Sensor Test Chamber.....	144
5.5 Sensor Materials Characterization.....	146
5.6 Sensor Electrical Characterization.....	148
5.7 Sensor Conclusions and Future Work.....	154
6. Conclusions and Future Work.....	157
6.1 Conclusions.....	157
6.2 Future Work.....	159
Bibliography.....	161

LIST OF TABLES

Table 2-1 Variable Nomenclature for Sculptured Thin Films	9
Table 2-2 The STF Formation With Respect To The Pitch.....	39
Table 3-1 Physical Properties of Anatase and Rutile.....	69
Table 3-2 Important TiO ₂ XRD Peaks	76
Table 3-3 Experimental conditions for the effect of oxygen partial pressure during deposition on subsequent rutile/anatase formation.....	82
Table 4-1 Primary Process Conditions for Annealing Experiment Depositions.....	108

LIST OF FIGURES

Figure 2-1 The four phases of PVD growth: Nucleation, Islanding, Channel Fill, and Continuous Film Growth	12
Figure 2-2 View of Structural Zone Model Morphologies.....	13
Figure 2-3 Examples of the Growth-Extinction Model	16
Figure 2-4 Effect of increasing the flux incidence angle on the tilt angle.....	18
Figure 2-5 The “Taga” Interface.....	23
Figure 2-6 SEM Images of “Blade” Structures.....	24
Figure 2-7 Film Density With Respect to Incident Flux Angle.....	26
Figure 2-8 First Thin Film Realization of a Helical Bianisotropic Medium	28
Figure 2-9 TiO ₂ Sculptured Thin Films Deposited By The Author In The BMMSL Evaporation System	29
Figure 2-10 Successful (top panel) and unsuccessful (lower slide) attempts to create a contiguous capping layer.....	30
Figure 2-11 Tilt Angle Variations for Different Materials	33
Figure 2-12 Effect Of Pressure On The Tilt Angle.....	36
Figure 2-13 STF Structures as a Function of the Pitch.....	40
Figure 2-14 Evaporated (top) and Sputtered (bottom) GLAD Films	42
Figure 2-15 Effect of competition on GLAD pillars grown on unseeded substrates.....	44
Figure 2-16 PSD Function Curves For Deposited And Simulated Films.....	46
Figure 2-17 Scaling Behavior Of The Column Broadening In STFs	49
Figure 2-18 Column Radius as a Function of Column Height	50
Figure 2-19 Shadowing Length Illustration.....	52
Figure 2-20 Shadowing During The Initial Growth Stage For Proper Seed Spacing.....	53

Figure 2-21 Simulation Of The Film Density With Respect To (A) Seed Period And (B) Flux Angle	56
Figure 2-22 Pillar Widening With Respect To Seed Period.....	56
Figure 2-23 Humidity Sensor with Capping Layer.....	59
Figure 2-24 Well Defined Capping Layer Atop Porous Films.....	59
Figure 2-25 Tilted Nano-Rods Grown Using The Angular Sector Method	62
Figure 2-26 SEM images of Phi Sweep Films.....	65
Figure 3-1 SEM Images of Titanium STF Columns.....	77
Figure 3-2 XRD For 500nm Ti Films Deposited At 10^{-6} Torr With Subsequent Annealing ..	78
Figure 3-3 XRD Graphs For 100nm TiO Films Deposited At 10^{-5} Torr With Subsequent Annealing	79
Figure 3-4 SEM Images of TiO _x STF Pillar Structures	80
Figure 3-5: XRD Values for the As-Deposited TiO _x Pillars.....	85
Figure 3-6: XRD Values for TiO _x Pillars after 450 °C, 5 Minute Anneals	86
Figure 3-7: XRD Values for TiO _x Pillars after 650 °C, 20 Minute Anneals	87
Figure 3-8 XRD Values for TiO _x Pillars After 900° C, 5 minute anneals.....	88
Figure 4-1 TEM of MgO Nanocolumn Deposited Using the GLAD Techniques.....	95
Figure 4-2 Temperature Programmed Desorption Spectra	99
Figure 4-3 XRD Profile of Normal Profile and STF Tungsten Formations	101
Figure 4-4 XRD Patterns For Pillars Deposited On Glass Substrates – As-Deposited	111
Figure 4-5 XRD Patterns for TiO _x (A) Pillars and TiO _x (Ru) Pillars for Various Annealing Conditions in Air.....	114
Figure 4-6 XRD Patterns For TiO _x (Anatase) Pillars Stabilized By 1 Hour Anneal At 450 °C In Oxygen And Subsequently Annealed For 1 Hour At Higher Temperatures In Air.....	117

Figure 4-7 XRD Patterns For TiO _x (Anatase) Pillars Stabilized By 1 Hour Anneal at 450 °C In Oxygen And Subsequently Annealed For 1 Hour At Higher Temperatures In 5% H ₂ /N ₂ Forming Gas	118
Figure 4-8 XRD Pattern Of Ti Depositions For Various Flux Angles And Substrates.....	120
Figure 4-9 XRD Patterns Of Ti Depositions After 900° C Anneals In Air For Various Flux Angles And Substrates	122
Figure 4-10 SEM Images of Ti Pillars Deposited at Various Flux Angles on Si(100)	125
Figure 4-11 SEM of Ti Pillars After 900°C Annealing	126
Figure 5-1 Open Vertical Post Capacitance Humidity Sensor Fabricated by Increasing the Angle of Incidence	133
Figure 5-2 Vertical Post--Capping Layer Capacitance Humidity Sensor (a) SEM Image (b) Humidity Response.....	136
Figure 5-3 Conduction Anisotropy Test Structure.....	139
Figure 5-4 Conduction Anisotropy Demonstrated By The Directional Dependence Of The Chevron Films Resistivity	140
Figure 5-5 Mask Designs for the Sensor Strip Area and the Contacts for 2” Wafers	144
Figure 5-6 Design of Sensor Test Chamber.....	145
Figure 5-7 SEM Images of Chevron Formation	147
Figure 5-8 SEM of Anatase Chevron Formation.....	149
Figure 5-9 XRD Patterns For Four Layer Chevron Formation Used For The Alpha Sensor	150
Figure 5-10 Resistance (MΩ) versus Temperature (°C) Data at 1.0 μA for Alpha Sensor in Air	155
Figure 5-11 Resistance (MΩ) versus Temperature (°C) for Sensor Alpha in Argon at 1.0 μA	156

Chapter 1

Sensor Fundamentals

Ah, Smell!!! This most ubiquitous of the human senses, a marvel of organic engineering has proven to be perhaps the most difficult human sense to duplicate in cybernetics. The human nose is a fantastic sensor capable of selectively distinguishing between billions of individual smells. Odorous molecules are typically volatile organic compounds (VOC's) that have molar masses ranging from 30 to 300 daltons.[1] The nasal passages are lined with cells which react to these VOC's. The nose consists of an immense array of these individual cells (sensor) which transmit their responses (signals) to the neurons which carry the combinations of these responses (data manipulation) along the neural pathways to the large neural net (brain) where the individual smells are extracted and classified.

1.1 The Electronic Nose

The development of an electronic equivalent of the nose (e-nose) holds great potential across many applications. Presently, the impetus is not in the area of human sensory enhancement (ala the hearing aid), but to provide a way of monitoring a specific area for changes in odor concentrations or components. In this case, the e-nose is closer in scope to the CCD video system. The response of a large array of individual sensors is processed until a complete image can be formed and stored electronically. Areas where e-nose or airborne chemical sensor technology is presently employed include monitoring the quality of potable water,

identification of illness, determining the quality of foods, identifying infectious disease microbes, explosives identification, and numerous other uses.[2-5]

The e-nose development has four distinct levels on which research opportunities exist: Physical Sensor Development, Measurement Techniques, Data Manipulation, and Feature Extraction. At the most basic level, the initial signals are generated by individual sensors. The physical sensor development includes such areas as sensor design, layout, materials systems, material structure/morphology, sensitivity, selectivity, etc. At the next level are the measurement techniques used which include flow patterns and modulation; conduction, capacitance or impedance measurements; temperature modulation; optical transmission, etc. Once a raw electrical signal has been generated, data manipulation handles the amplification, analog/digital conversion, compensation/filtering, and digital signal processing. Finally, at the highest levels (the brain, if you will) of the e-nose system, individual features of the signals are extracted and classified. An example of this would be recognition of a spike in CO concentration or change in humidity.

1.2 Metal Oxide Sensor Fundamentals

The thrust of this research “Application of Sculptured Thin Films to Metal Oxide Sensor Technology” is concentrated on the most basic level: Physical Sensor Development. At present, most gas sensors are fabricated using either semiconducting metallic oxides (MO sensors) or conductive polymers (CP sensors). The MO sensors use either thick, sintered

ceramic films or more recently thin films ($<5\mu\text{m}$) using integrated semiconductor technology. At this point, the thick film sensors are far more prevalent commercially. But the thin-film technology holds significant potential, especially in developing smaller devices and integrating these devices into more complex sensor arrays. In general, thick film sensors are easier to manufacture and have shown better sensitivity than most thin-film sensors.[6] One reason for the enhanced sensitivity in thick films is related to the greater porosity of the thick films. The sensing process in MO sensors is primarily a surface response, and therefore greater surface area directly affects the sensitivity of the sensor. Recently, the ability to deposit thin films with a highly porous microstructure has been demonstrated.[7, 8] These sculptured thin films can easily be fabricated using metal oxides, and provide the impetus for this research.

A brief review of sensor fundamentals is useful at this point. Several factors define the quality of any sensor. One key characteristic is the sensor response time. The response time is important not only in the initial response to an impulse, but also in the recovery time when the initial conditions are returned. Hysteresis is the term applied when the reaction and recovery paths are different in either time or magnitude. Although there are situations where hysteresis can be beneficial, an ideal sensor would have extremely fast response times with little or no hysteresis. Reproducibility is also a critical sensor parameter. With the highest level e-nose systems, the detection of specific odorants (especially in complex chemistries) depends on consistent feature identification. Without a reproducible response, these advanced classification methods are difficult to implement. Two additional factors critical to define sensor response are the sensor sensitivity and the sensor selectivity.

Sensitivity is usually defined as the change in a measurable quantity/calibration measurement, or in most MO sensor measurements as $\Delta R/R_{\text{Initial}}$. In most cases, the highest possible sensitivity to the change in the target gas concentration is desired to easily identify the signal. However, due to the simplicity of the MO sensor conductivity response, it is often hard to distinguish between different gas components or mixtures simply from steady-state resistance measurements. The masking of a signal from the desired gas due to the reaction with common other gases is called “poisoning”. Selectivity is the ability to distinguish and modify the response of individual gas components. One method of selective design is to decrease the sensitivity to a common “poisoning” agent (*e.g.* CO in measurements for NO₂ in engine exhaust), while increasing the sensitivity of the target gas.

The metallic oxides used in MO sensors generally act as defect semiconductors. Vacancies, defects, metal interstitials, and other generation/recombination centers participate in conduction as acceptor or donor sites. The conduction process is similar to that in doped semiconductors, except that a broad range of energy levels (barrier heights) exists, and the conduction centers are not uniformly distributed across the material (variable range). The most widely characterized MO material is SnO₂, or stannic oxide, which acts as an n-type material. As in all conduction processes, temperature plays an important role. At the most basic level, the key to using these materials as gas sensors lies in the surface adsorption of oxidizing or reducing gas species. At low temperatures oxygen chemisorbs on the sensor surface as an O₂⁻ ion, extracting an electron from the SnO₂ substrate, which creates a positively charged donor site in the film. Since SnO₂ is n-type, this action decreases the

number of majority carriers (electron) and thus increases the resistance. When higher concentrations of oxidizing gas species are present, or when oxidizing species with greater charge density (O^- or O^{2-}) are present (generally at higher temperatures), then the resistance is increased further. When reducing gases (CO , H_2 , etc.) are present, they can react with the chemisorbed oxidizing species, which returns the electron to the substrate. Therefore, in the simplest model, the change in conductance is controlled by the amount (surface coverage) and type of chemisorbed oxidizing species, tempered by the reactions with any reducing gases.

The material structure of the MO film plays an important part in the sensitivity of the gas sensors. Grain size, surface roughness, etc. affect the conduction through the scattering mechanisms. More porous films have a larger surface area, more surface sites for gas adsorption, and therefore, display a higher sensitivity. These effects are similar in most materials, however, and structural composition is usually related to (and controlled by) the fabrication techniques (deposition method, sintering temperature, etc.). Control of the structure is often used to modify the sensitivity and selectivity of the MO sensors. The sticking coefficients of the various gases vary significantly with surface of the sensor. These effects can be manipulated by adding a surface dopant, changing the crystallographic structure, and other techniques.

1.3 The TiO₂ Materials System

The TiO₂ materials system was chosen as the metal oxide semiconductor (MOS) material for this research. Titanium oxide has two distinct polymorphs in the anatase and rutile phases which have been used in gas sensor technology.[6, 9-13] The two phases have distinct materials properties which contribute to their usefulness as a gas sensor. Control of the anatase/rutile percentage in the thin films is critical to the design and application of the sensor. Recently, nano-scale titania sensors have demonstrated very high sensitivity to hydrogen and simple alcohols.[11, 13] In addition, the gas sensing properties of the rutile phase show a dependence on the crystal orientation of the thin films.[10] The sculptured thin film technology can be used to create nano-scale features with excellent control of feature size, and the crystal orientation can be influenced by the deposition parameters.[14, 15] Therefore, the sculptured thin film techniques are ideally suited for investigating novel gas sensor designs with the titania materials system.

1.4 Goals of the Sculptured Thin Film MOS Sensor Development

The overall goals of this research can be summarized by the following bullets:

- Develop and characterize the ability to deposit sculptured thin films at North Carolina State University
- Develop process conditions to control the anatase/rutile morphology in titania sculptured thin films
- Identify the effects of annealing/oxidation on the nano-scale sculptured thin films.
- Design and fabricate a titania-based gas sensor using sculptured thin films.

Chapter 2

Review of Sculptured Thin Films

The trend toward nano-scale engineering has led to many new opportunities for creating custom structures on this level. One of the most promising methods uses the growth dynamics present in highly oblique angled physical vapor depositions to produce Sculptured Thin Films (STFs).[7, 8, 16-20] The overall goal of this research is to use sculptured films to fashion Metal Oxide Semiconductor (MOS) gas sensors with improved sensitivity and selectivity through increased surface area, tailored shapes and porosity, and more precise control of surface chemistry. This chapter will present four sections related to depositing STF's. The first section provides a brief summary of the physical vapor deposition (PVD) process and gives an overview of how surface diffusion and localized shadowing contribute to void or “defect” formation in the deposited films. The second section traces the evolution of glancing angle PVD techniques, and the requirements to produce simple nanometer scale structures such as pillars, helices, and chevron formations. The third section explores the STF growth dynamics in detail and describes how conditions can be manipulated to control film properties such as porosity, spacing, birefringence, and surface area. The final section details how an improved understanding of these concepts has led to advanced techniques that can form more complex features and sensor structures.

The nomenclature of the obliquely deposited film technology is quite varied due to the large number of groups using similar techniques. This variation applies to the overall descriptions

and names of the techniques; the nanostructured films themselves, and the deposition parameters. Therefore, it is necessary to define the nomenclature that will be used here. The most widely used name for the oblique deposition technique is “GLancing Ange Deposition” or GLAD coined by Robbie, *et al.*[8] The groups of structures created by GLAD techniques are best described as Sculptured Thin Films or STF’s.[21] Table 2.1 contains a partial list of the deposition parameters and corresponding symbols used in this report.

Table 2-1 Variable Nomenclature for Sculptured Thin Films

Deposition Parameter	Symbol	Description
Deposition Angle	α	Angle of the substrate surface incident to the deposition flux (deg)
Rotation	ω	Revolutions per sec
Pitch	p	Deposition during one rotation (nm)
Column Tilt Angle	β	Mean angle of column growth (deg)
Column Diameter	d	Mean diameter of columns at a specified height (nm)
Column Separation	a	Mean spacing of aperiodic deposited columns
Seed Separation	δ	Distance between seed sites for periodic seeded substrates
Deposition Rate	r	Normal incidence deposition rate (nm/sec)
Column Height	z	Column height (nm)

2.1 Summary of PVD Techniques

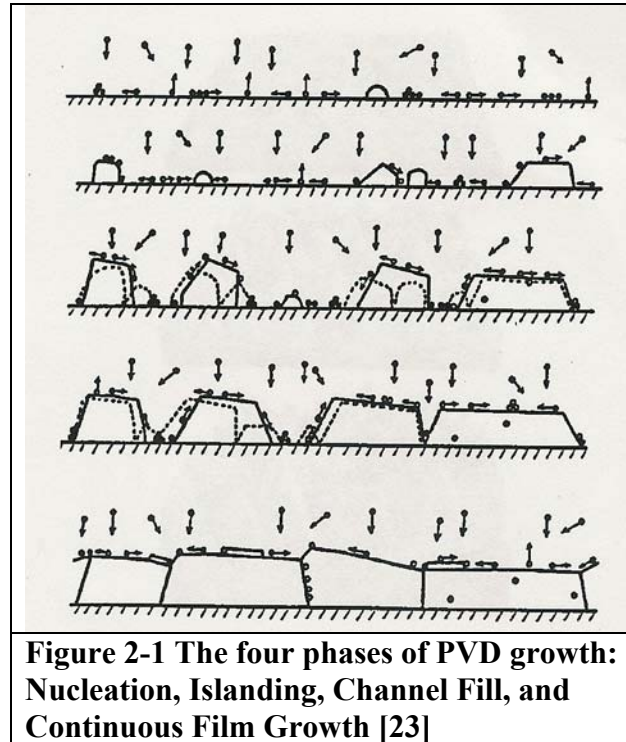
The growth dynamics for physical vapor deposition techniques such as electron beam (e-beam) evaporation and magnetron sputtering have been widely studied due to the many applications to thin film processing. However, a very basic understanding of these techniques is necessary to begin the discussion of sculptured films. In e-beam evaporation, an electron gun is used to melt a source material contained in a metallic crucible. Since the melt occurs under high vacuum conditions (typically $<10^{-6}$ Torr), the melting source material has sufficient vapor pressure for a significant flux of the material to evaporate and move through the deposition chamber. The e-beam is swept across the source surface in order to maintain an even melt of the source material and as a way of controlling the flux (deposition rate). When these groups of atoms of source vapor come into contact with another surface, *i.e.* the substrate, shielding, chamber walls, *etc.*, the vapor essentially condenses on these colder surfaces and accumulates into a thin film. For a non-noble metal source material, the vapor can also react with components (oxygen) in the background atmosphere or at the surface and form compounds or oxides. If this process occurs in a significant fashion, it is referred to as a reactive deposition.

A key aspect during the flight of the evaporated material concerns the degree of collimation in the flux. The vapor flux leaves the source melt with a wide angular distribution. As the distance increases from the source to the substrate, the solid angle of the flux trajectories that

impinge on the substrate becomes smaller. The flux trajectories are therefore closer to parallel (more collimated). In addition, at lower pressures the mean free path between vapor particle collisions (scattering events) becomes longer, which also leads to greater collimation at the substrate. The need for a highly collimated flux to create sculptured films will become apparent in subsequent sections.

For most films deposited on non-ionic substrates, the growth process consists of four main stages: nucleation, islanding, channel filling, and continuous film growth.[22] The vapor particles are either reflected by the surface or undergo physical adsorption. When they are physically absorbed, the absorbed atoms (or adatoms) move across the surface in a process known as surface diffusion. At this point the adatoms can desorb (return to the gas phase), become pinned on the surface, or collide with other adatoms or groups and form nuclei. As the nuclei become larger, their rate of movement or mobility decreases. Once the nuclei reach a critical size, it is highly probable that they will become pinned to the surface and provide an anchor for other adatoms to conglomerate. As the pinned nuclei grow in size, they appear as islands on the substrate surface. Initially, these islands are widely scattered across the substrate, but continue to increase in size and number and appear more like an archipelago. The gaps between these islands eventually decrease and take on the appearance of channels or voids. When these channels are filled in (covered over), continuous film growth develops. Since the size, shape, and energy of the adatom groups reaching a particular channel are all random factors, these channels do not fill in an organized manner. Some are only partially filled before the top of the channel is covered over, leaving voids in the film. In other words, void formation is directly related to shadowing as some adatom

formations effectively screen or shadow areas of the channel from the incoming flux. The islanding and channel formation process leads to the creation of columnar grains and voids (defects) in the films. A widely used illustration of these four phases of PVD films growth is shown in Figure 2-1.



A significant portion of the work in PVD development has been to minimize the amount of grain boundaries and voids to produce high quality epitaxial films. However, amorphous and polycrystalline films also have many applications where the properties associated with the film microstructure are important. One key factor in describing the microstructure is the morphology, or the size and shape of the crystals. A methodology known as Structural Zone Modeling (SZM) has been developed to relate the morphology to various deposition

conditions. One widely used model developed by Movchan and Demchisin relates the dependence on the morphology to the ratio of the substrate temperature during deposition, T_s , and the melting temperature of deposition material, T_m . [24] This ratio provides a general qualitative value for the mobility of the adatom. As the ratio increases, so does the mobility of the adatom. The model was originally based on experimental results using e-beam evaporation for relatively thick ($>25 \mu\text{m}$) films. Three distinct regions or structural zones (Zones I, II, and III) can clearly be defined from their observations based on the T_s/T_m ratio. Subsequent works have identified an additional zone (Zone T) and investigated the effects of sputtering, deposition pressure [25], thinner films, ion bombardment [23, 26], and impurity incorporation [27], but the current models are based on the original concepts. Figure 2-2 provides a cross-sectional view of SZM morphologies.

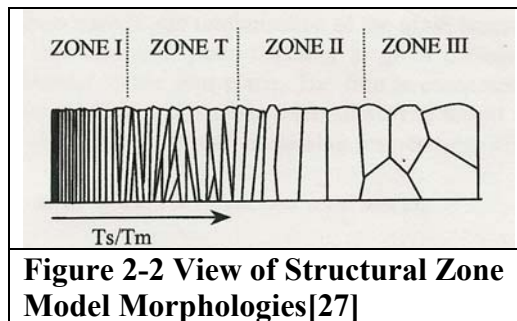


Figure 2-2 View of Structural Zone Model Morphologies [27]

Zone I has the lowest mobility range ($0 < T_s/T_m < 0.2$). The values that define the ranges have some material dependence. For example, metals transition at slightly higher values than the ones for oxides used in this document. [22] In this zone, the amount of surface diffusion is small and bulk diffusion is virtually non-existent. Therefore, the shadowing effects dominate the structure formation. Randomly distributed column placement, and random size, multiple

crystal textures, and rough surfaces characterize this zone. Grain sizes are small and the films are mostly amorphous or polycrystalline. The films have random textures as the crystal growth mirrors the initial orientation of the various nuclei. With the low adatom mobility, many voids are formed due to incomplete filling of the channels. Zone I produces films which are less dense than in the other three zones.

As the ratio moves into the Zone T regime ($0.2 < T_s/T_m < 0.35$), surface diffusion becomes the dominant factor. Although shadowing still occurs, the adatoms on average move greater distances before becoming pinned at a nucleation site. In simple terms, the adatoms are more likely to fill in gaps between the columns and voids caused by shadowing. In addition, the films are not homogeneous from the substrate to the surface. Near the substrate, the films have a similar appearance to the small columns in Zone I. However, a competition for growth between the columns leads to fewer and fewer columns which continue to grow as the film thickness increases.

Columns with different texture present different facets toward the vapor flux. These facets have different surface energies, and thus different surface diffusivities. The increased surface diffusion leads to this growth competition by favoring columns with lower diffusivity facets, *i. e.* the adatoms are more likely to stick to these facets. In general, Zone T films are more dense, show a weak preference in texture that increases with thickness, and have a wide distribution of grain sizes due to the competition effects. The Zone T morphology is more clearly defined in sputtered films than evaporated films. This effect is due to the greater

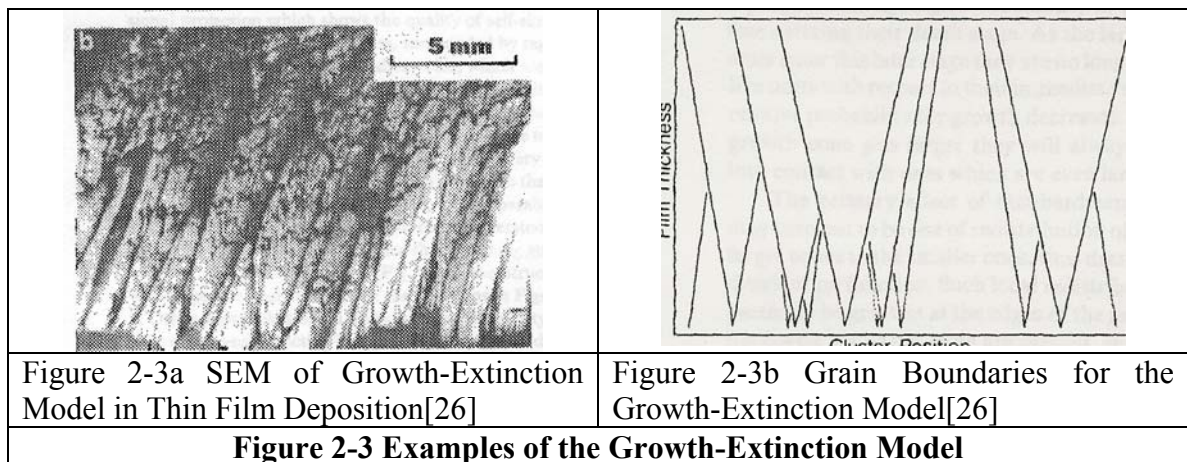
kinetic energy (thus higher mobility) possessed by the sputtered ions[22, 25], and the effects of ion bombardment on the surface.[23, 26]

In Zone II ($0.35 < T_s/T_m < 0.5$), bulk diffusion becomes significant and grain boundary migration can occur during the entire growth process instead of only during the nucleation and coalescing stage. The columns extend through the entire thickness of the films, are larger in width, and are more uniform in size, crystal texture, and shape. The grain sizes are significantly larger than in the preceding zones. In effect, the larger columns (those that “won” the growth-extinction competition) absorb the smaller, extinct columns through grain boundary migration. The primary texture is determined by the competition in the initial growth stages, and can be related to growth conditions or the substrate surface.[23, 27]

Finally, in the highest mobility region, Zone III, the grains have sufficient bulk diffusion and grain boundary migration for additional recrystallization to take place independent of the film growth. The grains are very large, globular (equiaxial) in shape, and randomly textured with respect to the substrate. In effect, the films are being deposited and annealed simultaneously, which allows each grain to recrystallize without the constraints of the substrate texture.

From the previous discussions, it should be obvious that the lower mobility zones provide the best opportunity to produce structured features. Therefore, a closer investigation of the Zone I and Zone T morphology is warranted. Since the development of TEM and AFM techniques, it has been seen that films deposited under low mobility conditions have similar honeycomb void networks which implies that a common mechanism exists for the origin of

this anisotropic morphology.[26] The surfaces have been referred to as “cauliflower-like” due to the similarity in appearance with the surface of the plant. The cauliflower plant growth is formed by a competition between randomly branching structures, which compete for light with the other structures. As one structure begins to shadow its neighbor, the shadowed neighbor receives less light and its growth diminishes. Messier and Yehoda modeled this type of growth for thin films using four key assumptions.[26] First, the structural features evolve continuously in this growth-extinction competition. The shadowed feature’s growth diminishes to the point the feature no longer receives any flux, or becomes extinct (stops growing). Second, at any given film thickness the largest features remaining have a greater probability to continue growth, i.e. dominate the competition. In addition, as features become larger, they eventually “sprout”, and produce continually evolving smaller structures. This concept can be easily visualized in the “cauliflower” structure. Finally, modeling of an atomistic self-shadowing mechanism showed that structural anisotropies naturally occur with dimensions on the order of 10-30Å. Figure 2-3 shows how the growth-extinction model approximates the columnar-void structures found in low mobility films.



The final deposition parameter to cover in this basic review is the angle of incidence of the vapor flux on the surface. The previous discussion assumes a relatively collimated vapor flux approaching the substrate at a perpendicular angle. However, the flux leaves the source with a wide angular distribution. Therefore, with a very wide substrate positioned close to a point source, the angle of incidence for the flux can vary greatly across the surface. Young, an early researcher in oblique angle PVD, recognized these films had different optical properties based on the position across the substrate and theorized the variation in flux angle introduced in-plane anisotropies to the films thereby changing the refringent properties.[28] Similarly, anisotropies were discovered in magnetic films with oblique angles of incidence. From an equipment development standpoint, this discovery may have contributed to the invention of planetary substrate holders. However, it was not until the development of advanced microscopy techniques that the physical results of these obliquely angled fluxes became quantifiable. When the vapor particle impinges on the surface from an oblique angle, it has a momentum in-plane with the surface. The momentum influences the direction the adatom moves along the surface. This “directed mobility” vastly enhances the effect of shadowing in that direction. In the lower mobility structural zones, this increased shadowing will cause a shift in column growth towards the flux source. In addition, the growth-extinction competition will favor column textures with preferred growth in the flux direction. In effect, the adatoms will prefer the lowest energy sites along the direction of its momentum, rather than the lowest energy sites in the area equidistant to the initial contact. The columns appear to tilt in the direction of the vapor source. Figure 2-4 illustrates how increasing the angle of incidence of the incoming flux also increases the tilt angle of the

columns. This directional column growth accounts for the anisotropies exhibited by films that are reflected in the film properties.

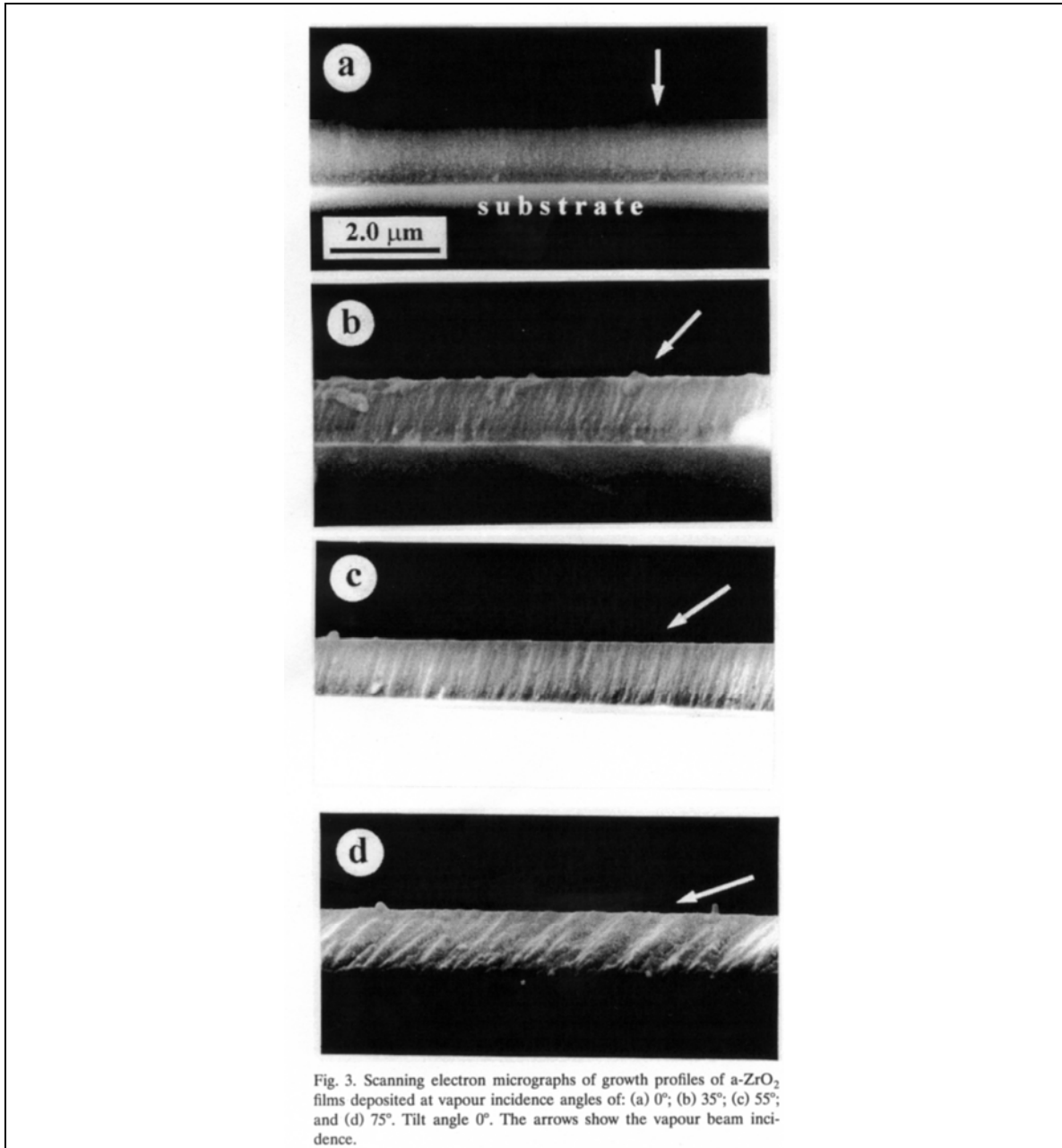


Figure 2-4 Effect of increasing the flux incidence angle on the tilt angle[29]

This basic review of the PVD growth process has developed several key points. Voids are formed during PVD film growth due to shadowing effects. To effectively control the formation of anisotropic features (i.e. control the voids) and create sculptured films, the shadowing effects must be the dominant factor in the morphology formation. The use of lower melting point deposition materials, T_m , or higher substrate temperatures, T_s , during deposition leads to increased surface and bulk diffusion. The structural zone models illustrate how the increased diffusion produces films with larger grain sizes, smoother surfaces, higher densities, and thicker columns. These factors are detrimental to the control of small features, which makes the formation of sculptured films more difficult. In the lower mobility zones where shadowing effects determine the morphology, the deposition can be modeled as a growth-death competition between the columnar features. By placing the substrate at an oblique angle to incoming vapor flux, it is possible to enhance the shadowing effects in one direction. This enhancement provides the mechanism to manipulate the growth of the columns in a controllable manner.

2.2 Evolution of Oblique Angle Deposition Techniques

Increased shadowing due to more oblique flux angles leads directly to more void formation and tilting in the direction of the flux source. The void formation and structural tilt combine to introduce anisotropies in the crystal structure and affect the physical properties of the films. The development of nano-scale sculptured films was a direct outgrowth of attempts to characterize and manipulate these anisotropies for desired film qualities. As previously

discussed, the first reports of unique optical properties in obliquely deposited PVD films appeared in the 1950s. However, over the next three decades, most of the published research in this area concerned the characterization of the magnetic anisotropic properties of these films. This focus most likely occurred from the combination of two factors. In the early years before advances in optics and electronic microscopy, the measurement, characterization, and applications for the magnetic properties were far more easily achieved. In addition, the economic opportunities associated with magnetic media for data, film, and voice recording provided a solid funding source for the research. Therefore, during this period the focus of the research was on the end properties of the films rather than the created nano-scale structures. In addition, much of the work concentrated on using deposition angles less than 60°. In this regime, the resulting column tilt angle, β , can be related to the deposition angle, α , by the tangent rule[30] :

$$2 \tan \beta = \tan \alpha \quad [\text{Eq. 2-1}]$$

It is only in the more oblique incidence regime, where the tangent rule does not adequately describe the results, that control of the shadowing becomes effective enough to allow for sculptured thin film growth.

Van Kranenburg provides an excellent review of oblique-incidence PVD through the late 1980s, especially in regards to the magnetic film research.[22] However, around 1990 several breakthroughs refocused the attention on the microstructure itself. The following

section describes how new deposition techniques, a focus on the highly-oblique regime, and the discovery of potential applications for these sculptured films led to the development of several new nano-scale structures. These new structures include multi-layer chevrons, self-supported cylindrical columns, chiral columns, and solid films deposited atop (*i.e.* capping) these other structures.

The first seminal event was a paper that was published in 1988 on the birefringent properties of tilting columnar films co-authored by Motohira and Taga.[31] There were two key elements in the work which moved the field of STFs forward. First, they successfully used the unique optical properties (birefringence) for a specific application, creating retardation plates for optical filtering and phase-contrast microscopy. Secondly, in order to improve the performance of these retardation plates, they added a second layer of deposition with the source aligned in the opposite direction from the first layer.

Young had originally reported on the birefringent properties of obliquely deposited flourite films in the late 1950s.[28] Several other groups reported similar results with other materials over the years. Nieuwanhizen produced an extensive review of these publications in 1966, but the focus was still on the material properties rather than the structure.[30] For example, typical titles of these papers include “Optical Properties of Obliquely Evaporated Aluminum Films”[32] and “Obliquely Deposited Amorphous Germanium Films”.[33] However, in the 1980s the effects associated with the structure of the oblique films came under more intense scrutiny. It became apparent that many of the unique optical properties were related more closely to the microstructure than the specific materials.

The subsequent investigation of Motohiro and Taga on retardation plates was based on this supposition.[31] They attempted to create retardation plates made by depositing films at highly oblique angles on glass substrates. They compared many deposition conditions (angles and pressures) and source materials (primarily metallic oxides). Significant differences were found between the materials deposition characteristics. The differences contributed to variations in the birefringence, Δn , and in the film's haze value (non-ideal transparency due to forward scattering). However, the successful creation of retardation plates using WO_3 , Ta_2O_5 , and Bi_2O_3 produced similar results and showed that the microstructure properties were the dominant factor in the film's optical response resulting in a successful application using this technique.

Even though a single layer of slanted film was able to produce enough birefringence to produce the retardation plate, a significant problem was found. The monolayer films had large anisotropies in birefringence based on the angle of the light source with respect to the column tilt direction. Therefore, the other major contribution of this investigation was the decision to add a second layer of oblique deposition, but with an opposite flux direction. This method produced a "zig-zag" or chevron formation. It was found to vastly increase the homogeneity of the optical response across the retardation plates. The resulting optical effect has come to be known as the "Taga Interface" [34]. Figure 2-5 shows an SEM image of this original Taga interface.

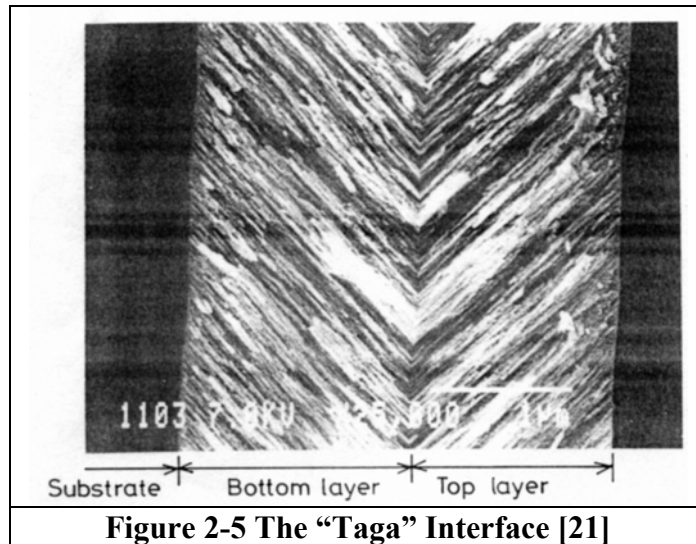


Figure 2-5 The “Taga” Interface [21]

The successful work of Motohiro and Taga refocused the attention on obliquely deposited thin films for optical applications. In addition, the renewed interest encouraged the search for other possible applications. A key factor to recognize in these films is that void formation in otherwise solid films decreases the density and increases the effective surface area of the material. This factor led to the beginning of the work by Robbie and Brett on highly obliquely deposited films, which was the second major event in the development of sculptured thin films.

The first experiments by Robbie and Brett were done in an attempt to produce thin films with greater porosity for use in gas sensors.[35] It was important not only as the first Robbie publication, but because it focused solely on using highly oblique ($\alpha > 70^\circ$) deposition angles for all cases. As mentioned in the nomenclature section, they also coined the term GLancing Ange Deposition or GLAD for this process. In addition, they investigated two new methods

for depositing material from multiple angles *in-situ*. A modification of one of these methods was subsequently used for much more advanced microstructures. But initially, the goal was to increase the film porosity in a controlled fashion.

The initial method was simply to use two separate evaporation boats (sources) and mount the substrate between them. For creating porous films, this method worked well in terms of the final structures. As the initial columns form, the shadowing from both directions combine to create narrow, bladed columns (similar in appearance to blades of grass) that are aligned with the sources. The columns are very non-uniform with jagged sides and have a random distribution of the primary tilt angle and position. Cross-sectional and planar view SEM images are shown in Figure 2-6.

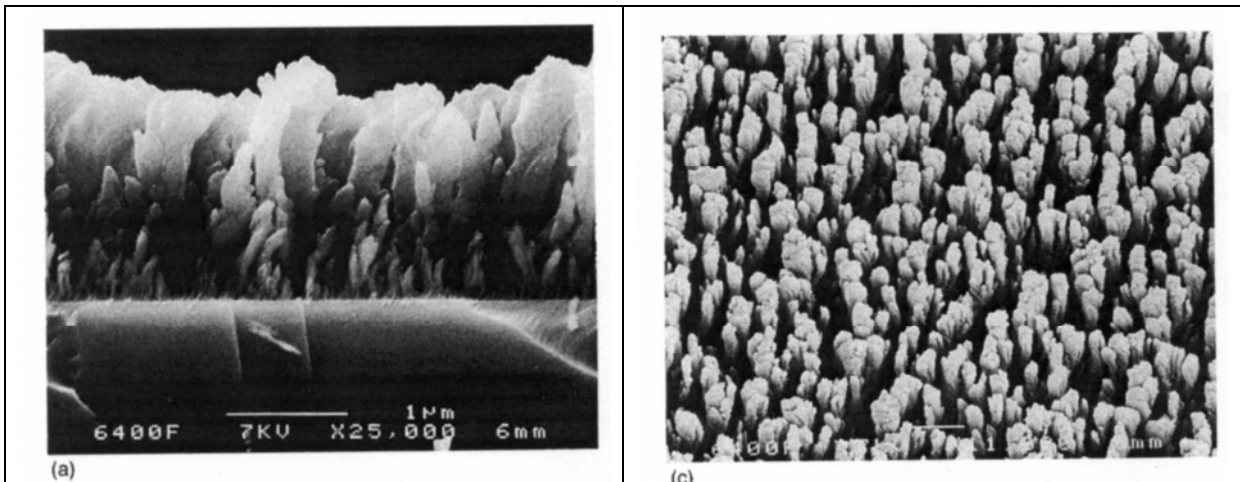


Figure 2-6a SEM of “blade” structures deposited using dual evaporations[35]

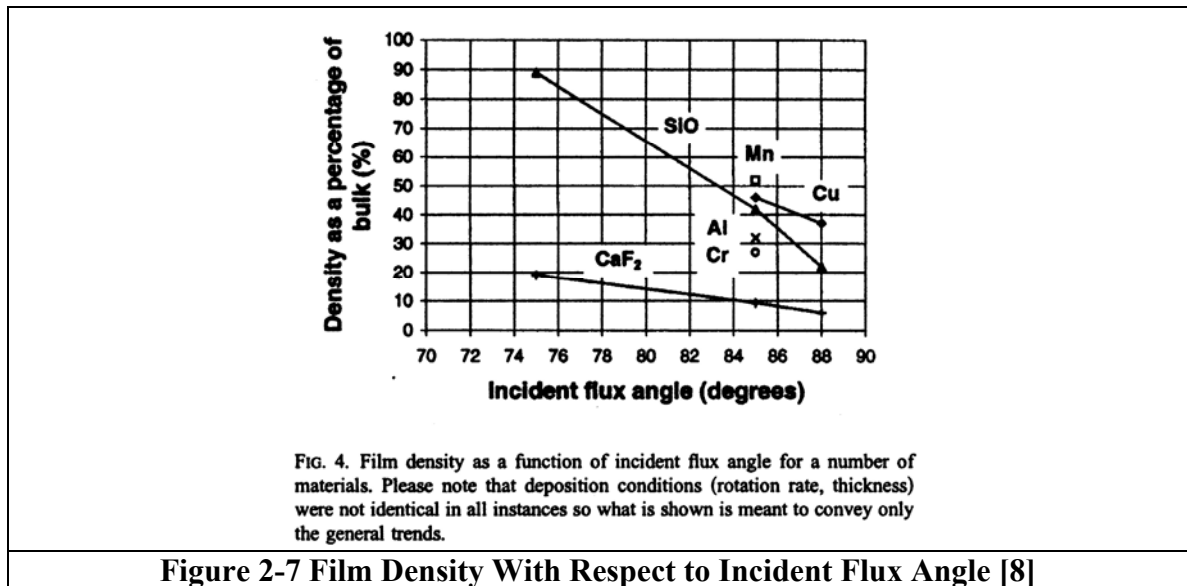
Figure 2-6b Planar SEM of “blade” structures[35]

Figure 2-6 SEM Images of “Blade” Structures

One cause of the non-uniform structures is the inherent difficulty in controlling the deposition rate for each of the two e-beam evaporations simultaneously. However, other practical issues were involved. Due to constraints in the size of the vacuum chamber, the two sources could only be mounted a distance of approximately 20 cm apart. In this case, the substrate needed to be mounted physically close to the two boats in order to have the flux angles from both sources in the glancing angle range ($>70^\circ$). The close proximity of the substrate to the sources creates two major issues. As previously mentioned, at these close distances the flux angle varies greatly (*i.e.*, the flux is not collimated) across the target area. Since the shadowing and deposition rates are highly dependent on the flux angle, this variation causes significant non-uniformity in the growth and porosity across the surface. Also, the e-beam melt generates a large amount of heat, so radiative heating off the substrate becomes very significant with close proximity to the source. This increases the T_S/T_M ratio described in the structural zone model, which reduces the shadowing effects and thus the structural formation.

Since the process issues make the two-boat system impractical, another method for depositing from multiple directions needed to be developed. The next solution was to mount the substrate at the end of a short pendulum that had nearly 180° of arc movement. At one extreme, the substrate surface has an incident angle of 85° with respect to the source. Using a stepper motor, it could swing down to a position normal to the source then up the other side to 85° from the opposite side. Shielding prevents deposition from occurring during the transfers from one side to the other. By mounting the pendulum much farther away from the source, the substrate heating was reduced and the flux collimation increased. The results

were similar to the Taga method, but the flux direction change was conducted in-situ and was capable of more oblique deposition angles. The more oblique angle increases the shadowing and hence the individual separation of the columns. Figure 2-7 shows the changes in thin film density (porosity) achievable using the oblique pendulum method. Densities close to 15% of bulk were achievable using high melting point materials such as MgF_2 . The porosity decreases for lower melting point (higher adatom mobility) materials. This result is expected due to decreased shadowing effects.



The third major event advancing STF development was the formation of helicoidal or chiral formations by Robbie, *et. al.* in 1995.[36] It was the result of a confluence of several different groups' directions, focus, and experiences. Chiral materials have polarizing optical properties which have been widely exploited using twisted-nematic liquid crystal layers under a glass cover plate for display technology. Lakhtakia began speculating on and

modeling the effects that could be achieved by more stable solid chiral media. The ideas were extended by Azzam for several applications, but most relevant to this discussion would be a polarization plate that retarded orthogonal circular states in a manner similar to the Taga interface linear retardation plates described earlier.[37] However, Azzam went further and described a potential method for creating solid chiral media using a PVD platform. He proposed rotating the substrate slowly during a GLAD process. The axis of deposition (and hence shadowing) is continuously changing during the process. Under very low adatom mobility conditions and slow rotation, the growth occurs in a chiral shape. For example, with the chevron pattern created with the pendulum mount, each step was the result of a new deposition axis, albeit displaced by 180° . With a slow rotation, a series of new steps are continuously forming with a small angular displacement for each step. In effect, the steps form a spiral staircase, or alternatively, the shape of a spring.

The structures envisioned in Azzam's proposal were not realized for several years. It was during collaboration with Lakhtakia at a conference that Robbie realized the pendulum mount could be modified to test Azzam's hypothesis.[38] By replacing the pendulum rod with a rotational mount controlled by another stepper motor, both the rotational speed and incident flux angle can be changed in-situ. This control allowed the creation of the first chiral sculptured thin film or thin film helicoidal bianisotropic medium.[36] Figure 2-8 demonstrates the results using a high melting point material, MgF_2 . Once again, the adatom mobility plays a key role in the degree of shadowing and thus the sharpness of the structures created. It was at this point that the interest in and advances thereof sculptured thin films modeling and deposition became prevalent.

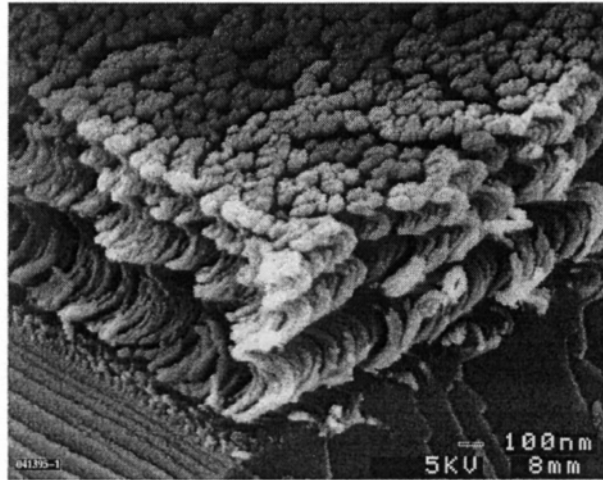


FIG. 3. SEM micrograph of a cleaved corner of a four-turn MgF_2 HBM thin film exhibiting helical columnar microstructure.

Figure 2-8 First Thin Film Realization of a Helical Bianisotropic Medium[36]

Once chiral structures were produced, the logical step was the creation of cylindrical columns or pillars. The pitch is defined as the height of material deposited during one rotation. An increase in rotation speed reduces the pitch, in effect compressing the spring shape. As the speed is increased, the chiral striations smooth out, and a solid pillar is formed. The pillar structure is more robust in terms of stability and processing. Therefore, this structure forms one of the cornerstone formations in this research on increasing the porosity for thin film gas sensors. Figure 2-9 shows TiO_2 pillars deposited using the BMMSL evaporation system. There are several key factors to note at this point. The pillars grow noticeably wider with height. Many of the columns seem to have stopped growing at various heights. These stunted columns are more frequent at lower heights culminating in a chaotic “scrub-growth” near the surface in the first 100 nm. These affects and the growth dynamics that affect the width, shape, density, spacing, tilt angle, etc will be discussed in more detail in a later section.

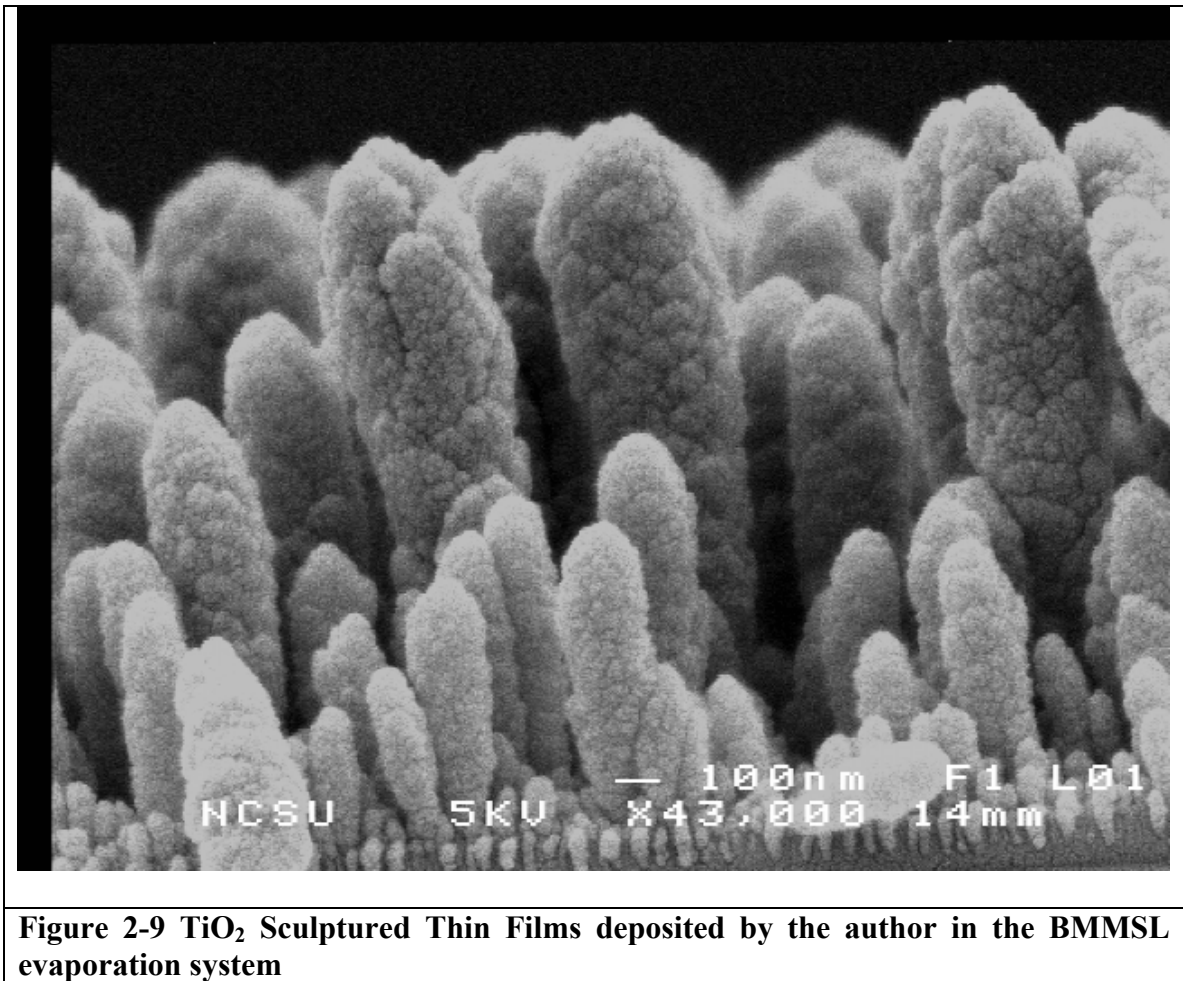
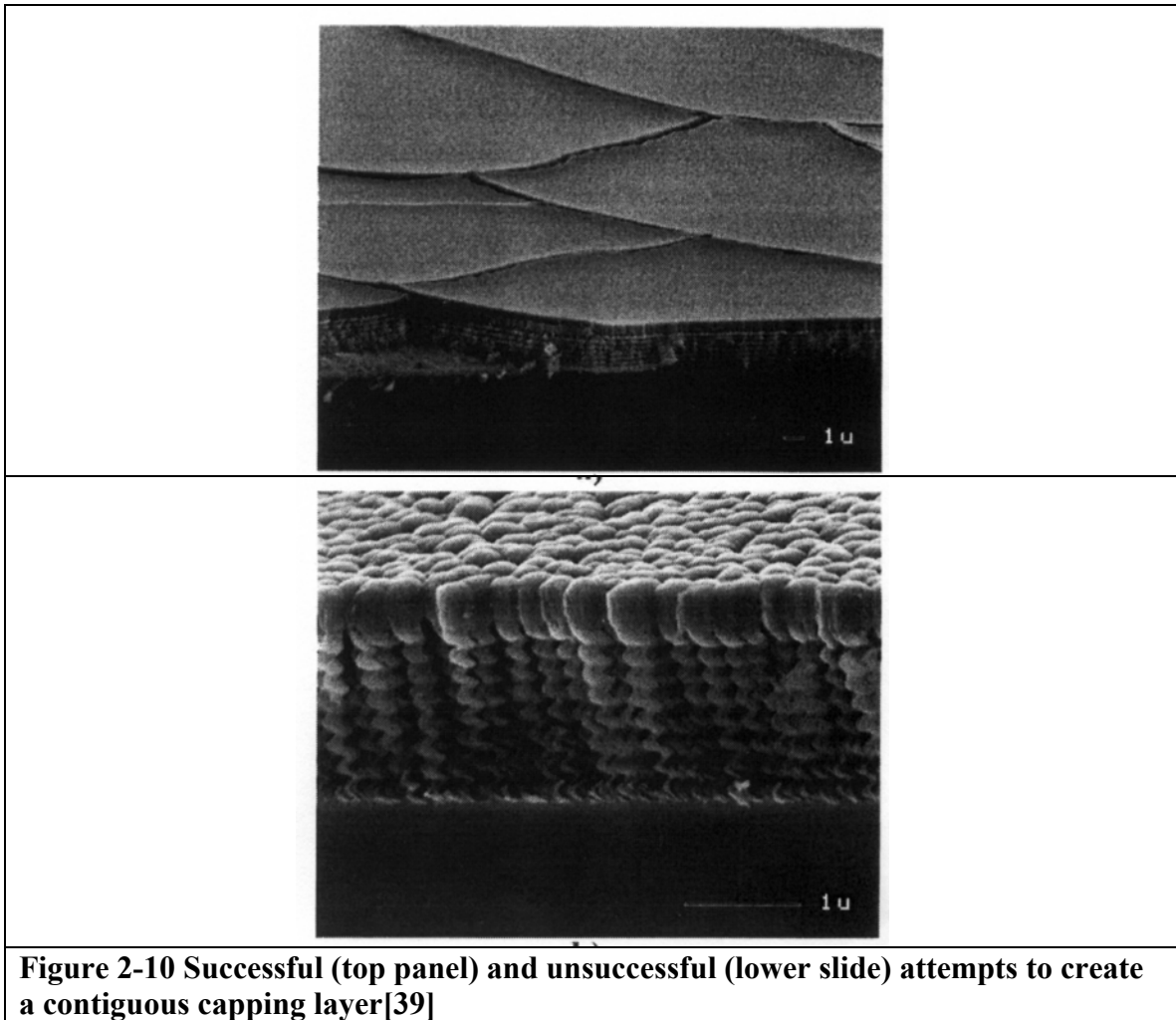


Figure 2-9 TiO₂ Sculptured Thin Films deposited by the author in the BMMSL evaporation system

The second cornerstone formation for sensor development is a solid layer atop (or capping) an array of pillars. If the pillar width can be rapidly increased when a desired height is achieved, it should be possible to fill in the voids between the tops of the pillars. The effect occurs in a manner similar to the channel filling described in the previous section. In theory, the manipulation of several of the growth dynamics that cause pillar widening should eventually produce the desired solid layer. However, in practice, the only successful method to date requires a simultaneous change in the incident angle, α , towards the normal, while

increasing the rotation speed.[20, 39] The optimal combination was to change the incident angle linearly, while increasing the rotation exponentially. Figure 2-10 shows both successful and unsuccessful implementations of a contiguous capping layer using this method.



The three main events: 1) the “Taga” interface formation, 2) Robbie’s first work on porosity engineering using *in-situ* control of the flux incidence angle, and 3) Robbie’s experimental realization of the chiral films described by Azzam constitute the first phase of STF

development. The optical interface development by Taga clearly demonstrated the use of higher melting point materials and more oblique deposition angles provide enough control to create definable nanostructures. Successful use as wave retardation plates generated renewed interest in optical applications for these films. In addition, by using several layers of deposition, new and unique structures could be created using different deposition conditions. But it was Robbie's focus on improving the substrate mounting to implement multiple deposition styles *in-situ* that provided the key to truly controlling the nanostructure. Finally, the imagination and collaboration between Laktakia, Azzam, and Robbie provided the direction to open up the next phase of STF development, the investigation of the STF growth dynamics.

2.3 Growth Dynamics of Sculptured Thin Films

Beginning around 1996, the second phase of STF development concentrated on understanding the growth dynamics during the depositions and how these dynamics affect the shape of the structures. Multiple growth studies were conducted either from direct experimentation[8, 16, 39-41], using simulations[42-45], or using a combination of the two approaches[19, 46, 47]. For the most part, this research has concentrated on the most fundamental STFs – the slanted films (or chevrons with multiple layers), and the basic vertical column or pillar. The pillar formation is intrinsic to the gas sensor design. Therefore, this section focuses on the fundamentals of the pillar growth dynamics. The presentation will concentrate on the experimental side, with simulation results added when relevant.

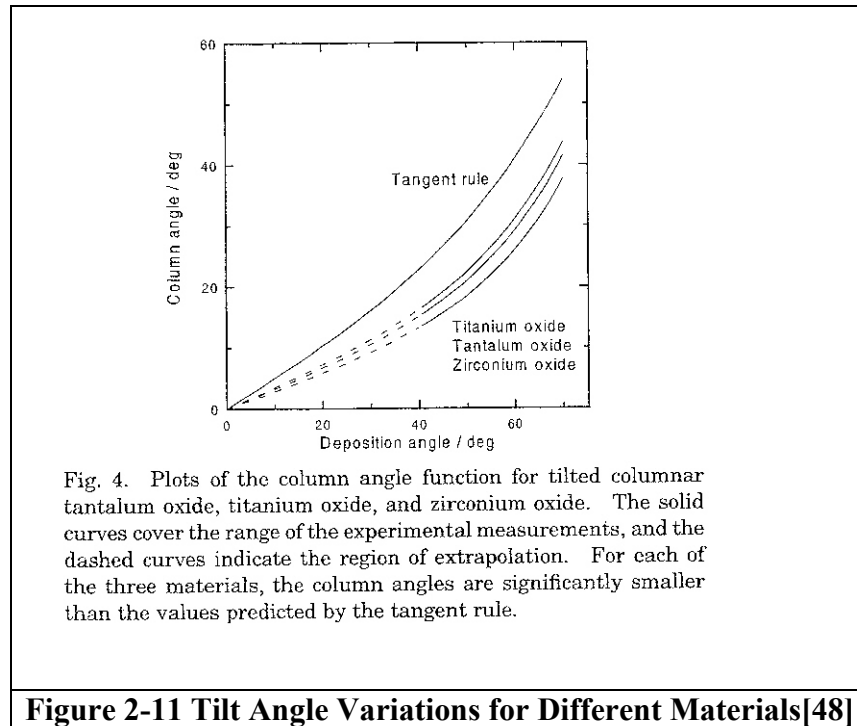
This section covers many of the finer points on STF growth dynamics. Initially it is useful to review the research on slanted columns and chevrons which provide insight into initial nucleation, filament microstructure, the effects of stacked structures (initial seed formation), and on the effects of process conditions during deposition. Key aspects for pillar formation include the role of pitch in determining the structure, the effect of collimation, pillar thickening, and most importantly, the relationship between the film density, column thickness, and column spacing.

Although the broad range of STFs share many of the same growth dynamics, there are some areas unique to the slanted columns (single-layer) or chevrons (multi-layer) structures. The most widely researched of these factors is the column tilt angle, β . Due primarily to in-plane adatom momentum and surface diffusion, β is in general significantly less acute than the deposition flux angle, α . Several approaches to quantify this relationship have been published.[18, 30, 42, 45]

The “tangent rule” provides a good basis to begin discussions on the tilt-angle/flux-angle relationship. Based on empirical data from numerous sources and developed by Niewenhizen in 1967, the tangent rule is as follows:[18, 30, 42, 45]

$$2\tan \beta = \tan \alpha \qquad \qquad \qquad [\text{Eq. 2-2}]$$

The rule does a very good job in describing the basic relationship between the tilt angle and an increasing flux angle, but does not have any provision for a large increase in the surface flux momentum or for changes in the material properties. This effect can be seen in the Figure 2-11, which shows the predicted tilt angles from the tangent rule along with empirical data for several materials.[48] The shapes of the curves are similar,



but the β values are different for each material. The differing material properties affect the surface diffusion for each system and contribute to these variations. In addition, for flux angles greater than 60° , the large surface momentum begins to dominate the nucleation pattern and the “tangent rules” have been shown to be no longer valid.[18, 45, 48] The “Tait rule” improves on the tangent rules for slightly more oblique flux angles ($60^\circ < \alpha < 70^\circ$): [45]

$$\beta = \alpha - \sin^{-1} [(1 - \cos \alpha)/2] \quad [\text{Eq. 2-3}]$$

The “Tait rule” is based on a 2-D ballistic deposition simulation using adatoms modeled as discs and incorporates some surface diffusion and column spacing, but does not consider diffusion between columns. This method and several similar versions are known as the “cosine” rules. Lintymeyer provides an excellent review of these methods.[18]

The methods for predicting the tilt angle (or more accurately, the limitations of these methods) illustrate quite effectively the need to quantify the effect of the surface diffusion to adequately model the STF growth dynamics. Paritosh has shown in extensive simulation work that modeling the shadowing effect alone cannot accurately predict many of the film properties observed empirically.[49] These properties include the columnar tilt angle, void fraction (porosity), mean column diameter, and grain size. Their simulation data became less accurate as the deposition angle increased, which suggests the surface diffusion, species size, sticking coefficients, and other surface factors play an increasingly significant role during the more extreme angle depositions. Other simulation methods have shown similar results. The SIMBAD simulator developed by Smy improved on the Tait (cosine rule) efforts by including movement along the surface to the initial algorithm.[42, 43] As subsequent efforts have added more weight to the diffusion factors, including 3-D movement, the results have become even more successful. In addition, several experimental methods developed to control the tilt angle also illustrate the importance of these factors. The next few paragraphs discuss these methods and segue into the more critical deposition dynamics of pillars. The tilt

angle was chosen to be investigated in depth here as it is a singular, yet critical measurable in the deposition of the chevron STFs. Therefore, it served as a simpler initial presentation of the complex issues in STF formation than the fuller, interrelated dynamics of pillar formation.

Process conditions can also have a significant effect on the tilt angle. Lintymeyer found that for flux angles greater than 30° , the pressure in the deposition chamber has a quantifiable effect.[18] Figure 2-12 provides an excellent illustration not only of the pressure effect, but also of the predicted β values from the two major “rules”: the tangent rule and the cosine rule. As the pressure increases, the tilt angle becomes less acute (i.e. the columns are closer to vertical). Increased pressure results in more collisions occurring in the gas phase between the evaporated flux and the molecules in the chamber atmosphere. Therefore, the collimation of the flux is decreased. From the earlier discussion, we know the decrease in collimation decreases the shadowing effect. But more interestingly, the average momentum (and thus the average directed momentum) of the impinging flux is also decreased.

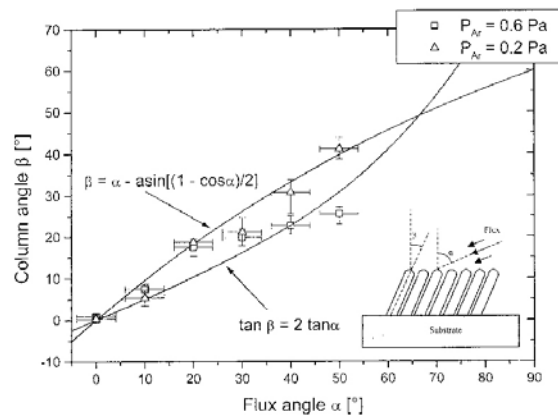


Fig. 2. Column angle β for two different working pressures as a function of the flux angle α . Comparison with the theoretical rules 'tangent' and 'cosine'.

Figure 2-12 Effect Of Pressure On The Tilt Angle[18]

The opposite effect on the tilt angle (a rotation of β towards α) has been observed when ion bombardment is used during the deposition.[50] The amount of this rotation increased when the energy of the ions was increased. Since the x component of the ion stream is nominally in the same direction as the x component of the flux, the net effect would be an increase in the directed momentum of the flux along the x (surface) plane. The results for the ion bombardment and the increased deposition pressure both imply that β is a strong function of the directed momentum or what is effectively the surface diffusion length.

Multi-layer films add more complexity to the tilt angle dynamics. In order to properly utilize multi-layer chevron films for optical purposes, the tilt angle of all of the layers must be controlled. However, given the difficulty shown in predicting the exact column angle that results when the initial surface is polished, it is not surprising the column tilt angle/flux angle

relationship changes for each subsequent layer when the initial surface is a set of columns slanted away from the flux direction. In fact, the change in β is not insignificant. Harris found the tilt angle variation can average 8% from layer to layer for a fixed flux angle.[16] The primary tilt angle for each layer was measured by analyzing SEM images using sophisticated imaging algorithms. They reported some success modeling the change by substituting a new flux angle calculated with respect to the previous layer's tilt angle, but found the second layer tilt angle was consistently underestimated. The faceting (or rounding) of the columns near the tip is a likely source for this error. In addition, large variations associated with the materials systems (i.e. diffusion lengths) were again evident.

It is clear from the simulation results and the various experimental attempts to manipulate the column tilt angle the surface diffusion length is a very critical factor in determining and controlling the STF growth dynamics. This tilt angle discussion has provided an excellent metric to illustrate this factor. These next methods for controlling the tilt angle now serves as a bridge into the dynamics and interactions involved in pillar formation, and lead to more advanced surface structures.

The slanted films discussion also provides an excellent example of the cross-coupling of various STF growth parameters. In effect, the relationships between the deposition angle, α ; the column tilt angle, β ; and the film porosity. Although surface diffusion and other factors play a critical role in the exact form of these relationships, the empirical rules demonstrate a direct connection between α and β , *i.e.* as α increases, so does the corresponding β . A direct relationship also exists between α and the film porosity. As α increases, so does the effective

shadowing and consequently larger voids are formed in the films. This also leads to an increase in the overall porosity of the deposited films. Therefore, by supposition, the column tilt angle and the film porosity must also be similarly coupled.

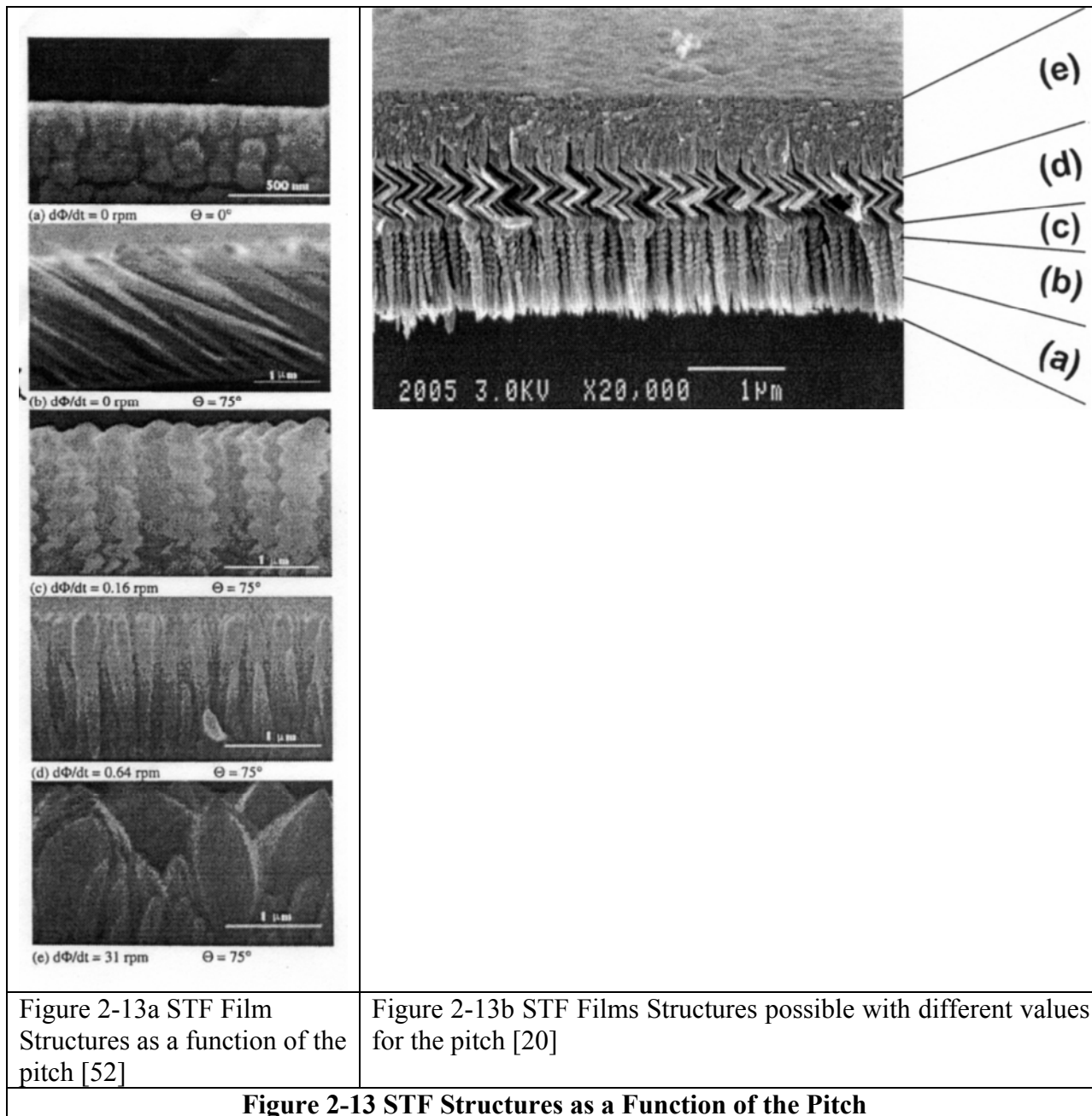
Film porosity and the column tilt angle are not the only critical parameters that are interrelated. As the discussion moves toward pillar formation, the porosity becomes an important factor in both the column width and the column spacing for GLAD film growth. GLAD structures can be grown on seeded or unseeded substrates. With seeded substrates, features are added to the surface to act as nucleation sites (or seeds). These seeds could be lithographic patterns, defects in previously deposited films, or large (nm) scale debris. The patterns are usually periodic in nature to control the GLAD structures growth in a systematic way by controlling the growth competition. This style of film formation has been referred to as “periodic” GLAD structures, while films grown on flat surfaces are referred to as “aperiodic films” to distinguish them. With aperiodic growth, the nucleation sites and initial growth competition occur stochastically and the formations are randomly distributed. Initially, all discussion will assume aperiodic growth conditions. The growth dynamics associated with periodically seeded substrates will be addressed later in the chapter.

For pillar formation, the pitch (deposition per revolution, p), is a critical component alongside of the flux angle. As the pitch is increased during the GLAD process, the aspect ratio of any vertical formation also increases.[20, 41, 51] At a median pitch, the formation appears as a solid pillar. Increasing the pitch leads to formation of the helical structures. The phenomenon can be illustrated by imagining a spiral staircase or a spring. If the height of

each step (pitch) in the staircase is increased, the spiral elongates. As substrate rotation approaches the limit of static (no rotation), the spring is stretched to the point where over the short range it appears as an oblique slanted column in the direction of the flux. At the other limit, when the substrate rotation is too fast, this spiral is quashed flat and loses its shape. At this point, the shadowing becomes disordered and the films display a “leaf-like” columnar growth.[41] There are several factors which influence the transitions between these growth models. They include the angle of flux incidence, the substrate temperature (or more importantly T_s/T_m from the Structural Zone Model discussion), the deposition material, and the substrate. While several groups, including work in this dissertation, have found similar results qualitatively[20, 41, 51], the quantitative pitch values at which the transitions between these growth models occur vary greatly. Table 2-2 shows the reported pitch values for the various formations. Figures 2-13a and Figure 2-13b show SEM images of the various formations.

Table 2-2 The STF Formation With Respect To The Pitch

Reference	Material	Flux Angle	Pitch nm/rev	Formation
Liu[41]	Fe	75°	750	Helices
Liu[41]	Fe	75°	188	Pillars
Liu[41]	Fe	75°	3.8	Leaf
Suzuki[20]	TiO ₂	82°	16	Pillar
Suzuki[20]	TiO ₂	82°	79	Helices
Dick[51]	SiO ₂	85°	42.8	Pillar
Dick[51]	SiO ₂	85°	125	Helices



The formation of helices in particular demonstrates some of the critical requirements necessary to fabricate the sculptured thin films. It is much more difficult to produce the fine

features in the helices than the more solid pillar formations. Once again the mobility of the deposition material plays a critical role.[8] Low mobility materials (SiO_2 , Si, etc) are able to produce the whole range of finer structures. But lower melting point materials like bismuth show a very strong dependency on pitch and substrate rotation. This dependency is even more pronounced for films that have a tendency toward faceted growth such as aluminum.[51] The GLAD process, especially during initial nucleation, exaggerates any growth advantage, *e.g.* along favored crystal planes. This factor leads to strong texturing in the crystal structure of these films, an aspect that will be discussed in a later chapter. Finally, a very narrow flux distribution is critical for helices formation. Wider flux distributions cause a degradation of helix growth into pillar formations.[53, 54] Helices formation is one area where evaporation has a distinct advantage over sputtering due to the much narrower flux distribution with evaporation. The effect is demonstrated by a comparison of pillar formations using both methods on a periodically seeded substrate. The sputtered pillars (b, the four lower slides) in Figure 2-14 have significantly greater asymmetry in size and shape.[53]

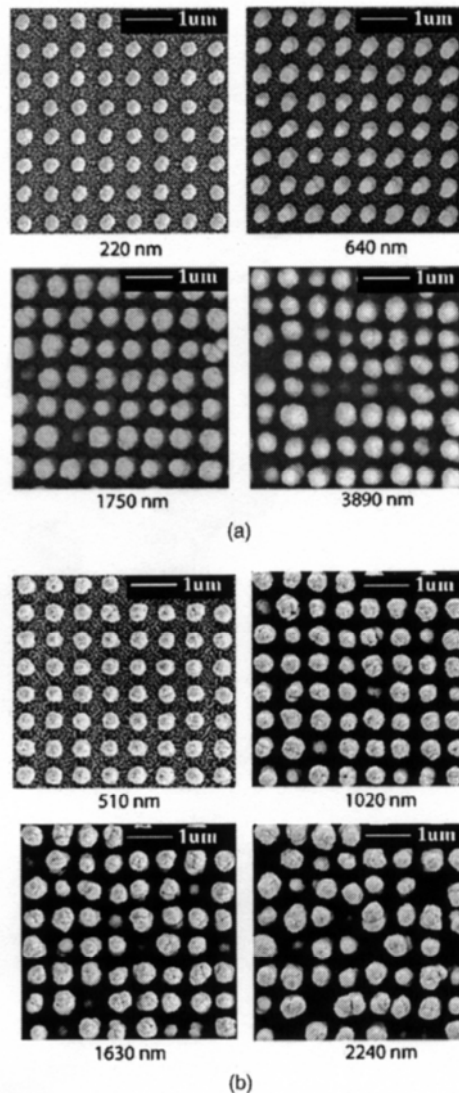


FIG. 5. Comparison between periodic GLAD films grown by evaporation and sputtering. Each film was grown on a seed array with $p=600$ nm and is shown at four points in its growth evolution (film thicknesses are shown below each image panel). (a) shows an evaporated SiO_2 film grown at $\alpha=85^\circ$ ($\Delta\alpha=2^\circ$). (b) shows a sputtered W film grown at $\alpha=86^\circ$ ($\Delta\alpha=6^\circ$).

Figure 2-14 Evaporated (top) and Sputtered (bottom) GLAD Films[53]

The initial nucleation and growth for aperiodic pillars helps define the final appearance of the films. As can be seen for previous figures such as Figure 2-9, the initial 100 nm of growth has a large number of very small structures. These structures appear to be randomly

distributed around the base of the larger pillars. In this region, the growth-death competition described in Section 2.1 leads to a very high extinction rate for the individual islands of growth. Any island which randomly attracts a greater amount of flux than its nearest neighbors begins to shadow these same neighbors. The shadowing process follows a self-amplifying path in which additional shadowing increases the growth rate of the shadowing feature even more. However for approximately the initial 100 nm, the films do not have time to form recognizable structures and resemble “curly hair”.[55] Next to the “forest” of pillars however, it also resembles the scrub growth found on the floor of a tree forest. The GLAD growth competition is also analogous to forest growth as the larger trees receive more sunlight, which leads to increase in the taller tree’s growth. The size and shape of the scrub layer also has a strong material and surface diffusion dependency.

As the growth continues out of the “scrub layer”, pillar structures continue to emerge. The columns quickly form to a minimal thickness which is determined primarily by the surface diffusion length.[42] The extremely high columnar extinction rate evident earlier in the deposition begins to slow. While there are still several medium height pillars, the larger trees (columns) begin to form a stable pattern. The mean separation distance between the surviving columns increases as other columns are shadowed and their growth is extinguished. Also, the columns broaden as each column grows taller. Working together from both the experimental[46, 47, 56] and the modeling[42] paths, Vick and Smy determined that the higher rate of extinction tapers off until a quasi-stable ratio is achieved between the mean column separation, a , and mean column diameter, d . A graphic experimental example of this competition can be seen from Figure 2-15 where the deposition was stopped for aerial SEM

pictures at several different times (i.e. thicknesses). The thicker films show fewer pillars, the pillars are significantly wider, and the rate at which the pillar growth is extinguished drops off quickly. For a constant rotational speed, the density of the films depends almost solely on the flux angle. [56] Since the density depends almost solely on the flux angle α , it is a stable parameter over most of the film deposition when α is fixed. The a/d ratio must therefore be quasi-stable as it directly relates to the density of the films. At any given height value, the areal density can be determined by knowing the number of pillars and the mean pillar thickness.

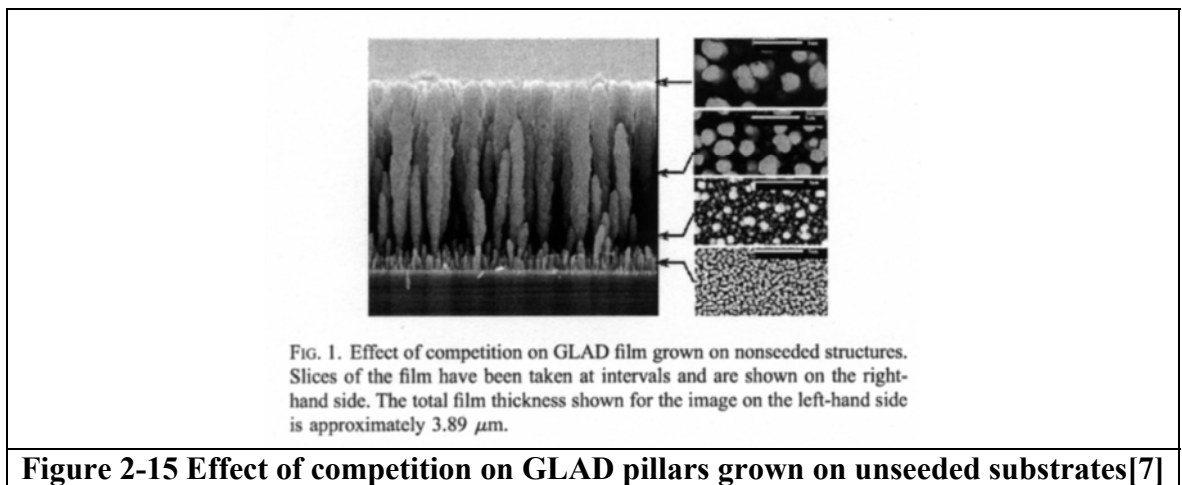
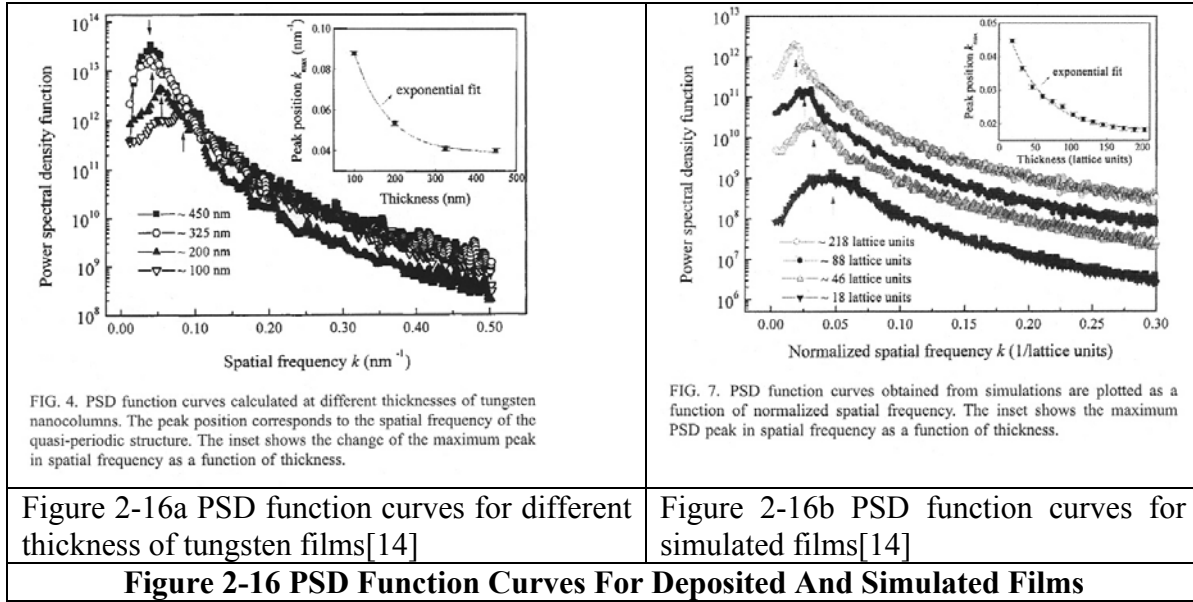


Figure 2-15 Effect of competition on GLAD pillars grown on unseeded substrates[7]

The visual imagery in Figure 2-15 provides a qualitative example of the competition effect, but from the planar SEM images it is difficult to accurately determine the mean column separation for a given column height. A direct quantitative measurement of the mean separation value, a , versus the column height (film thickness) would be beneficial. Fortunately, Atomic Force Microscopy (AFM) can measure the height variations across the

film surface with great precision. Karabacak noticed the AFM images of sculptured pillar films demonstrate a quasi-periodic nature with respect to their height.[14] The power spectral density (PSD) is a signal processing technique based on the Fourier transform that allows one to identify periodicity in data sets (in this case, the AFM surface height measurements). Peak values in a PSD frequency profile occur at frequencies where significant periodicity exists. Non-periodic functions have a flat PSD profile. For the PSD of the surface heights, the variable of interest is the spatial frequency, k (nm^{-1}). The spatial frequency, k , or more accurately, the corresponding spatial wavelength is related to the mean separation distance between the features (or column tops) which exhibit the periodicity. Figure 2-16 shows the PSD output for two sets of deposited tungsten pillars (a) and similar sets of simulated pillars (b) using a 3-D Monte Carlo simulation package.[14] The different curves in each graph correspond to films of different thicknesses. The insets provide the location of the peak position, k_{max} , as a function of the film thickness. The peaks become more intense and sharpen as the films grow thicker, indicating the surface heights have a more periodic distribution. In addition, the locations of the peaks shift toward a smaller spatial frequency as the thickness increases. In physical terms, these results indicate the mean column separation distance increases with thickness and the surface can be defined by a greater percentage of columns which are very similar in height. In other words, there are fewer (albeit wider) columns spaced farther apart. Also, from the inset, the rate at which the separation is changing exhibits an exponential decay, which suggests that a saturation value or steady-state conditions is being approached. These results quantitatively support the columnar growth-extinction model that has been described for oblique columns.



Although the extinction rate appears to taper off until nearly steady-state film growth occurs, the column broadening continues at a higher rate than the 2-D growth simulations predict.[42, 45] Therefore, the extinction process actually continues for much longer than originally expected. The continued column widening appears to indicate that a mechanism exists to construct a solid capping layer above a porous pillar region.

Malac in 2001 proposed several potential mechanisms that could be responsible for this continued broadening.[57] All of these mechanisms may have some effect on the column broadening.

1. Increase in surface diffusion length due to substrate heating
2. As helices terminate, mass balance requires more to be deposited on the others

3. Decreased sticking coefficient due to more scattering between the columns
4. Bifurcation (branching) in the pillars
5. Preferential crystal plane growth
6. Recrystallization leading to larger grains in the radial direction

These mechanisms form the basis for the long quest in our lab to gain sufficient pillar widening to close the gaps without changing the flux angle *in-situ*. However, over the years since Malac proposed these solutions, increasingly sophisticated modeling techniques have determined that the instability in aperiodic growth is directly related to the stochastic nature of the entire GLAD deposition process.[17, 42, 49, 58] In other words, the extinction process continues because even with a quasi-stable process, some pillars are still growing randomly which changes the shadowing dynamics. Any anomaly present early in the nucleation process continues to affect the stability throughout the entire deposition. One example of the inherent instability is demonstrated by the variation of the sticking coefficient with incident angle. Since even the highly collimated e-beam system has some flux angle variation, different incident angles create a variation in sticking probability across the sample, which leads to a constant variation in film thickness and porosity. This variation provides a source for a perturbation of the growth on a random column, thus changing the shadowing profile and leading to a column extinction. But on balance, there is a relationship that does exist between the flux angle α , the film density, the mean column spacing, and mean column thickness. This relationship is dominated by one important factor. YES, it is the surface diffusion length.

Karabacak also identified a scaling behavior related to the column broadening that allowed was able to provide a solid metric to investigate the effects of including surface diffusion in both a Monte Carlo model[59] and later a continuum model.[58] The broadening, defined as the column width as a function of height (or deposition time) appears to follow a power law formulation:

$$W \sim Z^P \quad [\text{Eq. 2-4}]$$

where W is the column width, Z is the column height, and P is the power law scaling factor. Figure 2-17 shows this scaling behavior for deposited films of (a) Si, (b) Co, (c) Cu, and (d) W. The scaling factor, P , ranged roughly from 0.28~0.34 for the films shown.[17] Later Monte Carlo simulation work predicted the scaling factor would range from 0.5 with no surface diffusion to a value of 0.31 with significant surface diffusion. The empirical values of 0.28-0.34 compare favorably to the simulations with the surface diffusion included. Additional material variations may be due to factors such as preferred texture growth, changes in the sticking coefficient, or other surface material properties that are not in the Karabacak Monte Carlo model.

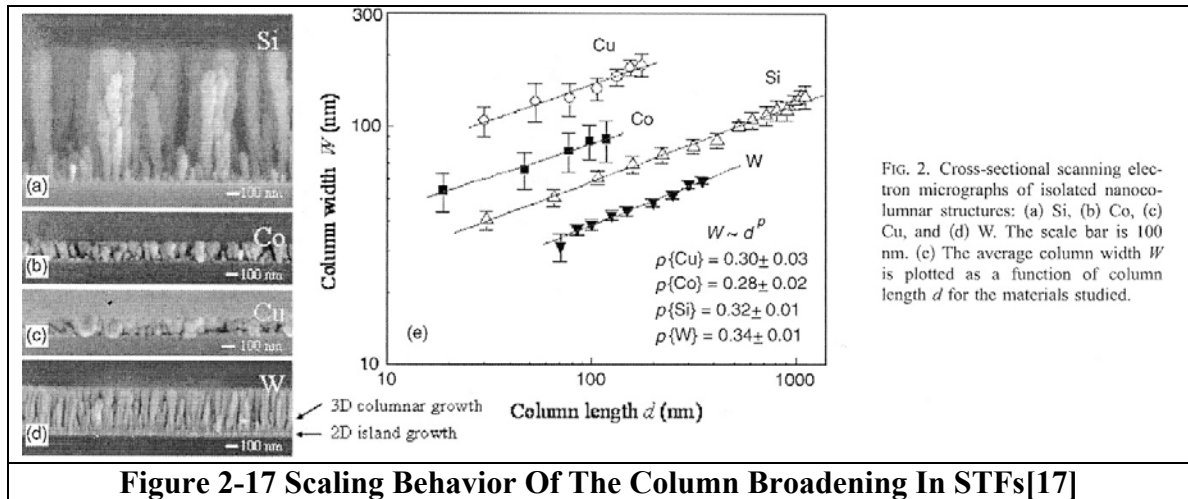
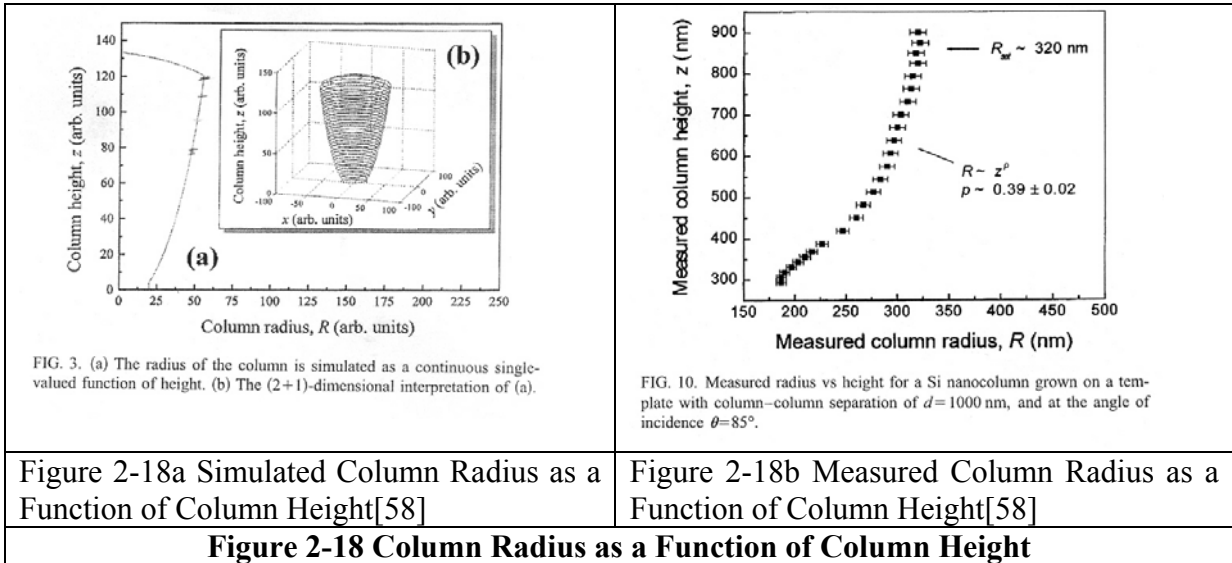


Figure 2-17 Scaling Behavior Of The Column Broadening In STFs[17]

Working with Karabacak, Main developed a continuum model for the column broadening that directly outputs the column radius as a function of the height.[58] Using a symmetric seed column for the starting conditions, the continuum model found a scaling factor of 0.37 which is close to the Monte Carlo and empirical values. The continuum model predicts a saturation value for the broadening, but the saturation value is dependent not only on the standard parameters such as flux angle, but also on a noise term, and on internal coding variables (i.e. the number of points used to numerically calculate the height). Also, the continuum model does not consider the effect of a change in the shadowed flux due to any change in the mean column spacing. However, qualitatively the saturation of the column broadening is consistent with both the apparent saturation of the mean column spacing and the stable relationship expected between the column spacing and column width. Finally, Figure 2-18a shows the predicted values for a simulated column, while Figure 2-18b shows the measured values for a silicon nano-column deposition.[58] In order to be consistent with the model, the deposition was on a template with a column separation of 1000 nm. Note the

empirical column width measurements approach saturation when the column radius approaches 320 nm at a height of 900 nm. Over the last 200 nm of height, the width increases only 10 nm. Even assuming the rate of change is constant after this point (in opposition to the predicted saturation), it would require an additional 3600 nm of deposition to close the gap between these columns and provide a solid surface.



The discussion to this point has focused on aperiodic growth, i.e. growth of structures on substrates that are initially flat and have no pre-existing features which contribute to the shadowing. In other words, all of the effects are the result of “self-shadowing”, in which only the previously deposited material serves as the shadowing source. However, if a nucleation island can begin to significantly shadow the area around itself, it stands to reason that a pre-existing feature of similar size will have the same effect. With aperiodic growth, the porosity of the film can be controlled, but the localized features are randomly distributed across the

deposition area. For many applications involving the STF structures, it is desirable to control the spacing of the features. Therefore, a significant thrust in recent years has been using initial seed layers for control the STF formations. Many different methods have been employed to create this initial seed layer including e-beam lithography[7, 53, 60], embossing techniques[61], direct laser write lithography[62], and using a monolayer of nanoscale colloids (90nm polystyrene balls) on the surface[63-65]. Since most of these techniques are used to produce periodic patterns, these depositions on seeded substrates have been referred to as “periodic” STF structures. This section describes the evolution of these techniques, while showing how the results of these seeded depositions helped further the understanding of the STF growth dynamics for unseeded films.

During the initial nucleation phase for aperiodic STF depositions, there exists a period where multiple islands form and are quickly shadowed by neighboring islands. This region was earlier referred to as the “scrub-growth” layer. The growth in this region is characterized by a very high rate of feature extinction until a preferred density is established, and the surviving pillars begin to emerge. As this growth-extinction competition is stochastic in nature, so is the axial distribution of the surviving features. This initial stochastic competition must be suppressed to produce periodic films. Therefore, the initial seed layer should contain features similar in size, shape, and spacing to the randomly growing pillars that emerge from this scrub layer.[60]

In characterizing the growth of STF's, Karabacak introduced the concept of the shadowing length.[14] As illustrated in Figure 2-19, the shadowing length defines the distance over

which a particular feature produces a shadowed effect. The shadow length concept directly relates to the mean separation distance between the columns. Since the mean column separation distance for random films has a strong material dependence, and is quite likely a function of the surface diffusion, Karabacak argues the shadow length can be analogously used with the surface diffusion length to qualitatively discuss some of the growth dynamics in STF's.[14, 17] This concept will become apparent as this discussion investigates the effects of varying the initial seed period.

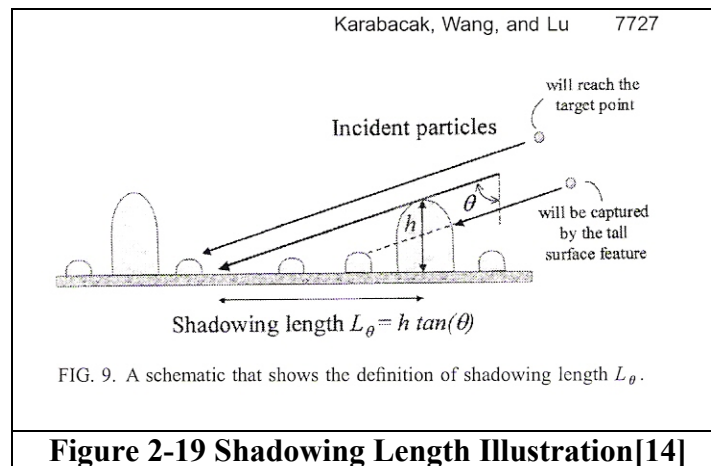


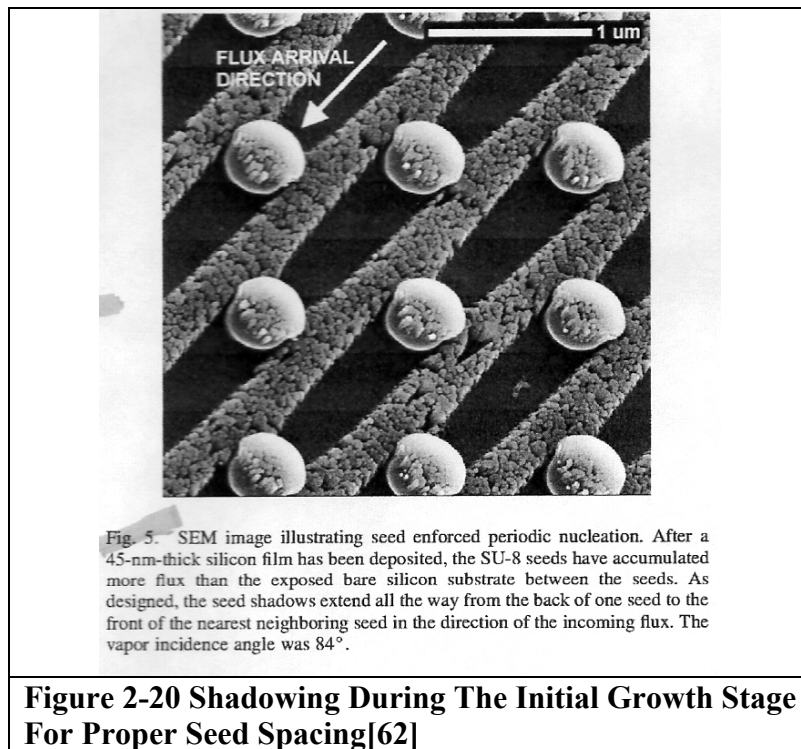
Figure 2-19 Shadowing Length Illustration[14]

Similarly, Dick suggests an optimal seed separation, δ_{opt} exists for a given set of material and depositions conditions which results in STF growth with the same periodicity as the initial seed layer.[53] In both examples, the groups assume the shadowing behavior is the dominant mechanism in the film formation and that all of the shadowing is provided by nearest neighbors. In this case, the forms of each equation are identical. Therefore, the optimal seed

separation is equivalent to the shadowing length for a given height and conditions and has the form:

$$S = \delta_{\text{opt}} = h \tan(\alpha) \quad [\text{Eq. 2-5}]$$

where S is the shadow length, δ_{opt} is the seed separation, h is the feature height (or film thickness), and α is the flux incidence angle. Figure 2-20 shows the shadowing during the initial growth stage for a properly designed seed separation. The shadow length in this micrograph just reaches the nearest neighbor and shadows the area in between. The deposition in this example is only from one direction rather than with substrate rotation to better illustrate the effect.



Assuming the optimal seed separation is equivalent to the shadow length, what would the result be if the initial seed separation, δ , is not at this equilibrium value? If $\delta > \delta_{\text{opt}}$, the shadow length does not reach to the nearest neighbor. Some portion of the flux reaches the unshadowed area of the substrate and localized areas of the scrub growth appear. The seeded pillars will also grow, but more slowly than if at equilibrium when the entire scrub region is shadowed. However, most of the material will impact on the seeds rather than be lost in the scrub area. As the height of the pillars increases, the shadow length, and thus δ_{opt} do also. Eventually, the areas between the pillars are covered by the shadow area and equilibrium is approached. If $\delta < \delta_{\text{opt}}$, then there are more pillars than needed. The mean separation distance is too small and some part of each pillar is shadowed. Significant competition effects occur between the seeded pillars and some of the pillars become shadowed completely (or extinguished). As each column is extinguished, the mean column separation (i.e. the effective δ) increases and approaches the δ_{opt} value. The competition effect between the pillars is the key aspect of the sculptured pillar depositions. The introduction of the seeds delays the onset of competition between the desired pillars (i.e. on the seeds), while enhancing the extinction of the undesired pillars (in the scrub area). The seed pillar competition is delayed until the shadow length (or in effect the pillar heights) catches up to the seed separation.

One of the underlying concepts in this discussion is the tenet that for a given material system and deposition conditions, the density of the pillar STF's is coupled directly to the flux

incidence angle. As the flux angle becomes more oblique, the shadowing length increases, and a smaller area of the surface is exposed to the flux. Therefore, the density of the STF also increases. The second part of the tenet is that the ratio of the mean column spacing and the mean column diameter adjust to this density rather than determining the density. It is relatively simple to introduce periodic seeded elements into the initial conditions of ballistic simulations. Figure 2-21 shows the results for simulations that illustrate the relative independence of the normalized film density with respect to the initial seed separation distance, (graph (a) in the figure). Similarly, from graph (b) in the same figure, the change in flux angle from 82.5° to 86.0° decreases the normalized density by approximately 30%. In order for the density to be independent of the seed separation, the corresponding pillar diameter must quickly increase along with the mean separation distance to keep the ratio invariant. Figure 2-22 shows the pillar widening with respect to separation distance for films with various initial seed separations. The figure is presented as a pseudo-SEM micrograph to be visually comparable to Figure 2-15 shown earlier for real deposited films on non-seeded substrates. Note how the pillar diameters grow larger for the areas with fewer pillars (and hence a wider separation distance). Also, for the smallest seed period, the initial competition effects between the seeded pillars are evident.

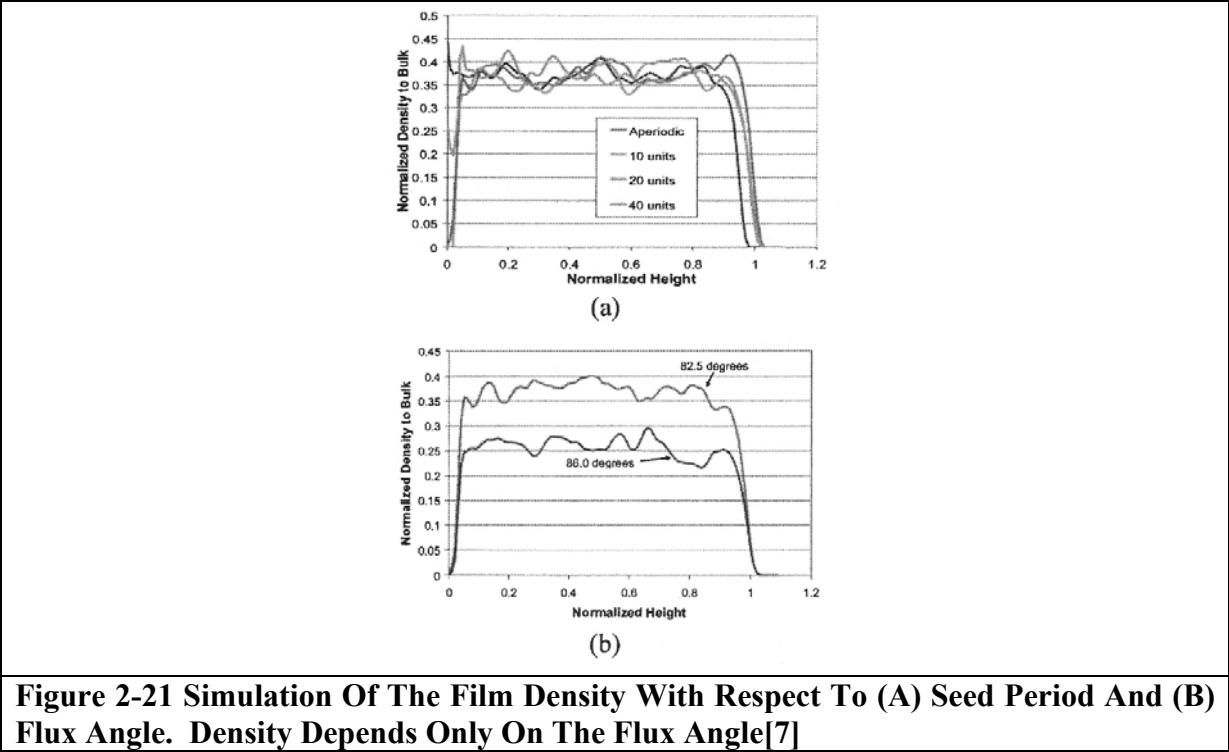


Figure 2-21 Simulation Of The Film Density With Respect To (A) Seed Period And (B) Flux Angle. Density Depends Only On The Flux Angle[7]

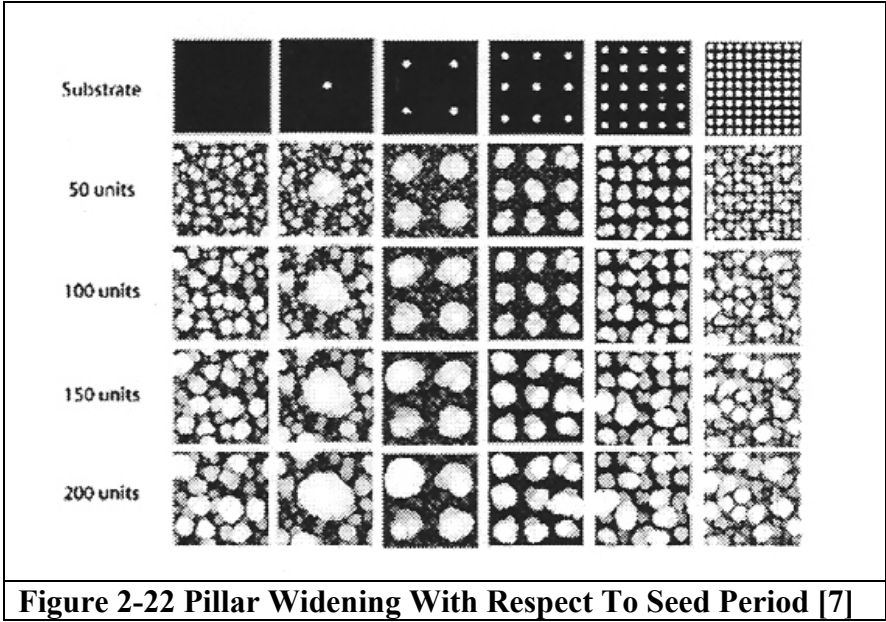


Figure 2-22 Pillar Widening With Respect To Seed Period [7]

2.4 Advanced Sculptured Thin Film Techniques

This section deals with some advanced techniques for depositing sculptured thin films. While they are not presently possible using BMMSL technology, they do provide significant insight into the theory and experimental results behind oblique film deposition. The first area covers the deposition of a capping layer on top of a porous film structure by changing the flux angle *in-situ*. [20, 39, 66-68] Another technique leads to direct manipulation of the tilt angle and control of the shape of the pillar. [63-65, 69] A similar technique, the Phi-Sweep method, works well for tailoring the shape of the pillars, essentially decoupling the porosity from the flux angle. This discovery led to the development of a new type of film exhibiting a very fine microstructure. [70-72]

2.4.1 Capping Layer

The key for producing a vertical capacitance sensor structure is the ability to deposit a dense (solid) film atop the porous microstructure created by pillars, helices, or chevrons. With this “capping layer”, it is then possible to deposit electrical contacts to the top side of these structures. The bottom contacts can either be on the substrate surface or a back-deposited metal layer. This choice is determined by the substrate conductivity and by the choice of electrical characterization for this sensor. Robbie published the first description of how to achieve this solid layer in 1997. [8] The method requires a “goniometer” style sample stage that is capable of changing α dynamically while still maintaining substrate rotation. As the flux angle moves toward the normal, the density of the films increases. This leads to a rapid

increase in column width and thus to a solid film as the columns merge. If α decreases too rapidly, the film undergoes an infill process where the voids between the pillars receive flux. This infill leads to non-uniform stresses in the films and fracture is a likely result. The best method for producing a quality capping layer is to decrease the flux angle exponentially with time, while linearly increasing the rotation rate. From the earlier discussion on pitch, simply increasing the rotation rate without changing α leads to a non-uniform “leaf-like” growth.

Several others have used the technique[20, 66-68], but to date no one has published a solid capping layer deposition method which does not utilize a dynamic change in the flux angle of incidence, α . Figure 2-23 shows an actual humidity sensor with a helical sensor area, a capping layer atop the helices, and gold contact layer deposited by normal incidence sputtering atop the capping layer. The Figure 2-24 shows a well defined capping layer, with approximately 300 nm between the tops of the helices and solid layer. In this case, there is roughly 500 nm between the tops of the helices and the gold layer. In general, it takes about 300 to 500 nm of growth for the solid layer to form even with the *in-situ* control of the flux angle.

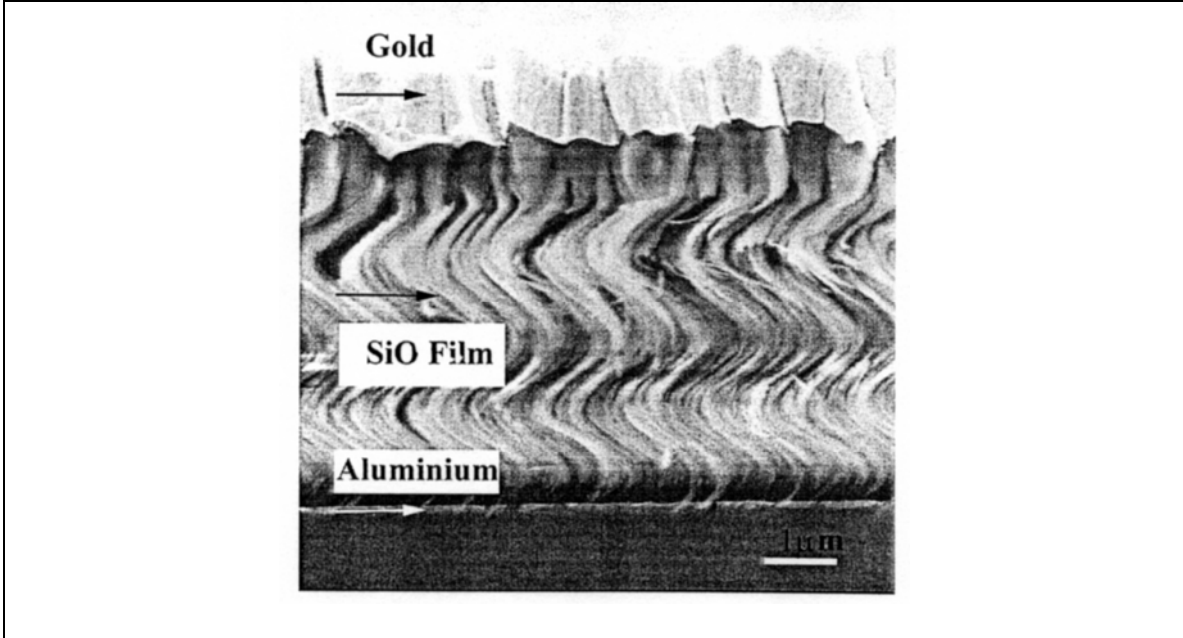


Figure 2-23 Humidity Sensor with Capping Layer[67]

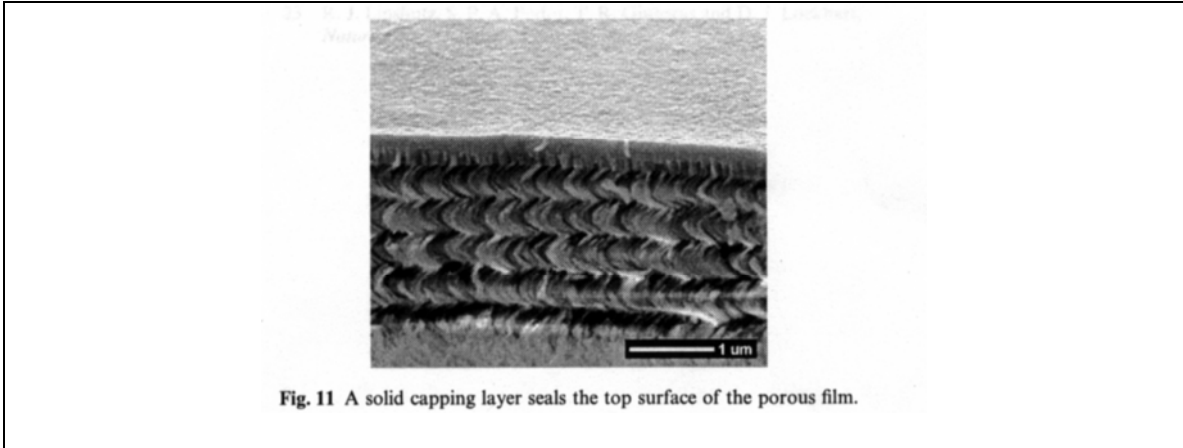


Fig. 11 A solid capping layer seals the top surface of the porous film.

Figure 2-24 Well Defined Capping Layer Atop Porous Films[66]

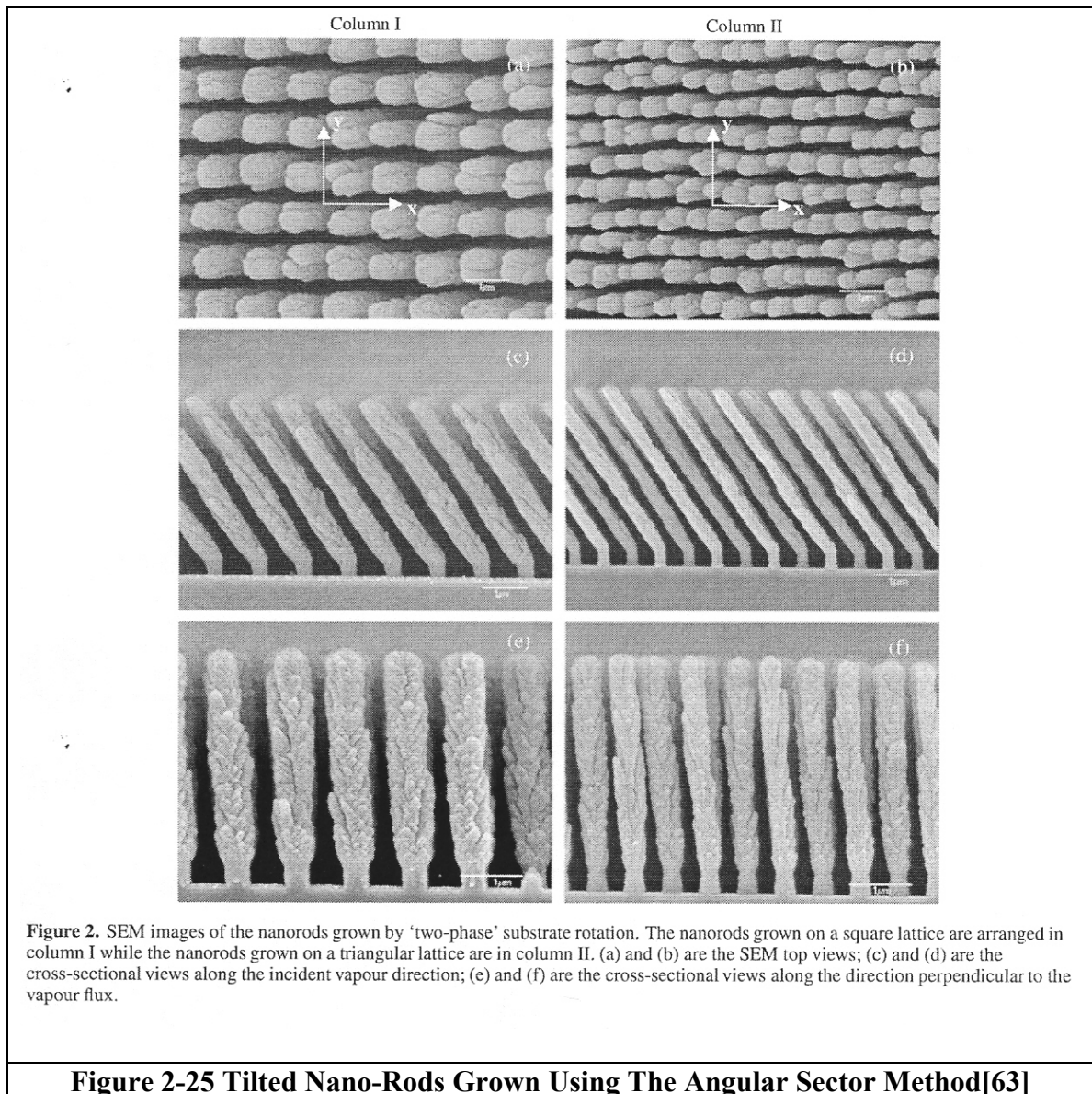
2.4.2 Tilt Angle Manipulation

As the knowledge of the growth dynamics of sculptured films has deepened, the research focus has shifted from basic understanding towards increasing the manipulation and control of the process. One area where this shift has occurred concerns manipulating the tilt angle, β , for slanted column deposition. For many optics applications, controlling the tilt angle and the column size are critical for creating a particular optical effect. As previously discussed, the tilt angle, β , is directly related to the flux incidence angle α . This relationship has been well characterized using the “tangent” and “cosine” rules. Some degree of control of β can therefore be obtained by adjusting α . However, the range of β control is not very large, and as α moves toward normal incidence, the shadowing effects are greatly diminished. Moreover, the density of the slanted film (i.e. the spacing and column width) is also affected by changes in α . A method to manipulate the β independently from α would allow a greater range of slanted films.

A series of methods have been investigated towards this end.[35, 63-65, 69] The initial attempt, the “zig-zag” technique, consists of depositing along a stationary axis for a set length of time, t_1 ; rotating the sample 180° with source shuttered; and then depositing for a different length of time, t_2 . [35] If $t_1 = t_2$, repeating this process produces the chevron films, but if $t_1 \gg t_2$ the effect is to bring β more toward the surface normal than if the deposition was only along the first axis. While this technique showed some promise, the primary drawback was the slanted columns flatten considerably along an axis perpendicular to the flux directions and resemble the “blades of grass” discussed in the earlier section.

The next step in the tilt angle manipulation was simply to rotate the sample, but not with the constant rotation rate, ω , used for pillar and helix formations.[69] Instead, the sample is rotated at different rates, i.e. ω_1 and ω_2 , over different arcs (Φ_1 and Φ_2) for each rotation. During the slower rotation more material is deposited on that region of the column. On unseeded substrates, the tilt angle can be changed 15°-30° by simply varying the size of the angular sectors, Φ_1 and Φ_2 , and the ω_1/ω_2 ratio.[69] Of course, if 2 angular sectors can be programmed into the stepper controller, then obviously 3, 4 or 5 angular sectors can also be used. Using a ω_1/ω_2 ratio of 30, Zhao produced films that had 2, 3, 4, and even 5-fold symmetry in the pillar distribution on unseeded substrates, and columns with like symmetry using a 90 nm colloid seed layer.[65] The five-fold columns resemble the bloom of a flower, and were dubbed “nano-flowers”.

Since the use of periodically seeded substrates can delay competition effects in pillar formation, it should have a similar effect on slanted films. This turns out to be the case; however the slanted features still exhibit the flattening effect seen previously. The angular sector method described above has the ability to control both the tilt angle and the shape of the column. Therefore, combining the proper seed layer with an optimal angular pattern should allow excellent control of slanted column depositions. Figure 2-25 shows what this combination is capable of producing. Note the columns are nearly round, have negligible widening, and demonstrate the precise control over the tilt angle that was the focus of this section.



2.4.3 Phi Sweep Method

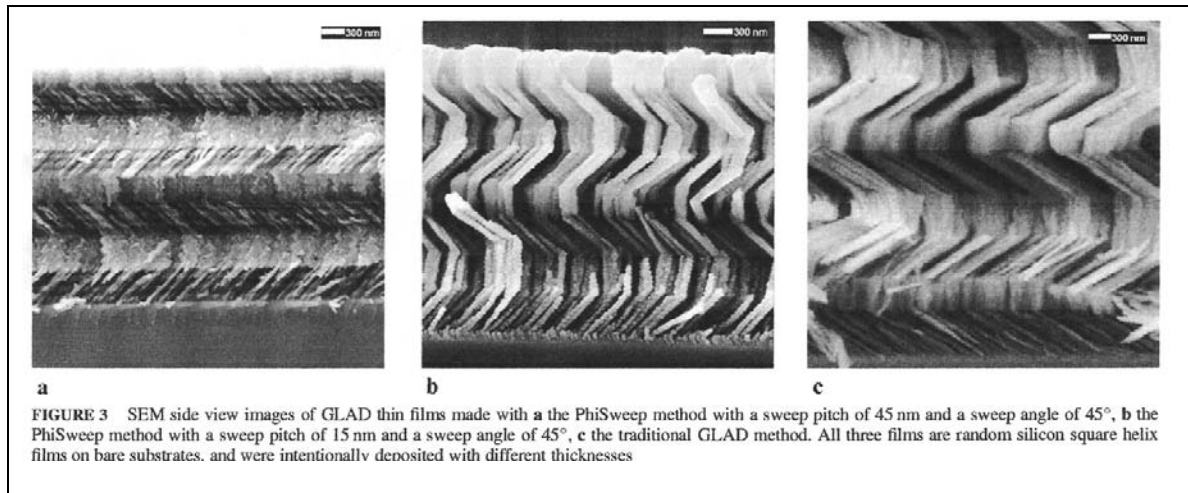
The final advanced STF technique presented in this section is the Phi Sweep method.[62, 70, 71] The method is similar to the angular sector method in that the core feature is control of

the rotational axis to continuously adjust the radial direction from which the flux arrives at the substrate. The origin of the Phi Sweep method is the “spin-pause” technique, in which the substrate is rotated to a specific angle and then paused for a set length of time.[35] In the Phi Sweep, the substrate is swept from side to side over a specific arc (typically 90°). At the end of each sweep, the substrate is paused for a set time or amount of deposition (aka the sweep pitch). The sweep angle is considered to be one-half of the total arc. The basic result is the growth of a feature slanted toward the centerline of the deposition arc, effectively decoupling the direction of the incoming flux from the primary direction of column growth.[62]

The original intent of the method was also similar to that of the angular sector method, i.e. to grow a slanted feature while having increased control of the shape and tilt angle of the feature. For small sweep pitch values (~15 nm), the results were as anticipated. The features resembled those created by the traditional STF techniques but with more control of the features. However, an unexpected effect was discovered when the sweep pitch was increased to 45 nm during a silicon deposition. The shapes of the STF structures were the same, but there were significantly more of them, and the typical column widths were very fine (20-30 nm). These nanofibrous features exhibit little or no column broadening from the substrate all the way to surface of the film.

During the discussion on initial nucleation, the “scrub-layer” was described where many small features formed until some of them reached a characteristic size or shape and began to shadow their neighbors. With the nanofibrous Phi Sweep structures, it appears the initial type

of growth conditions is constant, and the scrub layer growth model continues for the entire film thickness. For every sweep, the flux comes from a new direction and with enough material the shadowing competition is effectively restarted. The amount of sweep pitch which is necessary appears to be related to the critical size of the nanofibers in the formation. If the pitch is below this size, the amount of material is not enough to change the shadow effects completely and a traditional STF feature is formed. But if the pitch is larger than this critical size, the nanofiber features form. Figure 2-26 shows the side view (top panels) and planar views (bottom panels) for three types of square helices depositions. The left side panels are the nanofibrous films (45 nm pitch), the middle panels are the Phi Sweep STF's (15 nm pitch), and the right side panels are films deposited using traditional STF techniques. Note this technique produced the very dense packing of the nanofiber films. However, under similar deposition conditions, the final film thicknesses are similar for all three types of films, which imply the film densities are equivalent. It is obvious though, that the pore sizes of the nanofiber films are much smaller. The surface area of these films has been estimated conservatively (assuming the fibers are smooth, straight cylinders) at $68 \text{ m}^2/\text{g}$, more than ten times the measured values for traditional STF structures.[62]



766 Applied Physics A – Materials Science & Processing

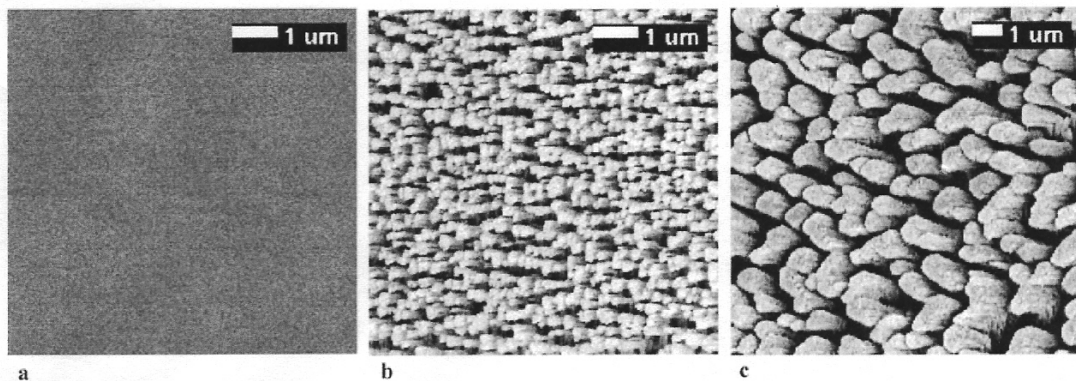


Figure 2-26 SEM images of Phi Sweep Films[62]

2.5 Conclusions

The structure of films grown by physical vapor deposition depends on the interplay between shadowing effects and diffusion. Depositing the films at highly oblique ($>80^\circ$) angle enhances the shadowing effects and permits the formation of sculptured thin films. Although the existence of a slanted pillar formation from this type of deposition was known in the 1950's, it was not until the early 1990's that other types of features were produced by

physical manipulation of the substrate during the deposition. Films with varying densities, sizes, and shapes can be created with nanometer scale dimensions. The process has many applications in the fields of sensors, optics, and nanomaterials.

Chapter 3

Morphological Control of TiO₂ Sculptured Thin Films

3.1 Introduction to Morphology

The sensing mechanism for most thin film metal oxide (MOS) gas sensors is based on the interaction of the surrounding atmosphere with the film surface. Therefore, increasing the available surface area should increase the sensitivity of the sensor. GLancing Ange Depositions (GLAD) use highly oblique flux angles to take advantage of atomic level self-shadowing and thus form nanometer scale structures or Sculptured Thin Films (STFs).[39, 51, 73] These STF structures can be vertical columns, helical columns, slanted pillars, or chevron formations. The effective surface area of a GLAD porous vertical column structure can easily be 40 times that of normal incidence (standard) deposited films.[44] However, GLAD films also can exhibit markedly different crystalline orientation [15, 74] than standard films, and respond differently to post deposition heat treatments.[75]

Titanium dioxide (TiO₂ or titania) has several polymorphs that exist at room temperature. The most common phases are rutile, anatase, and brookite. Of these, the anatase and rutile phases have been widely used for thin film gas sensors.[6] Anatase and rutile titania possess markedly different characteristics in electrical properties, photocatalytic interactions, and surface properties. Therefore, it is desirable to control the anatase/rutile (A/R) ratio in thin films used for gas sensors. In addition, the anatase to rutile transformation depends on many factors including initial deposition process and conditions, annealing conditions, grain size, and film impurities (dopants).[76-87]

This research examines the various titania phases produced by GLAD techniques and the effect of post deposition heat treatments on the final properties of the thin films. Experiments were designed to identify the critical parameters in the formation of the various titania phases during e-beam evaporation of sculptured thin films. The results of the materials characterization of these films are presented in relation to the available literature.

3.2 The Titania System

Anatase and rutile are the most common products of inorganic synthesis and form the vast majority of commercially available nanosized titania powders or thin films. Titania thin films or nanosized titania powders are generally created using either sol-gel methods [76, 83, 88], or with physical vapor deposition techniques [73, 80, 85-87] such as the reactive e-beam evaporation method used in this work. It is very difficult to synthesize films with a majority concentration of brookite, and only recently (2005) has pure brookite become commercially available.[89] Due to the difficulty in isolating brookite, it has not been reported extensively in thin film sensors and will not be a major focus of this review. On a macroscopic (bulk) level, rutile is the thermodynamically stable polymorph. Rutile is approximately 1.2-2.8 kcal/mole more stable than anatase.[90] Both brookite and anatase are metastable at room temperature. In other words, the rate of the transformation of anatase or brookite is too slow to be measurable. However, sufficient heating will eventually turn all titania into the rutile phase. For a metastable to stable transformation there is no absolute transformation temperature. Instead, the transformation occurs within a temperature range

and is influenced by many factors. However, once the stable polymorph (rutile) has formed, the transformation is irreversible by thermal processing.

Table 3-1 - Physical Properties of Anatase and Rutile[81, 90-93]

	Density g/cm ³	Refractive Index	Dielectric Constant	Band Gap (eV)
Anatase	3.84	2.55	~31	3.2
Rutile	4.26	2.73	60-100	3.05

	Bulk Modulus (Gpa)	ΔH° (kcal mol ⁻¹)	ΔG° (kcal mol ⁻¹)	S° (cal/deg mol)
Anatase	179	224.6	211.4	11.93
Rutile	211	225.8	212.6	12.03

The polymorphs have remarkably different physical properties. Table 3-1 shows a compilation of some key parameters reported in the literature.[81, 90-93] The density of the amorphous (α -TiO₂) phase has been reported as between 3.2-3.65 g/cm³. [81] The density increases from this value through the anatase phase until reaching a maximum in the rutile phase. This densification is consistent with reports that the thickness of thin titania films decreases by 6-8% with high temperature annealing.[83, 86] In addition, the refractive index and the dielectric constant increase as the material transforms and densifies.

Rutile and anatase both have a tetrahedral crystal structure. Anatase and rutile consist of chains of octahedral rings of Ti and O. Both phases exhibit six fold symmetry, but in rutile each unit cell has ten nearest neighbors, while anatase has eight.[94] In addition, the anatase rings share four octahedral edges to only two shared edges in rutile, which contributes to the

greater relative stability of rutile.[76] The specific volume of the rutile cell is 62.420 \AA^3 while for anatase it is 68.454 \AA^3 . [90] The tighter structure of rutile explains the density difference.

Crystals have planes with different surface free energies, which partially determines the structure of the crystal. Therefore, the various crystal structures tend to have a signature distribution in a powder diffraction pattern as measured by x-ray diffractometry (XRD). For the bulk rutile phase of TiO_2 , the ratios of surface free energy on the various planes are $S_{110}:S_{100}:S_{101} = 1:1.41:1.53$. [95] The (110) plane has the lowest surface energy and thus is the most thermodynamically stable. Therefore, during unassisted physical vapor deposition of TiO_2 it is easiest to deposit rutile (110). [96] Rutile (110) also has the highest unit cell density, while rutile (100) has the lowest unit cell density. [52] Since each plane has a different atomic areal density, they also have a different combination of titanium and oxygen atoms. As a consequence the number (density) and type (Ti or O) of surface sites available for gas adsorption varies with each plane, which affects both the adsorption parameters and the electrochemical properties. Effective control of TiO_2 crystal orientation (or crystal texturing) gives the ability to alter the sensor response to various gases. [10]

The variations in electrical properties, photocatalysis, and adsorption parameters in the TiO_2 material system definitely affect the gas sensor response. In fact, the sensor response can vary directly with the anatase/rutile (A/R) percentage. Two examples, selective carbon monoxide (CO) sensing and humidity sensing, show how strongly these metrics can be linked. In MOS gas sensors, an n-type response is defined as a decrease in the resistance with

reducing gas concentration, while a p-type response would be the inverse. Savage discovered conditions of film impurity concentrations and partial oxygen pressures where the anatase portions of the sensor film demonstrated an n-type response to CO and CH₄, while the rutile portion exhibited a p-type response.[9] Of greater significance, the A/R percentage where this response crossover occurred was different for the two gases. As a result, an optimal A/R percentage (75% rutile) was demonstrated where the CH₄ response of the sensor is suppressed (canceled out by opposing reactions). However, a strong CO response can still be detected at this ratio, which allows the fabrication of a selective CO sensor. Both anatase and rutile have been used in the fabrication of humidity sensors. As part of the development for this application, both materials have also been extensively studied for the standpoint of water adsorption, desorption, and hydrophilicity. Anatase has been shown to have a greater water adsorption capacity, while the sticking coefficient for physisorbed water is greater for rutile films.[79] The anatase dominant films demonstrate greater sensitivity, but also have more hysteresis than the rutile films. The differences in each phase's sensor responses clearly illustrate the value of controlling the morphology in the fabrication of titania gas sensors.

The most direct way to transform the metastable titania phase to the stable rutile phase is through the application of a post deposition heat treatment (annealing). As mentioned previously, the onset of a metastable-stable transformation does not have an absolute temperature value, but is usually defined in a range. Since the transformation can be occurring (albeit at a glacial rate) at any time, it is only when this rate of change is measurable that the onset of this range can be determined. Often, the transformation rate

increases so rapidly that the change appears nearly instantaneous to experimental observations.

The key mechanism behind the formation of metastable polymorphs in titania relates directly to the grain size. As energy (heat) is applied to a sample, the molecules are able to diffuse (move around) in search of lower energy sites. Polymorphic creation requires the cooperative movement of the Ti and O atoms, as they rotate into positions rather than sliding across the surface in a simple diffusion process.[97] Formations of similar polymorphs aggregate into small grains. In general, larger grains sizes are more stable and the smaller grains coalesce to form these larger grains during annealing. At certain grains sizes, the surface energies of the anatase and the brookite molecular arrangements are more stable than the rutile arrangement. This factor accounts for the existence of the brookite and anatase metastable polymorphs. For grain sizes smaller than 11 nm, Zhang reported anatase is the most stable arrangement.[95] Similarly, brookite is the most stable form for grains sizes between 11 nm and 35nm, for larger grains (above 35 nm), the rutile arrangement is the most stable.[95] From a strict thermodynamic analysis, anatase would transform into brookite when the grains reached the critical size (> 11 nm), and thence into rutile at grain sizes larger than 35 nm. However, at this point, the kinetics associated with the transformation begins to play a significant role. The preferential kinetic pathway for anatase appears to favor a direct anatase to rutile transformation. Annealing studies of anatase films containing significant fractions of brookite before annealing showed little or no growth in the total brookite concentration as the films were annealed until completely rutile.[98] However, the onset temperature and the temperature range for anatase-rutile transformation increased with respect to the initial

brookite percentage.[99] The structure of anatase is much closer in shape to the rutile structure. An orientation relationship exists between certain planes of the newly formed rutile and the consumed anatase.[97] Several planes of rutile form parallel to the anatase planes, *i.e.* the [001] rutile zone axis is parallel to the [110] anatase axis, and have similar lattice spacing. This relationship may provide the explanation for the direct A-R transformation. The direct A-R transformation may also be the primary reason for the scarcity of brookite and the difficulty in isolating pure brookite.

In annealing studies under constant SEM observation starting with nano-anatase (< 8 nm grains), the critical size for the onset of the anatase-rutile transformation was found to be 13-14 nm.[83] However, the full transformation did not occur for grains of that size. Instead, after a gradual coalescing to this critical size, the anatase grains then rapidly grew to 200-300 nm, at which point the rutile transformation consumed the anatase. The final transformation was so rapid that repeated attempts were able to capture only a few micrographs which showed grains that had undergone a partial A-R transformation. The rapid grain growth in the anatase from 13-14 nm to the 200-300 nm range provides a kinetic pathway which bypasses the brookite formation and preserves the thermodynamic integrity vis-à-vis grain size equilibrium.

Several other factors can inhibit or encourage the transformation as evidenced by the dynamic nature of the transformation temperature range. The most critical appears to be the number of oxygen vacancies in the films.[88] Oxygen-depleted anatase transforms at much lower temperature ranges. Also, annealing of Ti and TiO films in oxygen forms TiO₂ films

with higher rutile ratios at lower temperatures than would be anticipated from comparison with TiO₂ anneal studies.[87] It is probable that oxygen vacancies act as nucleation sites, and thus trigger the onset of the transformation.

3.3 Titania Experimental Design

Electron beam evaporation was carried out on a custom vacuum system operating in the North Carolina State University BioMedical MicroSensors Laboratory (BMMSL). Experiments were performed when the base pressure of the system was less than 10⁻⁶ torr. The target-substrate distance was 39 cm which results in a highly collimated flux. Substrates for this work were 75mm Si (100) wafers. The depositions used a titanium source melt. The starting pressure during the depositions ranged from the base pressure to 5 x 10⁻⁴ torr and was controlled by the introduction of Ar and O₂ in a range from 0-40 sccm.

The substrates were mounted on an unheated rotating stage set at a highly oblique angle (80°) to the source. For these films the rotation speed and the deposition rate were controlled so that the pitch (deposition/revolution) was in the 5-10 nm/rev range. At these pitch values the films form into isolated vertical columns with a width on the order of 50-100 nm. The films thicknesses ranged from 120-800 nm. Scanning electron microscopy (SEM) was utilized to qualify the pitch values necessary for column formation and to view the sculptured thin films.

After deposition, samples were annealed at various temperatures in air to thermally oxidize any non-reacted Ti or TiO sub-oxides material, and to crystallize the films into either anatase or rutile TiO₂. For this work, two options were used for annealing. The first option is an open-air alumina hotplate (HP) anneal at a power setting of 120V (Variac) using a 100mm Si wafer as a susceptor. Thermocouple measurements indicate that temperatures were between 150-200 °C at the surface of the susceptor. The second option is an open-air tube furnace. Anneals in this furnace were done at temperatures up to 900 °C. For these experiments, the annealing times ranged from five minutes to several hours, but the focus was on using the minimum time and temperature (thermal budget) to achieve the desired results.

The XRD analysis was performed using a Bruker AXS X-ray diffractometer. The CuK α filament power settings are 40 kV and 30 mA (1.2 kW). The Bruker AXS has a general area detector diffraction system (GADDS) that can scan 35 degrees of the 2 θ range at one time for a given centered value, ω . For all of the data presented here, scans were taken for each sample at $\omega = 30^\circ$ and $\omega = 55^\circ$. For each film, the curves for both ω values are plotted. The advantage of the area detector lies in the time savings for each scan. It can be used to quickly identify phases, structures, and materials in the films.

Peak location was determined either by direct evaluation of the data or by using the cursor location function in the graphing package. Peak identification is determined by comparing the experimental peaks with the database of XRD powder diffraction files, also referred to as the JCPDS charts. Table 3-2 lists some of the primary XRD peaks used in literature to characterize the anatase-rutile formation in TiO₂.

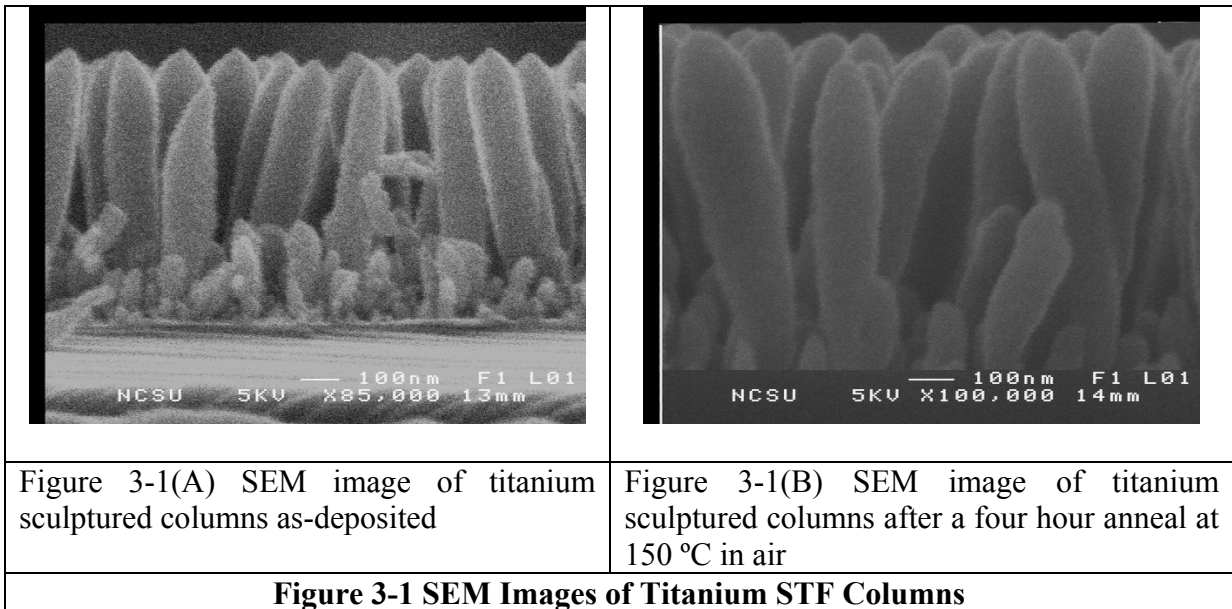
Table 3-2: Important TiO₂ XRD Peaks

Anatase TiO₂	2θ (degrees)	Intensity I/I₀
101	25.2	100
004	37.8	20
112	38.5	10
200	48.0	35
105	53.8	20
211	55.1	20
204	62.7	14
116	68.7	6
220	70.3	6
Rutile TiO₂		
110	27.4	100
101	36.1	50
111	41.2	25
210	44.0	10
211	54.3	60
220	56.1	20
002	62.7	10
301	69.0	20

3.4 Titania Morphology Results and Discussion

The initial qualification of the GLAD columnar films consisted of two main groups of titanium films. The first group were thicker films (>500 nm) and were deposited using a Ti source under vacuum conditions (<10⁻⁶ Torr). The second group of films were thinner (~100-200 nm) and were deposited using Ti with a small oxygen/argon flow to raise the ambient pressure to 10⁻⁵ Torr. Therefore, the chances of a gas phase reactive collisions between the Ti flux and ambient oxygen are significantly increased. The thicker films produced stronger (greater intensity) diffraction patterns than the thinner groups.

Figure 3-1(A-B) shows the SEM micrographs for the sculptured thin columns deposited under vacuum conditions. The micrograph in Figure 3-1(A) shows the as-deposited films, while Figure 3-1(B) shows the columns after a 4 hour hot plate anneal at 150 °C. Films deposited using the GLAD techniques are characterized by an initial growth period during which a high rate of column extinction exists until a quasi-stable ratio is achieved between the column spacing and the column density.[7, 17] This initial seed layer can be thought of as similar to the “scrub layer” on the surface of a forest. In both images, the first 100 nm of deposition exhibits this scrub layer appearance. After this point, the isolated nanoscale columns are clearly defined. The tops of the as-deposited films show clear faceting (points) which are an indication of crystalline formation. After low temperature (150 °C) annealing, the edges appear to be more rounded and less distinct.



For this first group with no oxygen flow, the as-deposited crystalline portions of the films were primarily TiO and Ti as expected. Figure 3-2 shows the raw XRD graphs for the various anneals on the Ti film depositions. The peaks of interest are near 32° which is most likely TiO(200), and the easily identifiable Ti(100) at 35.1° and Ti(101) at 40.2°. After as short as a five minute anneal at 150 °C, the crystalline TiO and Ti peaks have faded and the beginning of the rutile peaks are forming. Longer anneals at the same temperatures yielded more distinct rutile peaks. The 5 minute high temperature anneals (900 °C) completed the rutile formation. The XRD patterns for the high temperature anneals did not change significantly for longer times. However, note the dominant texture after annealing is near 62.7°. Ting identified this peak as Ru(200) in a titanium oxidation study.[100] From Table 3-2, the textures of Ru(110)-27.4°, Ru(211)-54.3°, and Ru(101)-36.1° have the highest powder diffraction intensities. These values differ from the texture shown here.

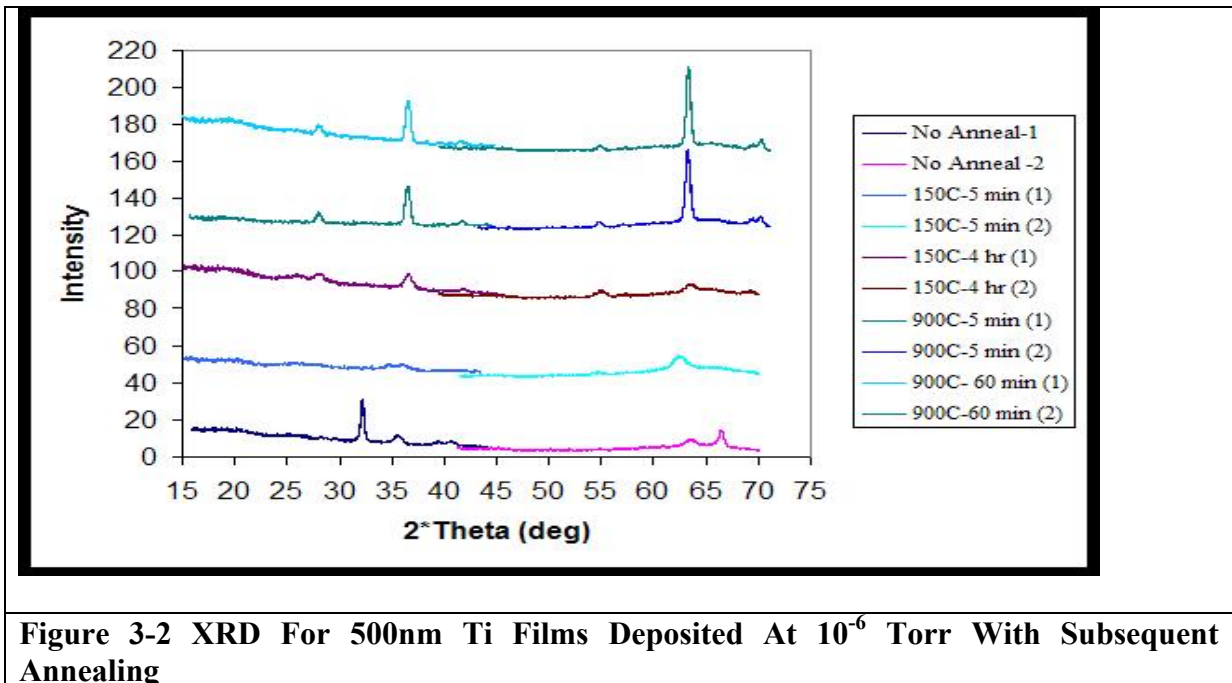


Figure 3-2 XRD For 500nm Ti Films Deposited At 10^{-6} Torr With Subsequent Annealing

The second group of films were thinner (~100-200 nm) and were deposited using Ti with a small oxygen ambient. The O₂ flow rate was 20 sccm which raised the pressure in the deposition chamber to ~10⁻⁵ Torr. Figure 3-3 shows the XRD curves for these reactive TiO_x depositions. As deposited the films were almost completely amorphous. The annealing processes were five minutes in duration for the data in Figure 3-3. For the lower temperature anneals (<900 °C), there was significant formation of anatase, A(101) at 25.3°. However, even the 150 °C samples have some rutile present. Longer anneal times increased the amount of rutile for all temperatures. The 900 °C anneals were almost completely rutile. However, for these films the dominant rutile texture was R(110), while the R(002) peaks were very small. This rutile texture differs significantly from the pattern in Figure 3.2.

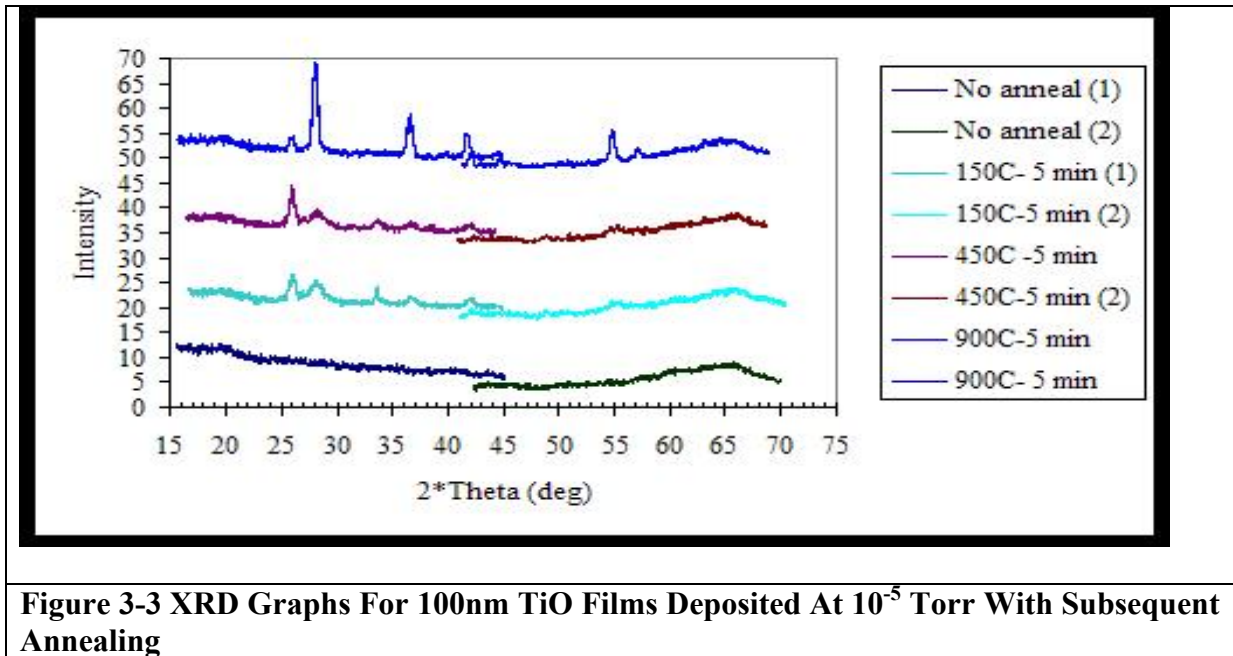
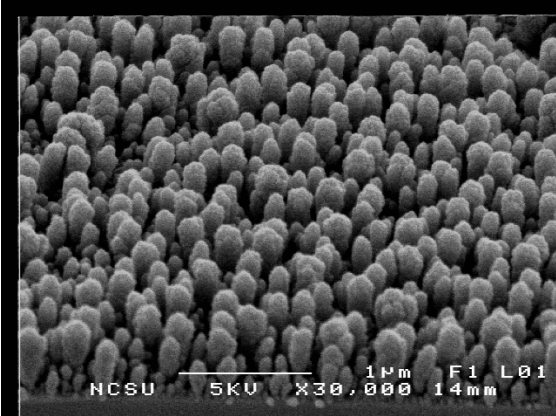
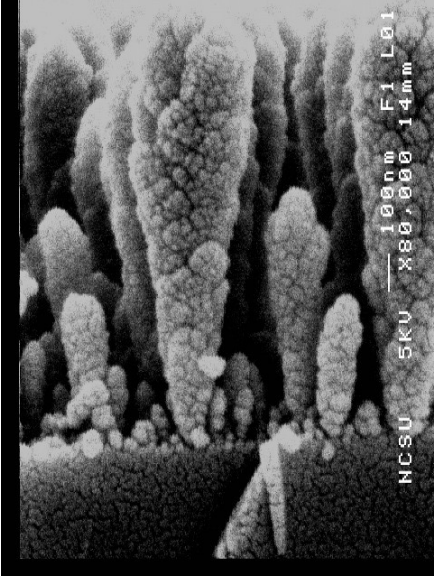


Figure 3-3 XRD Graphs For 100nm TiO Films Deposited At 10⁻⁵ Torr With Subsequent Annealing

Increasing the ambient pressure also adversely affects the collimation of the flux as it reaches the substrate. Therefore, the shadowing effects are diminished and the features of the nanocolumns are less defined.[53] In addition, the column widening effect is increased. Figure 3-4(A-B) shows the planar (A) and cross-sectional (B) SEM images for thicker films deposited at the same ambient conditions as those in Figure 3-3. The columns have a bulbous texture, with little or no faceting evident. This result is consistent with the amorphous measurements indicated by the XRD characterization of the as-deposited films.

	
<p>Figure 3-4(A) Planar SEM image of TiO_x sculptured films deposited with 20 sccm O₂ flow (10⁻⁵ Torr)</p>	<p>Figure 3-4(B) Cross-sectional SEM image of TiO_x sculptured films deposited with 20 sccm O₂ flow (10⁻⁵ Torr)</p>
<p align="center">Figure 3-4 SEM Images of TiO_x STF Pillar Structures</p>	

Since anatase and rutile TiO₂ possess different characteristics in both electrical conduction and surface interactions, it is desirable to control the A/R percentages in the STF sensors.

This control enables one to distinguish the unique characteristics of the materials, and provides more certainty to the repeatability in sensor design and development. Optimal control would result in films that were 100% anatase or 100% rutile.

The initial crystalline TiO₂ films produced with the BMMSL reactor all had a significant amount of rutile present as determined by XRD. Since rutile is the thermodynamically stable phase, it is not possible to reverse the A/R transformation using thermal processing. In addition, sufficient temperature and time will completely transform all of the films to rutile. Annealing the samples over one hour at 900 °C produced films with no evidence of anatase for both deposition conditions described to this point. However, the need to have a bottom electrode (Pt) in place before the initial deposition requires that the post-deposition anneals be limited to temperatures below 700 °C for the platinum to maintain adhesion to the substrate. Therefore, it is necessary to determine which factors during deposition will affect the subsequent phase formation and develop a pathway to control the final sensor composition.

From the previous sections on the A/R transformation, several points are critical to the design of this experiment. A primary factor in the onset of rutile formation is the number of oxygen vacancies in the films. Several groups have reported an increase in rutile formation when the initial deposition pressure was 10⁻⁵ torr or below, which would imply films with more vacancies.[80, 87, 96, 101-103] Larger number of vacancies can also lower the temperature range of the A/R transformation during annealing. Therefore, it appears that using higher oxygen partial pressure during deposition can improve the anatase percentage in the films.

However, as the pressure increases the number of gas-evaporate collisions also increase leading to a decrease in the flux at the wafer (dep rate) and a decrease in flux collimation. An experiment was designed to study the effect of higher O₂ partial pressures (increased O₂ flow rate), and at higher total pressure using increased Ar flow rates. Three TiO_x process recipes were developed based on the previous process. Table 3-3 lists the differences in deposition flow rates. After deposition, anneals were done at 450 °C-5 minutes (the anneal ID is J in the graphs), 650 °C-5 minutes (ID-M), and 900 °C-5 minutes (ID-K) in an open tube furnace.

Table 3-3 Experimental conditions for the effect of oxygen partial pressure during deposition on subsequent rutile/anatase formation

Wafer ID	Deposition Condition
30130	Control - 20 sccm O ₂ , 1 sccm Ar
30723	Higher Ar Flow – 20 sccm O ₂ , 4 sccm Ar
30722	Higher O ₂ Flow – 40 sccm O ₂ , 1 sccm Ar

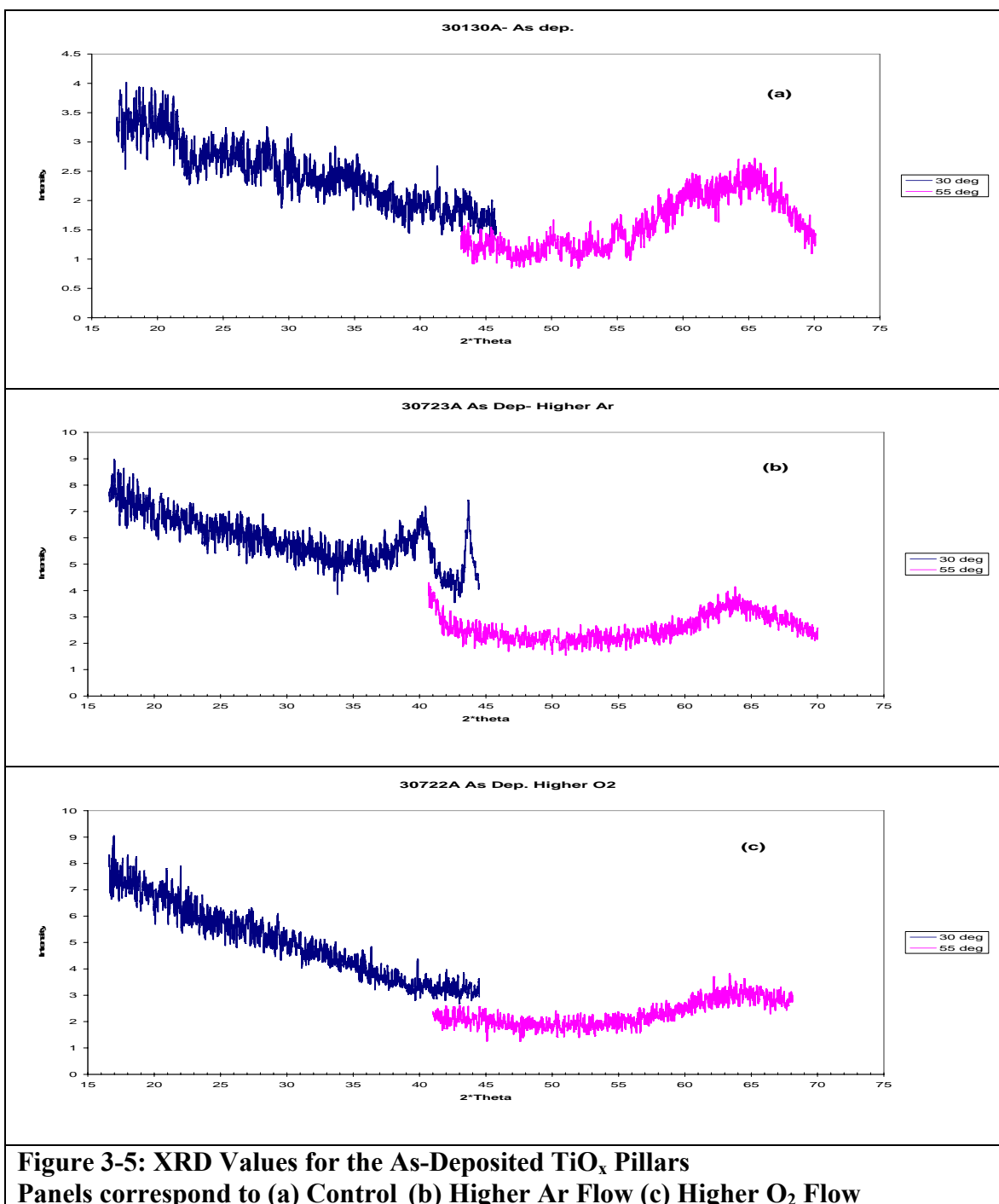
The results from the XRD analysis are shown in Figure 3-5 (a-c) for the as-deposited films, Figure 3-6 (a-c) for the 450 °C anneals, Figure 3-7 (a-c) for the 650 °C anneals, and Figure 3-8 (a-c) for the 900 °C anneals at the end of this document. In these figures, the (a) frames contain the results for the control sample of 30130, the (b) frames show results for the higher Ar flow rate sample 30723, and the (c) frames contain results for the higher O₂ flow rates of sample 30722.

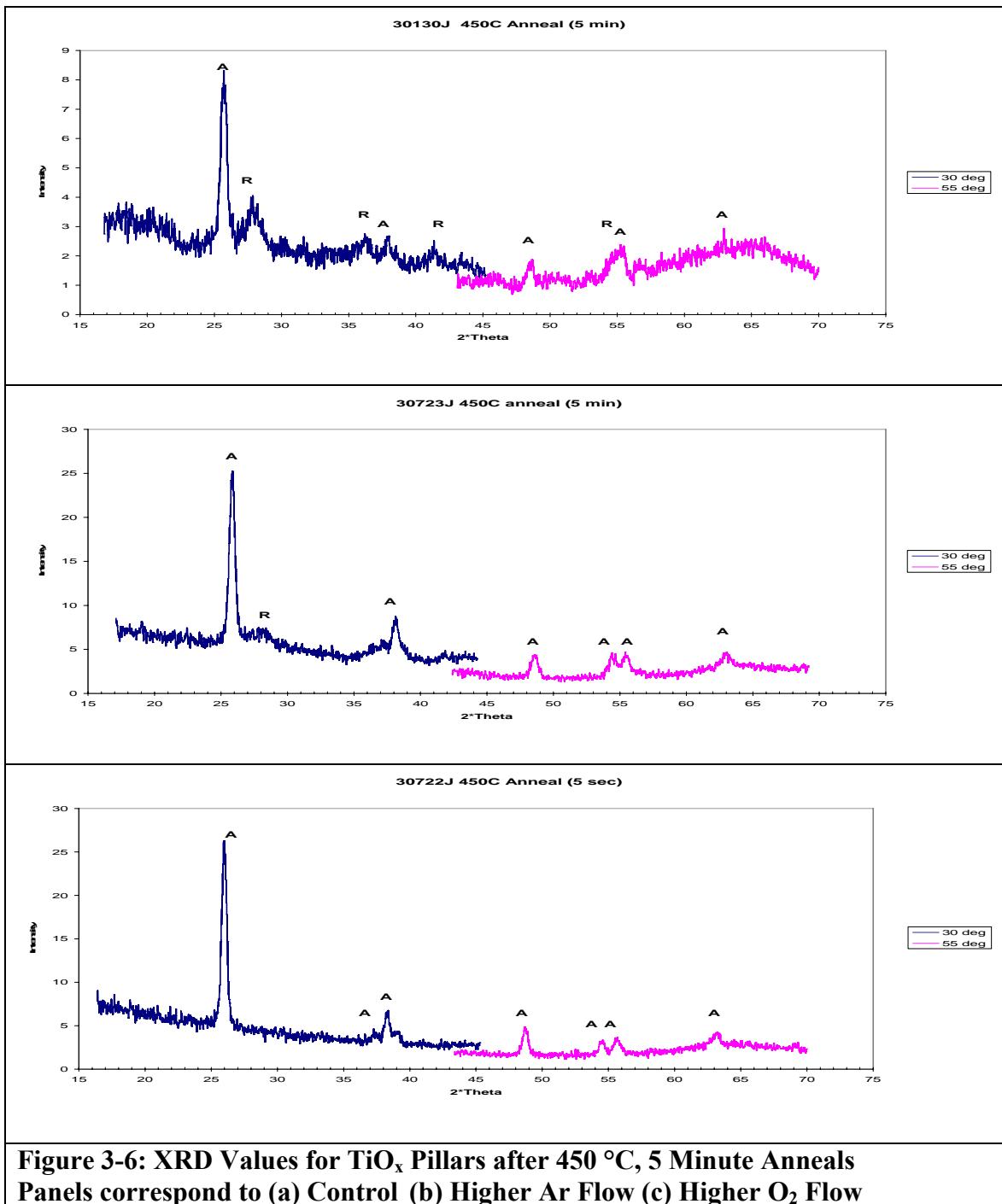
Figure 3-5 shows the XRD patterns for the as-deposited films. In general, no clear indications of sizable grain structures exist in the as-deposited films except for the wide peak at 40.5°

and a sharp peak at 44° on the 30° -centered scan for frame b. The 40.5° peak is probably Ti(101) and is confirmed by the 55° -centered scan. However, the 55° -centered scan did not register the 44° peak. It is a measurement artifact related to the aluminum holder for the Bruker XRD. For the (J) 450°C anneals in Figure 3-6, strong crystalline patterns emerge. The control sample shows mostly anatase peaks, but with definite indications of large grain rutile formation, especially at the characteristic 27.4° Rutile (110) peak. Frame 3-6(b) has some rutile formation (smaller relative peaks than the control), while Frame 3-6(c) has little or no rutile formation with many anatase peaks. The 650°C anneals (Figure 3-7) for frames (a) and (b) again show mostly anatase, but the relative heights of the rutile peaks have increased slightly. There is still little indication of rutile formation present in sample (c). Finally, after 900°C anneals (Figure 3-8), the rutile peaks are the dominant features for both the (a) and (b) samples. However, there is little indication of rutile formation for the oxygen rich films (sample 30722) even after the brief high temperature anneal.

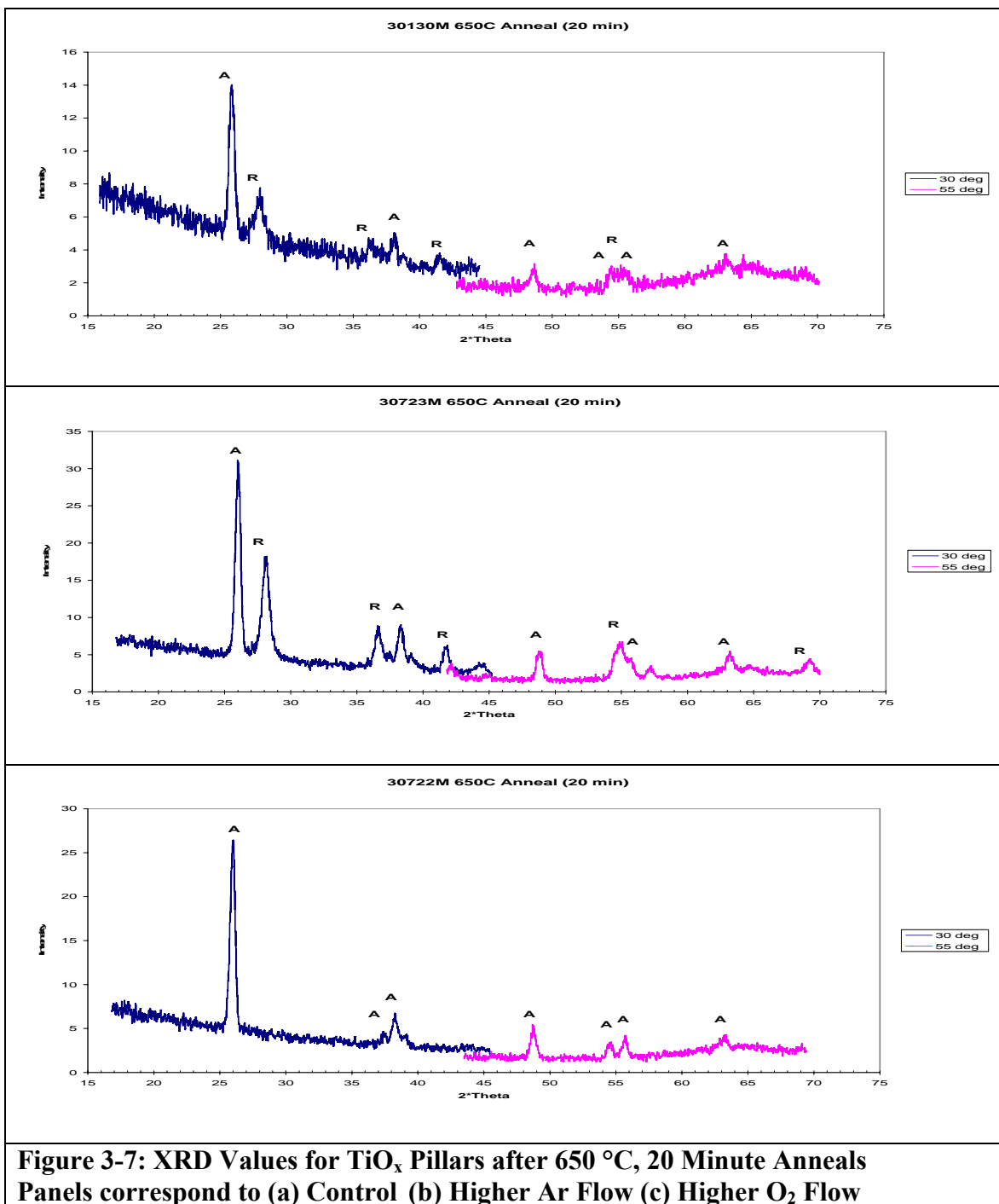
All of the films in this phase of the research were more amorphous initially, and had less rutile texture evident in the as-deposited films, as compared to films deposited before the 30130 samples. In addition, the short high temperature anneals (5 minutes at 900°C) did not produce fully rutile films in the oxygen rich depositions. The primary difference between the later films (Figures 3-5 through 3-8) and the previous reactive evaporations (Figure 3-3) was the significantly greater thickness (at least 8X) of the more recent films. This point implies that the percentage of crystalline formation is greater in the initial seed (or interface) layer near the Si surface. Also, the thicker films might simply require longer anneals to complete the A/R transformation.

The data clearly shows that the lower partial pressure of O₂ during deposition increased the percentage of rutile formation. This effect is evident across all variations of post-deposition anneals. Since it is likely that the reduced oxygen partial pressure results in more oxygen deficiencies in the films, these results are consistent with the supposition that the oxygen vacancies act as catalysts for the A/R transformation. Finally, as expected from the thermodynamics of the titania system, higher annealing temperatures also increase the percentage for rutile. It remains to be investigated if annealing in an inert or reducing environment will lower the temperature threshold for the onset of A/R transformation.





**Figure 3-6: XRD Values for TiO_x Pillars after 450 °C, 5 Minute Anneals
Panels correspond to (a) Control (b) Higher Ar Flow (c) Higher O₂ Flow**



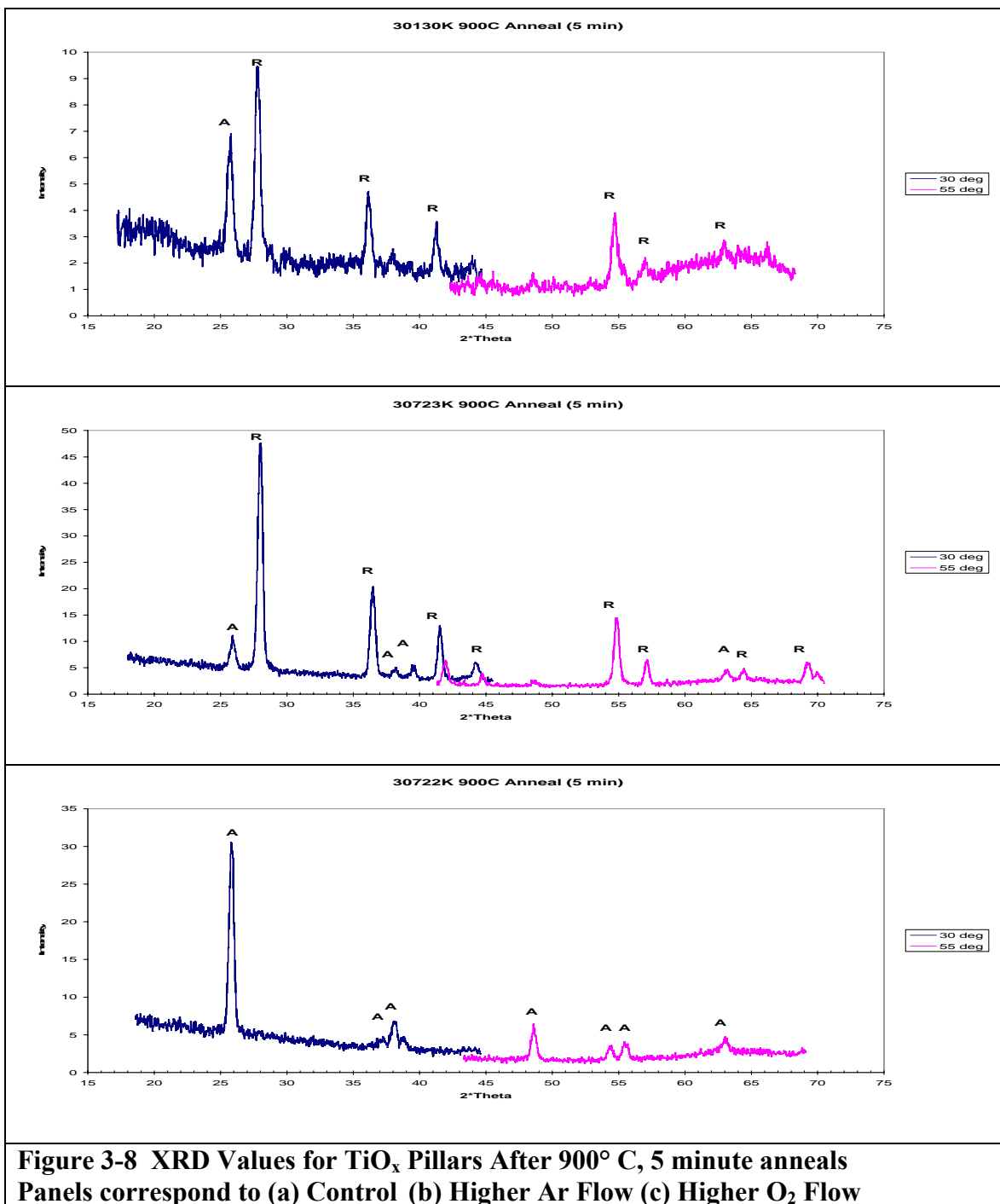


**Figure 3-8 XRD Values for TiO_x Pillars After 900° C, 5 minute anneals
Panels correspond to (a) Control (b) Higher Ar Flow (c) Higher O₂ Flow**

3.5 Titania Morphology Conclusions and Future Work

The strong evidence of the effect of deposition O_2 pressure on subsequent A/R percentages lends support to the supposition that oxygen vacancies play a key role in the A/R transformation. More importantly, it provides a promising pathway for the creation of both primarily anatase and primarily rutile sensors. Films deposited at higher oxygen ambient pressures will have greater anatase percentages, while lower oxygen ambient pressures produce films with higher rutile percentages. Also, the crystal texturing of the rutile films changes with respect to the initial deposition conditions and the annealing pattern. In addition, it is possible that rutile formation may be enhanced at lower annealing temperatures using oxygen-depleted atmospheres during annealing. This factor is important in order to incorporate metal electrodes into the sensor elements and to integrate these sensors into standard IC processing.

Chapter 4

Effect of Annealing on the Structure and Morphology of STF Films

This chapter investigates the effect of annealing on the structure and morphology of sculptured thin films (STFs). The typical STF structure is an isolated, self-similar construct on a nanometer scale. Therefore, each structure can react to external influences independently of the other structures, i.e. as a separate, albeit similar system. This small scale system “independence” allows the nanostructures to exhibit different material characteristics than conventional thin films. An important example of this phenomenon concerns the primary crystallographic alignment or “texturing” of the structures. Some sculptured thin films have demonstrated highly ordered crystallographic texture.[15, 74, 104-107] But the reasons for this texturing have not been widely investigated, especially in the area of metal oxides formed/enhanced by post-deposition annealing in oxygen.

4.1 Introduction to Annealing

The introduction provides a review of several key aspects of annealing with respect to thin films and crystal texture. These aspects include (1) background on the annealing process as well as a description of crystal texture, (2) the highly ordered texture reported for some as-deposited STF materials and the prevailing reasons for this effect, and finally (3), the reported effects of annealing on various STF structures and materials.

4.1.1 Annealing and Crystal Structure

The term “annealing” has become synonymous with heat treatment, but has its origins in metal working or metallurgy. Formally, the anneal process is a heat treatment to remove damage (dislocations or defects) from a crystal (metal) and consists of three stages; recovery, recrystallization, and grain growth.[108] Annealing is often described in terms of a “thermal budget” or time at a specific temperature. Increasing the thermal budget in terms of either the annealing time or the temperature in general enhances the effect of the process. Crystalline materials that have been placed under stress can undergo plastic deformation resulting in defects or dislocations in the lattice structure. These defects represent an increase in the free energy of the system by relieving the strain, and are thermodynamically unstable. However, at room temperatures the atomistic forces (i.e. diffusion) that are working to eliminate these defects are too slow to be observable for many materials. These processes are generally thermally activated and increase their rate with an increased temperature.

As mentioned, the typical metallurgical annealing process has three stages. In the recovery stage, the dislocation is annihilated, modified, or moved within the deformed structure to a more energetically favorable position. Upon further annealing, the atoms around the recovered defect site form new dislocation free grains within the original polycrystalline structure. This stage is called recrystallization. However, after recrystallization within a specific deformed structure, the original grain boundaries of the material still exist. The final annealing stage, grain growth, occurs as the grain boundaries migrate and the grains coalesce into large grain sizes.

These metallurgical effects also produce other changes in the material that often are the primary impetus for annealing. For example, grain growth usually results in a densification of the material as voids present along the grain boundaries are eliminated or reduced. Also, the net effect of crystallization and increased grain size is an increase in the crystallinity of the films, which can also increase the degree of crystallographic texturing. Many vapor deposited thin films have an amorphous texture as deposited and subsequent annealing steps are used to produce polycrystalline films.

While the preceding has described the formal process of annealing within its metallurgy, the term “anneal” has come to be identified with almost any heat treatment. Often, it is necessary to change the solid phase of a material to one of its more stable polymorphs. An example of this process is the change of anatase TiO_2 to rutile TiO_2 . Anatase will usually transform to the stable rutile phase at temperatures in excess of 800 °C.[97] One trigger for the transformation is the grain growth of the metastable phase. This process was described in detail in the previous chapter. Another “annealing” process involves the activation of dopants (boron, arsenic, etc) in semiconductor (silicon) device fabrication. In order for the dopants to be electrically active they must replace a silicon atom in the lattice structure, rather than occupy a position between lattice sites (aka interstitial sites). The maximum amount of dopants that are in the lattice is directly related to the solid solubility of the particular dopant in silicon, and therefore, a strong function of the annealing temperature. A final example stretches the definition of annealing, but is a standard process for producing metal oxide thin films. This process, thermal oxidation, is an annealing step which is performed in an oxygen

rich ambient where significant oxidation of the deposited material occurs. One example of this process would be a deposition of titanium thin films, with a subsequent thermal oxidation to produce the desired form of titanium dioxide.[109] Depending on the deposition conditions, the as-deposited film may be primarily Ti metal, contain significant amounts of Ti_xO_y sub-oxides, or be mostly TiO_2 (often with significant oxygen depletion).[86, 109] Although this type of thermal oxidation process does not technically qualify as annealing, the crystallization, grain growth, and phase change processes can occur along with the oxidation during a typical thermal oxidation run. This type of process is used in our sensor development and will therefore be included in this discussion.

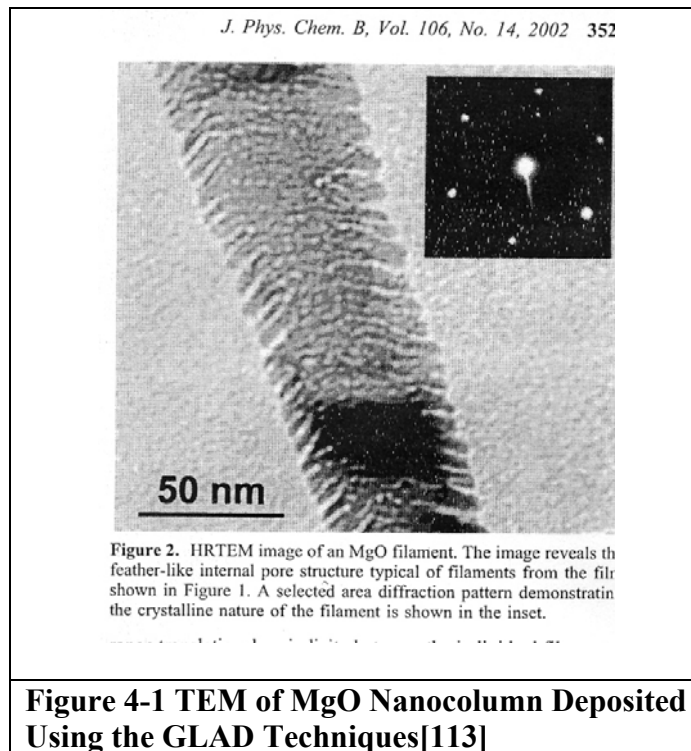
The term crystal texture refers to the degree of alignment of the crystals within a particular sample. An ideal single-crystalline material (no defects) would have perfect texture with every crystal aligned in one orientation. Conversely, in a completely amorphous material the orientation of every crystal would be random. The degree of texturing is often referred to by the labels of weak, moderate, or strong texture. The crystallinity and texture of thin films is most often determined by X-ray diffractometry (XRD), reflection high energy electron diffraction (RHEED), or by the electron diffraction methods available with transmission electron microscopy (TEM). The texture of a film is important for sensor technology because the various faces/planes of a crystal contain different configurations of atoms and therefore have different properties. One critical example of the need for texture control would be with magnetic materials. The location of the hard and easy axis of a magnetic material depends on the alignment of the crystal.[105]

In physical vapor deposition, the orientation of the molecules striking the surface is completely random. Therefore, the degree of crystallinity and the texturing are determined by the surface interactions. Materials that have a limited surface mobility (i.e. high melting point materials deposited at room temperature) tend to form amorphous films. Metal films, on the other hand, usually have a high degree of crystallinity. Obviously, increasing the substrate temperature increases the surface mobility and hence the degree of crystallization. In the absence of other factors, films form in the orientation which minimizes the surface free energy. However, this orientation may produce a lattice mismatch between the substrate and the bottom surface of the films. The mismatch introduces strain into the film, which changes the minimum energy equation. For normal incidence depositions, the crystal orientation is determined mostly by this competition between the minimum surface energy and the degree of strain produced at the substrate interface. Since the strain increases with film thickness, there exists a “critical thickness” for each film/substrate combination at which the strain induces the orientation of some of the grains to shift, thereby introducing a grain boundary. Over the course of the deposition, these grain boundaries can shift multiple times producing polycrystalline films. The use of lattice matched substrates has often been used to influence the texture of deposited films. The process conditions also play a key role in the crystallinity of deposited films.

4.1.2 Effects of Glancing Angle Deposition on Crystal Texture

Many of the sculptured thin films discussed in the literature have been deposited under conditions that produce amorphous films[73, 110-112], and these will be discussed under the

annealing section. However, among the films which produce crystalline STF structures as deposited, a high degree of texturing can exist across the system. Dohnalek reported the phenomena based on reactive depositions of MgO on various substrates.[113] Figure 4-1 shows the TEM image of a single MgO column with diffraction pattern inset. Note the featherlike internal pores of the column showing a large amount of surface area. The clear dots in the inset diffraction pattern indicate the crystalline nature of the column. However, the XRD patterns of the whole films provided the more interesting results. The long axis of the columns deposited on Mo(100) substrates were strongly aligned along the [111] MgO crystallographic direction. This result was not surprising as MgO grows epitaxially on Mo(100) due to their lattice match. But the columns grown on Si(111) were strongly aligned along the MgO[211] direction, which was completely unexpected.



The reasons for the strong texturing are believed by several groups to be related to the concept of “evolutionary selection” described by van der Drift in 1967 which states for the deposition of closely packed polycrystalline films the grains of the film which grow the fastest will dominate and shadow the other grains.[15, 74, 104-107] Since the whole concept of sculptured thin films is based on self-shadowing and the extinction of slower growing features, this theory aptly describes the expected growth in the initial STF formation. In many cases, the texture growth dynamics for STF structures are radically different than those observed for normal incidence deposition. For example, with ruthenium deposited on p-type Si(100), the normal incidence depositions have a strong {1011} texture, a moderate {0002} texture, and weak {1010}, while the obliquely deposited STF pillars ($\alpha = 85^\circ$) have only a strong {1010} texture.[74] The texture which dominates the growth is the one which has the highest growth rate in the vertical direction as a function of the incident flux angle (α). Due to the isolation of the structures, and the small substrate “footprint” of each structure, the large scale movement of grain boundaries is absent in these films.[114] In effect, the “critical thickness” which defines the upper limit for epitaxial or single crystalline growth is extended for the independent STF structures. This feature has led to the first reported growth of single crystalline β -phase tungsten by evaporation.[115]

4.1.3 Annealing Effects on STF Structures

The first annealing effect to be addressed is the effect of densification on the physical stability of the STF structures. One of the earliest investigations into the stability of STFs

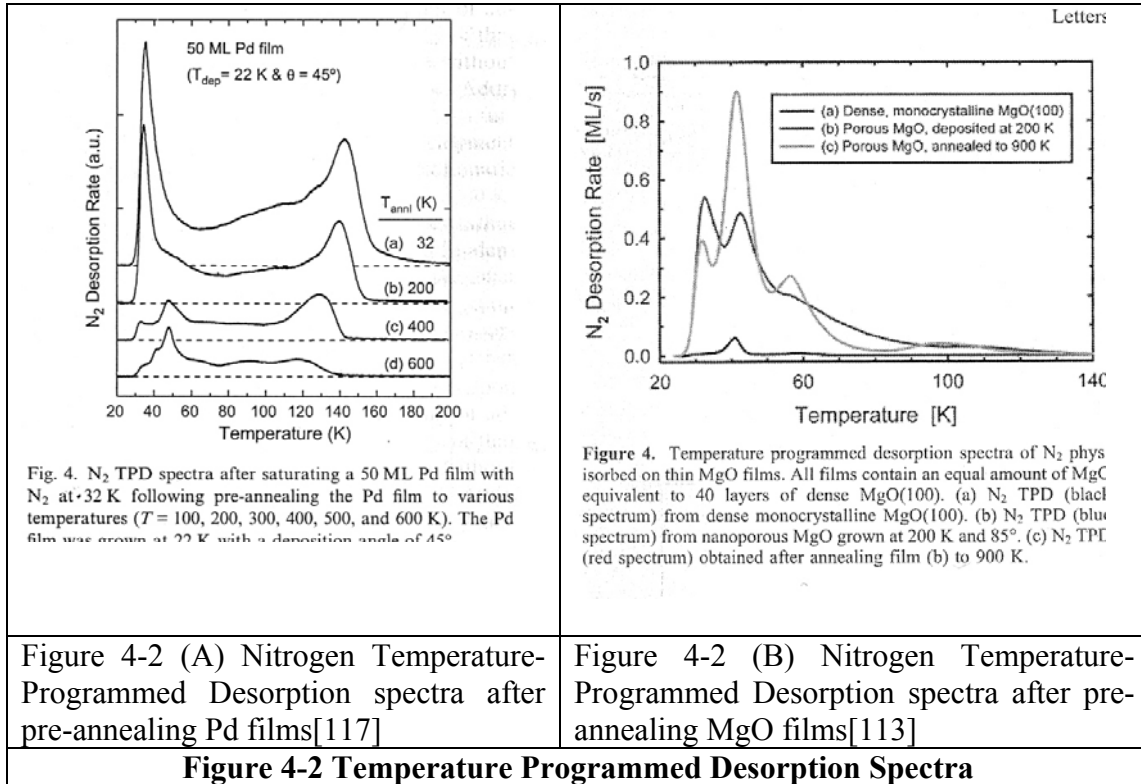
with respect to annealing was reported by Suzuki in 2001 using TiO₂ STFs deposited by reactive evaporation of Ti₂O₃[112] The study looked at isolated column shapes ranging from thin pillars (nail), striated columns (screw), helical coils (spring), and four layer chevron formations. Anneals were done in air at 500 °C for one hour. The isolated structures (nails, screws, and springs) exhibit little or no visual (by SEM) change in either structural integrity or thickness (pillar height). However, the chevron formation thickness decreased by more than 10%, and there were many broken columns and debris apparent in the SEM images. From a visual perspective, the chevron features are closely packed and the individual features appear to be in contact. In addition, the largest grain size (as determined by post-anneal XRD) for the annealed pillar and helical columns was on the order of the pillar widths, while the grains sizes recorded for the annealed chevron films were several times larger. The existence of these larger grains also indicates the chevron features were in contact with each other, with grain growth during the anneal spanning several features. The stresses caused during the annealing by this contact and the cross feature grain growth produced the physical damage to the features. However, the isolated structures show a robust physical stability under these moderate annealing conditions.

The stability of the columns as determined by SEM and thickness measurements is consistently reported for isolated columnar structures. Densification as determined by the change in thickness (pillar height) of less than 10% has been reported for carbon[110], tungsten[115, 116], TiO₂[73, 112], silicon[111, 116], and MgO[113] using annealing conditions typical for these materials. However, none of these studies looked at a broad range of temperatures. Under some annealing conditions (and materials) significant changes in the

pillar dimensions can occur. Pillars of 50 nm of europium oxide atop 400 nm of yttrium oxide had a height reduction of over 33% after a 900 °C, 75 hour anneal and showed significant column broadening.[73] Also, the melting point of Cu nanorods (550 °C) was found to be significantly lower than that of continuous Cu films (1083 °C).[75]

Another way of determining density (or more accurately porosity) for these films is using desorption studies. Two studies of temperature programmed desorption (TPD) of N₂ on Pd[117] and MgO[113] nanocolumns support the idea that while the macroscopic properties of the nanocolumns are only slightly affected by the annealing, the individual columns do undergo densification and increased crystal ordering. From the earlier figure (4-1) of the TEM of an MgO filament, there was a featherlike pore structure evident, indicating a large number of surface sites for adsorption. The TPD results for Pd and MgO are shown in Figure 4-2 (A) and (B) respectively. With the N₂ desorption studies, the lower temperature peaks represent bonding sites with weaker interactions, which are generally the smaller pores. The total number of sites is represented by the area under the desorption curve. For the Pd films in panel (A), the increasing anneals thru 400 K remove the large peaks below 40 K on the TPD spectra, indicating the many small amorphous pores have annealed out. The total surface area has been reduced by ~60% after the 400 K anneal. The 50 K peak on the TPD curve which begins to appear after higher annealing temperatures corresponds to a known peak for Pd(111) terraces. For the MgO films in panel (B), the overall number of sites stays equivalent after anneal, but the peaks have shifted to primarily at 42 K, which is a well-known desorption value for MgO (100) terraces and to 56 K which corresponds to MgO

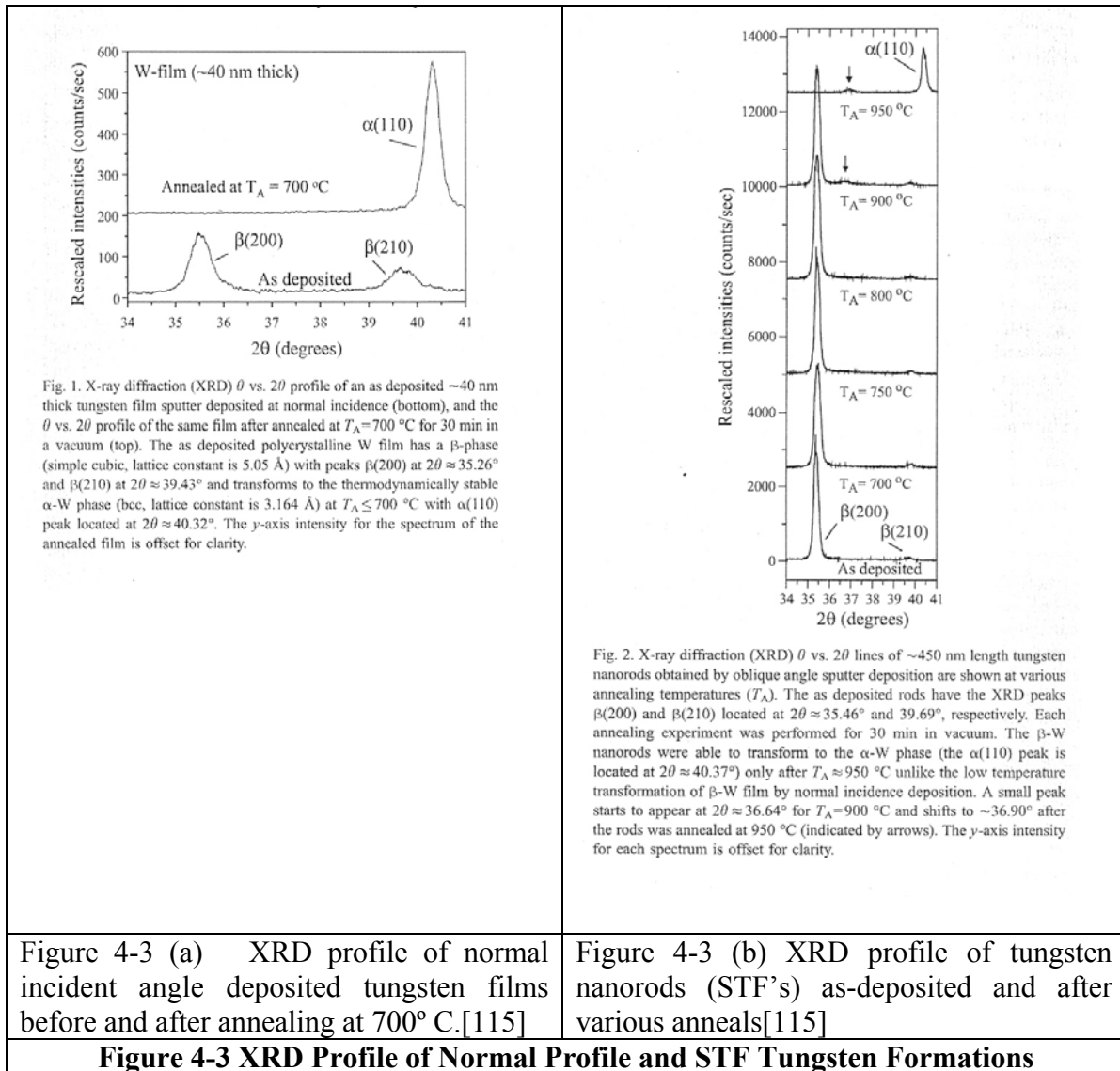
(100) defect desorption. These results imply an increased ordering (crystallinity) within the individual fibers and the elimination of very small pore features.



One of the primary reasons for post deposition annealing is to increase the crystallinity of the films, especially the films which are amorphous as-deposited. Many of these initially amorphous films have been the focus of annealing studies, with fairly consistent results. In general, isolated columns or structures (no column interaction) retain their macroscopic (SEM) shape integrity. In all cases, the annealing increased the crystallinity of the initially amorphous films, as determined by a broad spectrum of measurements. The physical changes that were observed were at the small grain scale (1-20 nm) and consistent with recrystallization and grain growth. As previously mentioned however, most of these studies

used a tube furnace with typical annealing conditions for the particular material system. There were few studies with variations in the annealing conditions to investigate any effect of the STF structure. Surprisingly, the detailed studies on texture evolution during the oblique depositions of Cu and Ru did not include any post-deposition annealing studies.[74]

A marked exception to this lack of post-deposition annealing studies was the phase change study on β -W nanorods. An excellent example of the effect of the STF formation on a thermally activated phase change has been reported for the tungsten system.[115] Tungsten, W, has a stable α -phase with a body centered cubic structure, and a metastable β -phase which has an A15 cubic structure. Typically, the upper annealing temperature range required for the β -W to α -W transformation has been reported as ~ 650 °C. But, the annealing studies by Karabacak on single-crystalline β -phase W nanorods showed the transformation temperature to be over 900 °C. The XRD results for these annealing experiments on both normal incidence W films and the W nanorods are shown in Figure 4-3 (A) and (B). In the (A) panel, the transformation from β -phase has clearly taken place after the 700 °C anneal as evidenced by the disappearance of the $\beta(200)$ and $\beta(210)$ peaks on the upper (700 °C anneal) XRD trace. In the (B) panel, a similar change in the XRD pattern does not occur until the 950 °C anneal. This tungsten phase transformation has been linked to the removal of oxygen from the β -W lattice. Therefore, Karabacak speculates the single crystalline nature of their β -W nanorods was the reason for the increased transformation temperature. The lack of significant grain boundaries would inhibit the removal of oxygen from the lattice since the grain boundaries serve as diffusion paths.



4.1.4 Thermal Oxidation of Sculptured Thin Films

The concept of crystal texturing of metal oxide structures formed by the thermal oxidation of metal STF nano-columns has not been widely researched. Most of the reported literature on STF crystal structure has focused on metal depositions. Also, the metal oxide STF literature

has concentrated on oxides that were initially deposited in crystalline form (MgO)[113] or deposited as an amorphous film and subsequently annealed (TiO₂).[73] Although the research to date has been limited, there are several reasons why the thermal oxidation of textured metal STF structures is of interest.

The concept of oxidation anisotropy holds that the oxide growth rate varies for different crystal surface planes during an oxidation process. The concept is a central tenet of the well-known Deal Grove model for the oxidation of silicon and has been reported for many other metal-oxide systems.[118-121] The effect is thought to be related to the epitaxial nature of the metal-metal oxide interface, in which the oxide grows with the structure that is most closely lattice-matched to the metal plane.[121] This concept implies that the orientation of the metal oxide is closely related to that of the starting metal. Therefore, both the degree of texturing and the orientation of the final oxide could be controlled through the initial source material. Once again, the titania system provides the proof of concept for this idea.

Although the oxidation of STF materials has not been widely reported, there has been extensive research on the oxidation process. Several groups have looked at the dynamics of titanium deposition and subsequent thermal oxidation to form TiO₂.[100, 109, 118, 121-124] It is difficult to form anatase films via this method due to the high temperatures required and the large number of oxygen vacancies (a trigger mechanism for rutile formation) that are inherently formed during intermediate steps in an oxidation process.[100] As a result, the groups have concentrated on rutile formation. From the rutile standard powder diffraction file (JCPDS No. 121-1276), the three primary XRD peaks for rutile are Ru(110) at 27.4°,

Ru(211) at 54.3°, and Ru(101) at 36.1° which have respective intensities of 100, 60, and 50. Therefore, the Ru(110) plane has the lowest surface energy for rutile films. Typical studies on the oxidation of weakly textured or mostly amorphous Ti thin films have shown that sufficient oxidation time and temperature to completely oxidize the films results in XRD patterns consistent with the standards.[100, 109, 121] However, the crystallinity of the deposited metal can be increased by increasing the substrate temperature during deposition. By using a substrate (fused silica) temperature of 500 °C during the initial Ti sputter deposition, Ting produced a strongly textured Ti(002) film as deposited which subsequently led to a strongly textured Ru(200) film upon oxidation.[121] This result strongly supports the supposition that the oxide morphology can be controlled through the starting material morphology. The high degree of crystallinity achievable using glancing angle deposition techniques should provide a solid opportunity to explore this area for oxidation.

The thermal oxidation of thin films also have several issues relating to the “top-down” nature of the typical thin film oxidation process that become more relevant with thicker initial films. In a standard oxidation process, the initial oxidation rate is very rapid, due to the abundance of oxygen atoms available on the surface and in the (assumed) oxygen-rich ambient. After this initial stage, however, the oxygen atoms must diffuse from the surface to metal-metal oxide interface for the reaction to continue. The term “top-down” describes this movement of the metal-metal oxide interface from the initial surface towards the bottom of the metal layer (i.e. the metal-substrate interface). This diffusion rate is often the rate limiting factor for the process. As the initial metal thickness is increased, the diffusion effects become greater throughout the process.

In addition to the decrease in oxidation rate, several other issues become important with increasing metal thickness. While the oxide grows with the most favorable epitaxial matching, some degree of lattice mismatch is almost always present. As the oxide layer grows, so does the strain induced by the metal-metal oxide interface mismatch. This strain can affect the adhesion between the metal and the substrate leading to flaking. Longer anneals or higher temperatures increase this effect. Using the rutile system as our example again, the maximum Ti film thickness that could be oxidized into a stable, adherent rutile layer on a Si(100) substrate was approximately 570 nm.[109]

Another effect of the “top-down” diffusion is the formation of sub-oxide materials due to the lack of sufficient oxygen to complete the process, i.e. Ti_2O or $\alpha-TiO$ in our example. These incomplete oxidation paths require longer oxidation anneals or higher temperatures to complete the formation of TiO_2 . Also, the sub-oxide grains disrupt the crystallinity of the source material (the initial Ti film) and therefore can influence the texturing of the final oxide. In the titania system, large concentrations of oxygen vacancies in the films dramatically favor rutile formation, thus further inhibiting the ability to form the anatase phase using this oxidation method for thicker titanium films.

Since the STF nano-columns are exposed to a supply of oxygen from the top of the columns all the way to the base, the oxidation process must occur differently than in the “top-down” model. The typical width of the columns is less than 100 nm, so the maximum diffusion path for the oxidation process is 50 nm. In addition to the metal texturing discussed initially, the

multi-directional oxidation process occurring with these nano-columns should provide interesting research results.

4.2 Annealing Experimental Design

Electron beam evaporation was carried out on a custom vacuum system operating in the North Carolina State University BioMedical MicroSensors Laboratory (BMMSL). The base pressure when these experiments were performed was less than 10^{-6} torr. The target-substrate distance was 39 cm which results in a highly collimated flux. The depositions used a titanium source melt. The initial pressure during the depositions ranged from 1.7×10^{-7} torr to 5×10^{-4} torr and was controlled by the introduction of Ar and O₂ from 0-40 sccm.

The substrates were mounted on an unheated rotating stage set at highly oblique ($> 76^\circ$) angles to the source. The flux angle of incidence, α , was 80° for most of the depositions described here. However, for selected depositions stage was mounted at 76° , 82° , or 85° . For these films the rotation speed and the normal incidence deposition rate were controlled so that the pitch (deposition/revolution) was in the 30-60 nm/rev range. The deposition rate was determined by a crystal rate monitor. At these pitch values the films form into isolated vertical columns with a width on the order of 50-100 nm. The films thicknesses ranged from 500-3000 nm. Scanning electron microscopy (SEM) was utilized to qualify the pitch values necessary for column formation and to view the sculptured thin films.

After deposition, samples were annealed at various temperatures, times and gas conditions to study the effects of the heat treatments on the film properties. For this chapter, two options were used for annealing. The first option is a 2" diameter Protherm open tube furnace. Anneals in this furnace were done at temperatures up to 1200 °C. The second option was a 2" diameter Thermcraft controlled atmosphere tube furnace. The available gases were nitrogen, oxygen, argon, and 5% H₂/N forming gas. For these experiments, the annealing times ranged from 5 minutes to 20 hours.

The XRD analysis was performed using a Bruker AXS X-ray diffractometer. The CuK α filament power settings are 30 kV and 20 mA. The Bruker AXS has a general area detector diffraction system (GADDS) that can scan 35 degrees of the 2θ range at one time for a given centered value, ω . For all of the data presented here, scans were taken for each sample at $\omega = 30^\circ$ and $\omega = 55^\circ$. One key advantage of the area detector lies in the time savings for each scan. It can be used to quickly identify phases, structures, and materials in the films. Also, as the STF structures are porous, the reflections per time period are significantly smaller than for continuous films. The Bruker AXS can also record the reflections over a broad range of χ at the same time. Therefore, integrating over the range of χ can provide a greater amount of data for polycrystalline films for a given scan time. For the scans at $\omega = 30^\circ$, the results represent an integration over χ using values of (-111) to (-68.2), while for the scans at $\omega = 55^\circ$, the χ integration values are (-106.3) and (-73.6). These values were chosen to encompass a typical range of the responses, and were applied consistently to all of the scan data. Peak location was determined either by direct evaluation of the data or by using the

cursor location function in the graphing package. Peak identification is determined by comparing the experimental peaks with the JCPDS database of XRD powder diffraction files.

The full design matrix utilized 3 substrates, 4 process conditions, 2 annealing conditions (along with the as-deposited films), and the pillar STF formation. Additional variations were added to illustrate or further define the results. The process conditions were based on the results in Chapter 3. The $\text{TiO}_x(\text{A})$ condition had a gas flow rate 39.9 sccm of oxygen and 1.0 sccm of argon. These conditions were shown to produce structures with mostly anatase formations after low temperature annealing. The $\text{TiO}_x(\text{Ru})$ condition had a flow rate of 19.9 sccm of oxygen and 4.0 sccm of argon. These pillars have more oxygen vacancies, which leads to a greater percentage of rutile formation for any given annealing condition. All of the TiO_x STF depositions were done with the substrate holder in the incidence angle, $\alpha = 80^\circ$ nominal position. Additionally, Ti films were deposited with no introduction of gas at base pressures in the $2\text{-}3 \times 10^{-7}$ Torr range. The final primary process condition moved the substrate holder to $\alpha = 76^\circ$ for Ti depositions. The less oblique angle creates pillars that are slightly shorter and wider, in addition to changing the value of the directed momentum (surface diffusion length). Table 4-1 lists the 4 primary process conditions with the respective identifiers used in the later figures.

Table 4-1 Primary Process Conditions for Annealing Experiment Depositions

Identifier	Flux Angle (α)	Gas Flow	Deposition Rate ($\text{\AA}/\text{sec}$)	Rotation (sec/rev)	Pitch ($\text{\AA}/\text{rev}$)
Ti	80°	None	25	12	300
Ti(76)	76°	None	25	12	300
TiO _x (A)	80°	39.9 sccm O ₂ 1.0 sccm Ar	25	24	600
TiO _x (Ru)	80°	19.9 sccm O ₂ 4.0 sccm Ar	25	24	600

The primary substrates were 3” n-type Si(100) single side polished wafers, 2”x3” standard float glass microscope slides (referred to as FG in the figures), and either 2” or 3” Si (100) wafers with 100 nm of thermal oxide grown by the supplier (referred to as SiO₂ in the figures). The standard annealing conditions were 450 °C, and 900 °C in air. The 450 °C range in general creates anatase films, while the 900 °C range is above the average reported range for rutile formation. For all controlled atmosphere anneals and most of the air anneals, the sample was loaded with the furnace at a temperature of ~150 °C. The ramp rate for both furnaces was set at 15 °C/minute. Also, for some anneals with the open air furnace, the wafer boats were inserted directly into a hot furnace (approximately 20 seconds to insert) to simulate a rapid thermal annealing. These samples are identified as an insertion anneal throughout the chapter. The annealing conditions were varied most frequently in temperature, time, ramp/insertion and background gases for the experiments. The float glass substrates were not annealed over 600 °C due to their lower melting point. In addition, one Al₂O₃ c-cut wafer received a deposition of the $\alpha = 80^\circ$ Ti film. Finally, a Ti film was deposited on a thermal oxide wafer with $\alpha = 82^\circ$.

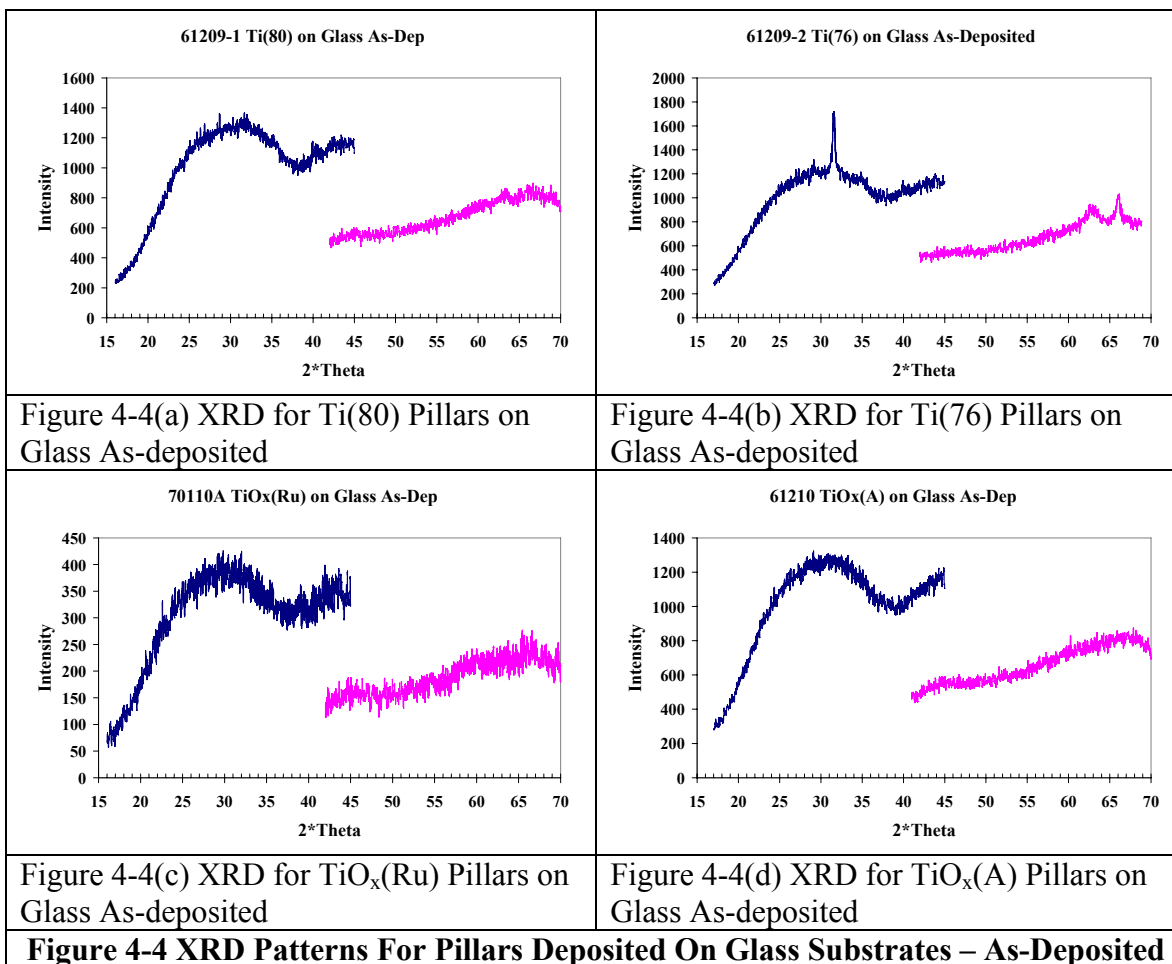
The typical structures were the pillar formations with nominal heights between 500-800 nm for all of the primary conditions. These formations have distinct spacing and in general are not in contact with their neighbors at these heights. Therefore, they best represent the small-scale independent systems as discussed in the background. Finally, all of the primary substrates received depositions of TiO_x(A), TiO_x(Ru), and Ti of ~750 nm thickness at normal incidence ($\alpha = 0^\circ$).

4.3 Annealing Experiments Results and Discussion

Several patterns emerge very quickly from the data that support expected trends, and can be summarized without extensive presentation. First, as α increases (becomes more oblique) the process should produce thinner, taller pillars for the same deposition rate and rotation speed. This result is easily predicted because the solid angle of the substrate becomes smaller with increasing α , which results in less material striking the substrate per revolution. Therefore, the porosity of the films at a given thickness is greater leading to thinner pillars. All Ti films deposited at $\alpha = 76^\circ$ were darker visually than those deposited with $\alpha = 80^\circ$. The visual response was more apparent with depositions on glass substrates as the $\alpha = 76^\circ$ films are significantly more opaque. Also, as was seen in Chapter 3, the reactive depositions to produce TiO_x structures were mostly amorphous as deposited for the STF depositions. This condition applied to both the anatase and rutile recipes, and is consistent with the literature for TiO_x films deposited at lower temperatures. These results were consistent across all substrates for the STF depositions.

Another obvious trend involved STF depositions on the float glass substrates. The films as deposited all had a large, wide curve across the XRD pattern with little or no distinct peak formation. The width of a peak indicates the degree of crystallization and the grain size. A sharp narrow peak indicates large grains and highly textured films, while wide shallow peaks indicate very small (almost amorphous) grain size and very weak texture. Figure 4-4 (a-d), shows the sculptured films depositions on float glass (microscope slide) for Ti when $\alpha = 80^\circ$ (Ti), Ti when $\alpha = 76^\circ$ (Ti76), $\text{TiO}_x(\text{A})$, and $\text{TiO}_x(\text{Ru})$ respectively. The only exception to this trend is the slight peak for Ti(76) near 31.5° . But this peak value is prevalent in all Ti(76) depositions regardless of substrate. These glass substrates were standard microscope slides, not highly polished like the semiconductor wafers. The increased surface roughness and amorphous surface most likely is the cause of the wide pattern as it would decrease the directed surface diffusion and thus the shadowing effects. Also, even after annealing, the XRD peaks evident are small and not well-defined in comparison to the large curve. Moreover, there are no new peaks present after annealing that are not expected in comparison to the other substrates.

The concept of the small scale system independence begins to be illustrated when comparing the pillar formations with the solid films deposited at $\alpha = 0^\circ$ (normal incidence). First, the XRD pattern intensities for the solid films are at least one order of magnitude larger than those for the most crystalline pillar formations although the height dimensions are equivalent. However, this factor is expected due to the density of the solid films and as XRD is primarily useful for bulk measurements. Another area where the comparisons are evident is the response to the annealing conditions as a factor of time.

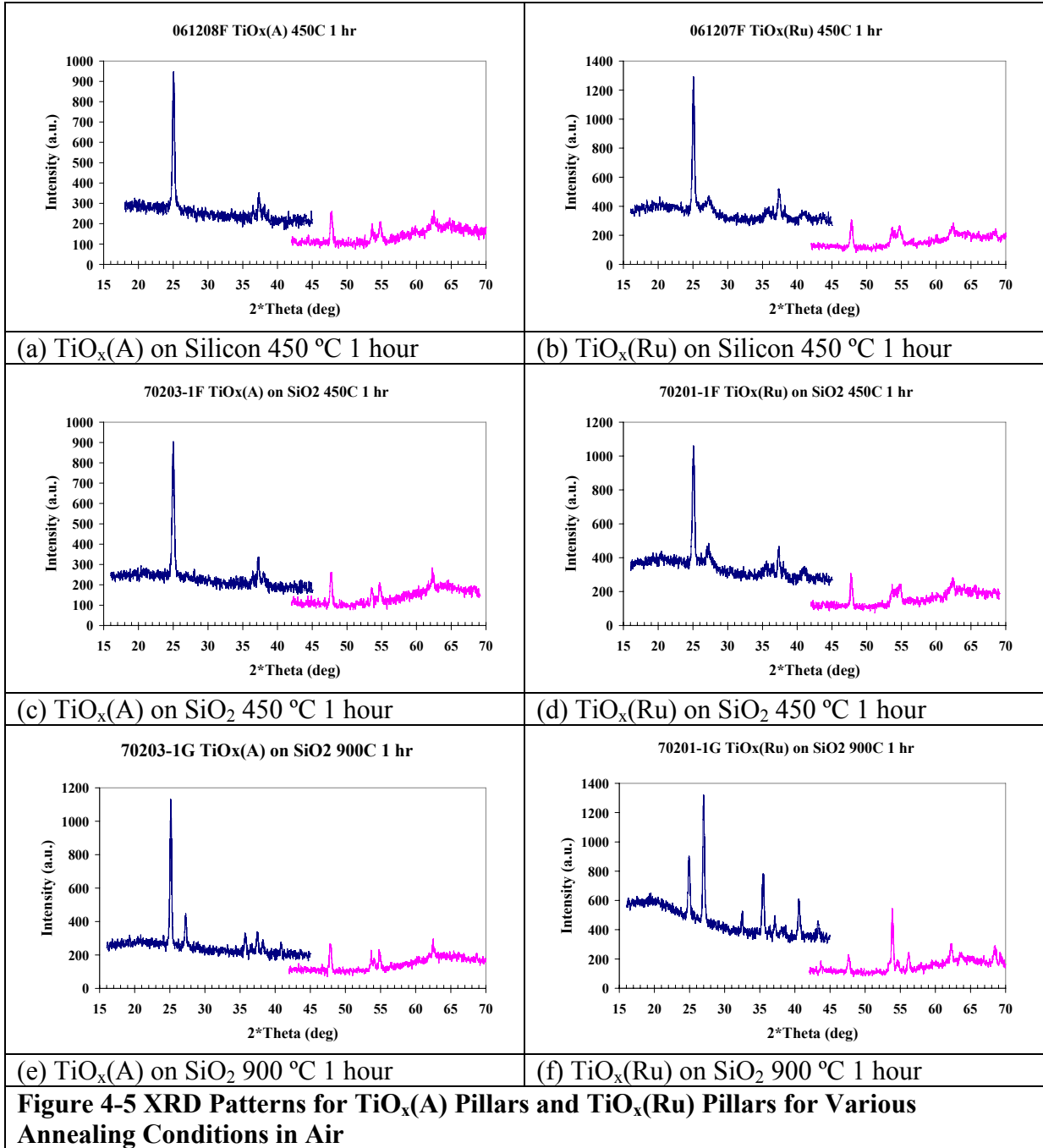


The pillar formations respond very quickly to the anneals. In fact, there is little evident difference between the crystal patterns for anneal times of 5 minutes, 20 minutes, or 60 minutes for temperatures above 450 °C with the pillars. However, the solid films (especially the Ti deposition) showed little change in the XRD pattern for even the longest anneals. The solid films did exhibit surface effects visually. The Ti films turned from silver to gold/brown at 450 °C, bluish at 600 °C, and silver again at 900 °C. However, on the glass substrates it was obvious the bottom surface of the Ti films were not affected as they remained silver in

color as observed through the glass. Also, there was little difference in the Ti XRD pattern for normal incidence films on any substrate. All of the films deposited at normal incidence had a dominant peak near 38.4° - Ti (002), with smaller peaks at 35.1° - Ti (100) and 40.2° - Ti (101) regardless of the substrate. The thicknesses of the normal incidence films are probably greater than the critical thickness for epitaxial matching (or substrate induced texturing). It may be necessary to use much thinner normal incidence films to get a solid comparison of annealing comparisons between normal incidence films and the STF samples.

The TiO_x pillar experiments produced results consistent with those factors discovered during the process development discussed in Chapter 3. The goal was to control the percentage of anatase/rutile in the pillars in order to produce sensor material with high percentages of either rutile or anatase. The TiO_x(A) recipe was shown in Chapter 3 to consistently produce films with higher anatase percentages than the TiO_x(Ru) recipe for any annealing condition in air for films on Si(100) substrates. Similar results were found using other substrates. Figure 4-5 shows the XRD patterns for the TiO_x(A) process on the left side boxes and the corresponding XRD patterns for the TiO_x(Ru) process on the right side boxes for selected anneals in air. The first row is for Si(100) wafers-450 °C, 1 hour anneals, the second row is for SiO₂ wafers-450 °C, 1 hour anneals, and the last row is for SiO₂ wafers-900 °C, 1 hour anneals. The peaks of primary interest for Anatase are near 25.2° [101], 37.8° [004], and 48.0° [200]. Similarly, the interesting Rutile peaks are at 27.4° [110], 36.1 [101], and 54.3 [211]. The TiO_x(A) films have no evidence of the 27.4° rutile peak after the 450 °C anneal, and only a slight indication of rutile formation after the 900 °C anneal. However, the 27.4° peak is evident for the TiO_x(Ru) for all annealing conditions. For the TiO_x(Ru) 900 °C anneal, the intensity of the

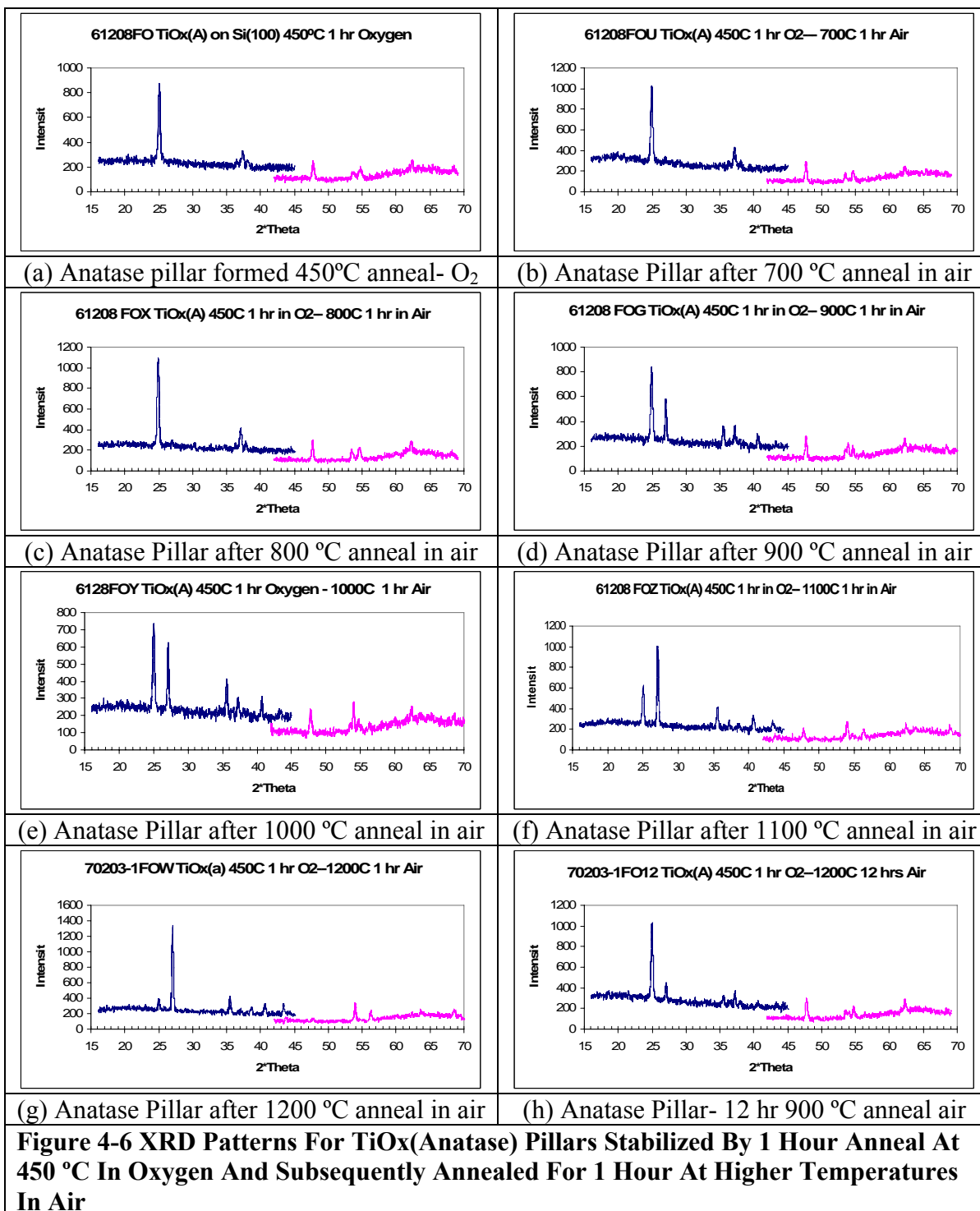
27.4° rutile peak is greater than the anatase 25.3° peak. Similar comparisons can be made for all of the anatase and rutile peaks, but the relative intensities of the 25.3° anatase peak and the 27.4° rutile peak provides the best qualitative measure of the anatase/rutile percentages for the TiO_x pillars to first order. Another key factor is the absence of any effect of the substrate on the crystal texture for both of the TiO_x processes. The XRD patterns after 450 °C anneals are nearly identical for TiO_x(A) regardless of the substrate as seen in panels (a) silicon wafer and (c) SiO₂ wafer. The same comparison can be made for panels (b) and (d). Also, note that for the 900 °C anneals, the preferred (highest intensity) rutile texture using either TiO_x recipes is Ru(110) at 27.4°.

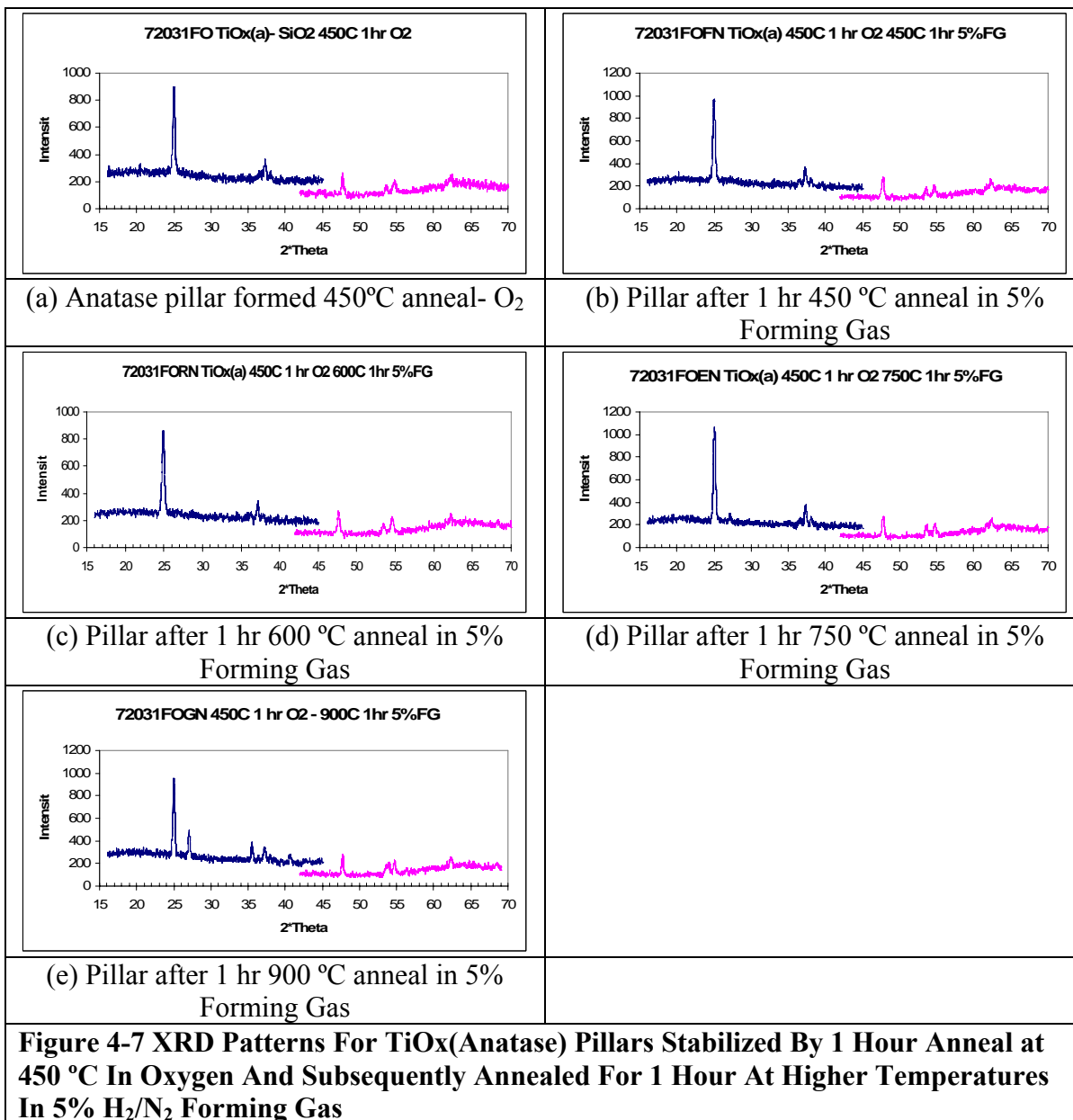


The anatase-rutile (A/R) transformation limits the operation of anatase based sensors to temperatures below the typical transformation temperature range (~ 800 °C). Attempts to stabilize anatase films with respect to this transformation have usually focused on the effect of dopant additions to the anatase films.[76, 82, 88, 125-127] The stability of the anatase pillar formations with respect to temperature was studied via an annealing experiment. Pillars were formed using the $\text{TiO}_x(\text{Anatase})$ process recipe for $\alpha = 80^\circ$ STF depositions on both Si(100) and the SiO_2 wafers. The pillars were annealed at 450 °C in oxygen for one hour to form a stable anatase formation. These anatase formations were then annealed at various temperatures (700 °C-1200 °C) for one hour in air. One sample was annealed for 12 hours at 900 °C in air. For the 1200 °C anneals and the 12 hour anneals, the SiO_2 substrate was used to minimize the oxidation effect on the substrate surface. The XRD results are presented in Figure 4-6(a-h). Panel (a) shows the initial XRD pattern for an anatase pillar formation prior to any subsequent high temperature treatments. The strong anatase (110) peak at 25.3° is clearly evident. Panels (b-g) represent anneals at 700 °C, 800 °C, 900 °C, 1000 °C, 1100 °C and 1200 °C respectively. The first indications of rutile formation do not occur until the appearance of small peaks of rutile (110) at 27.4° and rutile (101) at 36.1° after the 900 °C anneals. Using the anatase (110) peak and the rutile (110) peaks as a relative measure, the films do not turn predominately rutile until the 1100 °C anneals. Some evidence of anatase formation is still present even after the 1200 °C anneal. Panel (h) shows the results after a 12 hour anneal at 900 °C, which is still mostly an anatase formation. These temperatures are at the upper end of any range previously reported for the anatase to rutile transformation. From the discussion in earlier chapters, the presence of oxygen vacancies can trigger the onset of the A/R transformation at lower temperatures. Also, the initial formation of a rutile grain

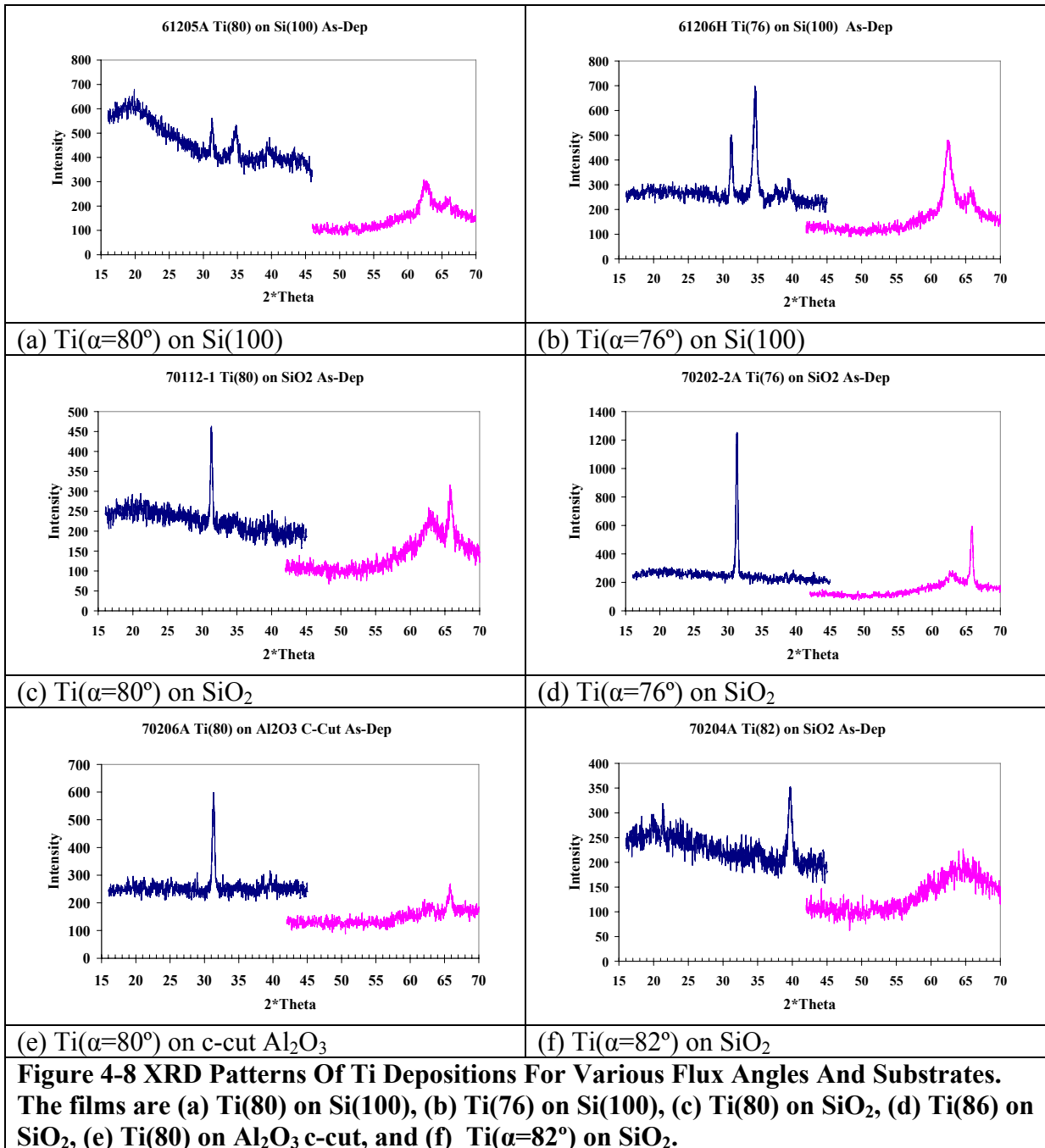
enhances the transformation of the surrounding material. But the STF pillar formations exhibit small-scale independence, so an area of the film where a substantial number of oxygen vacancies triggers the transformation would not propagate across the entire film. Finally, grain coalescence is another critical factor in the A/R transformation. Unless the pillars come into contact with a neighbor (or with the material in the “scrub layer”), each individual pillar is the sole source for TiO₂ material, *i.e.* an independent system.

The anatase sensors must also demonstrate the ability to operate in a reducing environment without significant loss of oxide from the bulk triggering the A/R transformation. For this experiment, anatase pillars formed on a SiO₂ surface (using the same process as for the high temperature studies in air) were subjected to 1 hour anneals in a reducing environment. Anneals were performed in a controlled atmosphere furnace with 20 scfh of 5% H₂ in nitrogen, commonly referred to as 5% forming gas. The XRD results are shown in Figure 4-7 (a-e). Panel (a) is the control anatase sample without any forming gas annealing. The forming gas anneals were done at (b) 450 °C, (c) 600 °C, (d) 750 °C, and (e) 900 °C for 1 hour. The first indication of significant rutile formation does not occur until the 900 °C anneals. These results indicate the STF sensors are capable of operating at much higher temperatures than are typical with anatase structures.





As discussed during the background section, several groups have reported on an effect of the flux incidence angle, α , and the pillar formation on the crystal structure and degree of crystal texturing.[104, 107] As the TiO_x films are mostly amorphous as-deposited and did not show any substrate dependence on the preferred orientation, the Ti depositions were used to investigate this phenomenon. The as-deposited XRD patterns for Ti films deposited at different flux angles, $\text{Ti}(\alpha=76^\circ)$, $\text{Ti}(\alpha=80^\circ)$, and one at $\text{Ti}(\alpha=82^\circ)$, and on different substrates are presented in Figure 4-8. The films are (a) $\text{Ti}(80)$ on $\text{Si}(100)$, (b) $\text{Ti}(76)$ on $\text{Si}(100)$, (c) $\text{Ti}(80)$ on SiO_2 , (d) $\text{Ti}(76)$ on SiO_2 , (e) $\text{Ti}(80)$ on Al_2O_3 c-cut, and (f) $\text{Ti}(\alpha=82^\circ)$ on $\text{Si}(100)$. There are several obvious features in these XRD patterns. First, the XRD patterns change significantly not only as a function of the substrate, but also directly as a function of the growth angle. The left side panels, (a-Si, c- SiO_2 , e- Al_2O_3) all represent Ti films deposited with $\alpha = 80^\circ$. While the SiO_2 -(c) and Al_2O_3 -(e) patterns are similar, the Si-(a) panel has a peak near 35° which is not as well defined for the other two substrates. This peak probably indicates $\text{Ti}(100)$ formation. Also, the (c) and (e) panels have a more defined peak at 65.7° than the Si-(a) panel. For the depositions at $\alpha=76^\circ$, the differences between the Si-(b) panel and the SiO_2 -(d) panel are the same as for the $\alpha=80^\circ$ panels. Therefore, there exists some substrate dependence on the XRD pattern.



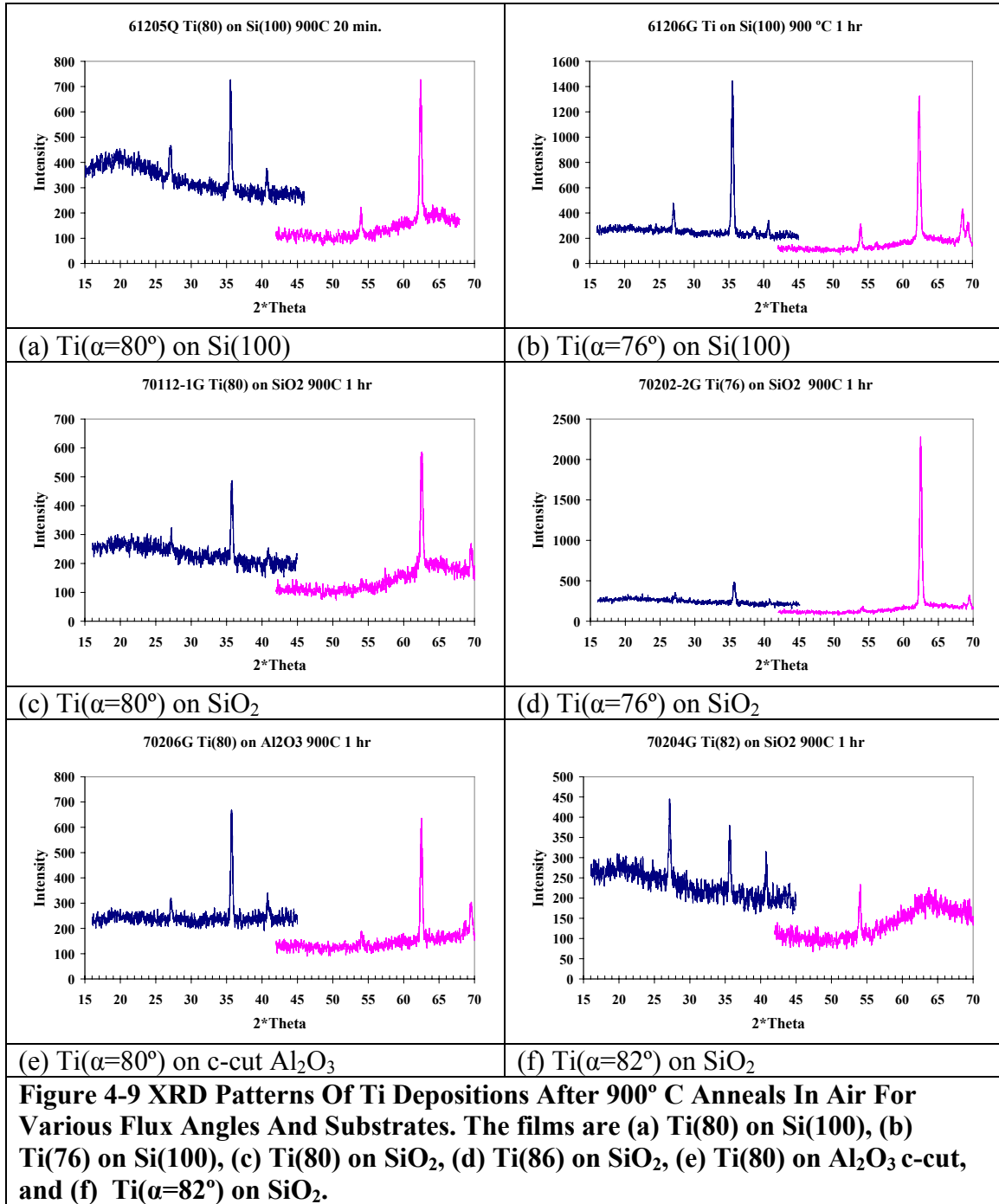
The results also indicate a change in the XRD patterns as a function of the flux angle of incidence, α . The effect is most clearly seen in the depositions on silicon where the XRD patterns for $\alpha = 76^\circ$, 80° , and 82° are represented by panels (b), (a), and (f) respectively in

Figure 4-8. The Ti(002) peak at 38.4° which dominates the normal incidence depositions here and in the literature for silicon substrates is barely evident in any of the patterns. The clear indication of the Ti(101) peak at 40.2° is only seen for the most oblique deposition at $\alpha = 82^\circ$. The most intense peak for the $\alpha = 76^\circ$ deposition is Ti(100) at 35° . As the angle becomes more oblique, this Ti(100) becomes both less intense and wider. At $\alpha = 82^\circ$, this peak is very small. Finally, the peak at 31.5° which is evident for all substrates at $\alpha = 76^\circ$ and $\alpha = 80^\circ$ is not evident when $\alpha = 82^\circ$, nor for the normal incidence depositions.

The peak near 31.5° is the dominant XRD peak for all of the $\alpha = 80^\circ$ titanium depositions and exists in all of the $\alpha = 76^\circ$ XRD patterns. However, this peak has proven difficult to identify. The smallest 2θ angle listed for α -Ti (the close-packed-hexagonal phase) in the JCPDS files is the Ti(100) peak at 35.09° . Oxygen incorporation in the titanium lattice can shift the 2θ peak value to lower values due to expansion of the lattice, but the amount of the shift is less than one degree.[109] None of the TiO_2 phases have an XRD peak near this location, nor do any of the TiO_x sub-oxides for $x > 1$. The TiO diffraction files list TiO(200) at 32° , but it is highly unlikely that a stable crystalline phase of this material has been formed, especially as the samples have been exposed to air for significant lengths of time. The reported 2θ values for titanium nitride and TiS_2 are all over 36° . Moreover, since the peak also is present for STF depositions on the sapphire and glass substrates, it cannot be a member of the titanium silicide family. This anomaly requires further investigation.

The most interesting result from the annealing studies concerns the high temperature anneals of the Ti pillars. The corresponding XRD patterns for the same films as in Figure 4-8 after a

900 °C anneal in air are shown in Figure 4-9. As with the as-deposited Ti films, the XRD pattern is changing not only with substrate type, but more significantly with the deposition

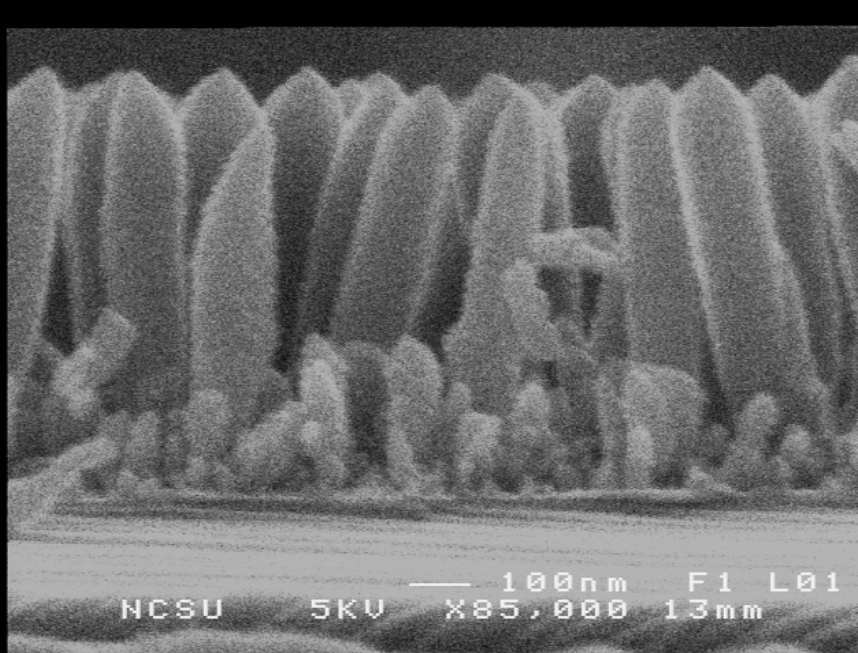


angle. The rutile (111) peak at 41.2° and the rutile (211) peak at 54.3° are both more prevalent on the Si(100) substrates (a, b) than on the SiO_2 substrates(c, d). The XRD patterns are markedly different as α is increased to 82° (f) versus the less oblique angles (a, b). Instead of the dominant rutile (110) peak at 27.4° that was apparent in all of the TiO_x pillar 900°C anneals, the rutile (101) peak at 36.1° is larger than the (110) peak for most of the annealed Ti pillar samples. But the largest peak is near 62.5° for every sample but the Ti(82) on silicon. Moon identifies this peak as rutile (002), a primary peak formed by Ti oxidation on m-cut sapphire, in his investigation of the orientation response of rutile TiO_2 gas sensors.[10] However, there are many Ti(X) compounds with XRD peaks in the $62\text{-}63^\circ$ range, so more investigation is warranted.

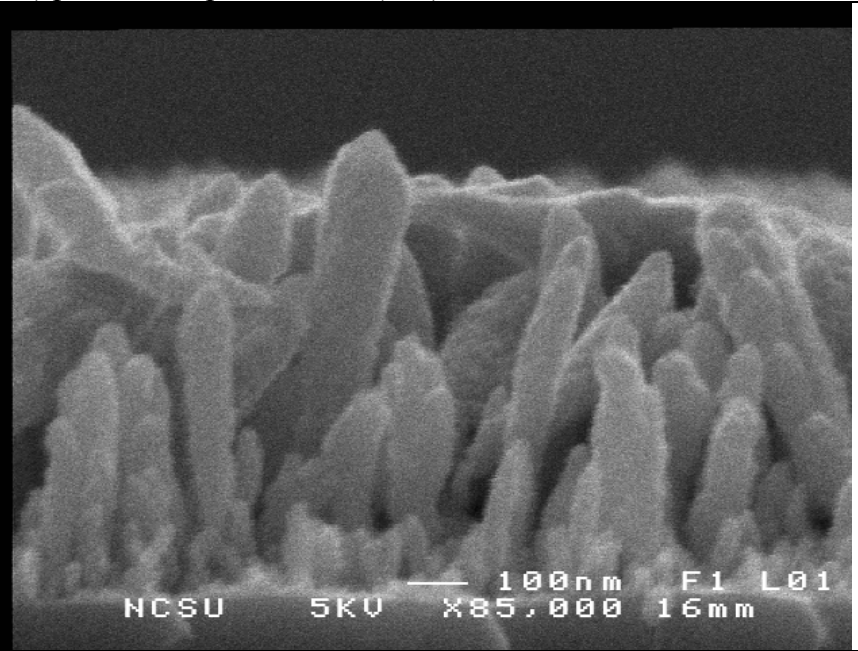
The SEM images of these annealed films are quite revealing. The images in Figure 4-10 show the Ti(80) and Ti(76) pillars on silicon as deposited. Note the Ti(76) pillars are slightly thicker and shorter. Also, the features in the scrub layer growth and the pillar peaks are sharply defined. The 900°C anneals were done with either a low temperature ($<150^\circ\text{C}$) load and $15^\circ\text{C}/\text{min}$ ramp or a 20 second direct insertion into a hot furnace. Figure 4-11 shows the Ti(80) pillars formation after (a) a 900°C , 20 minute insertion, (b) a 900°C ramp anneal, and finally, (c) the Ti(76) pillars formation after the 900°C ramp anneal. Although the melting point of Ti is normally around 1600°C , it appears that the pillar formations have melted prior to oxidation for the Ti(80) formations at 900°C . The insertion anneal in particular demonstrates both a complete melting of the pillar formation, but also signs of recrystallization. The Ti(80) ramp anneal has evidence of a melt/recrystallization starting at

the top of the pillar and moving toward the surface. Finally, the thicker Ti(76) pillars have not completely lost their shape, but the scrub growth around them has rounded features as do the peak tops.

Although the melting theory is initially counter to traditional thinking, remember the particle size of these features is quite small. A pre-melt zone exists along the surface of a bulk metal several nanometers in thickness which serves to transfer heat to the bulk via convection before actual melting occurs.[75] This pre-melt thickness is on the same scale as the total thickness of the titanium STF pillars, so surface effects will play a more significant role in the material properties.

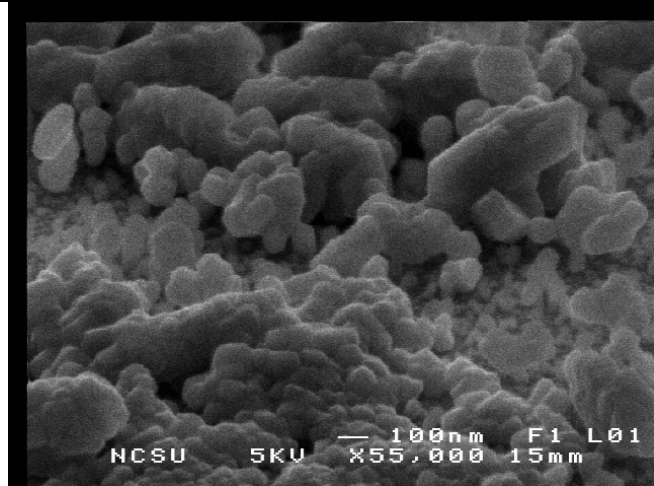


(a) $\text{Ti}(\alpha = 80^\circ)$ pillars as deposited on Si(100)

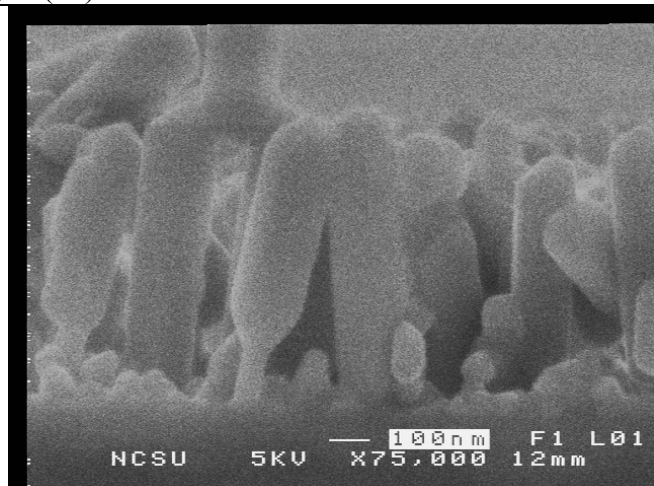


(b) $\text{Ti}(\alpha=76^\circ)$ pillars on Si(100) As Deposited

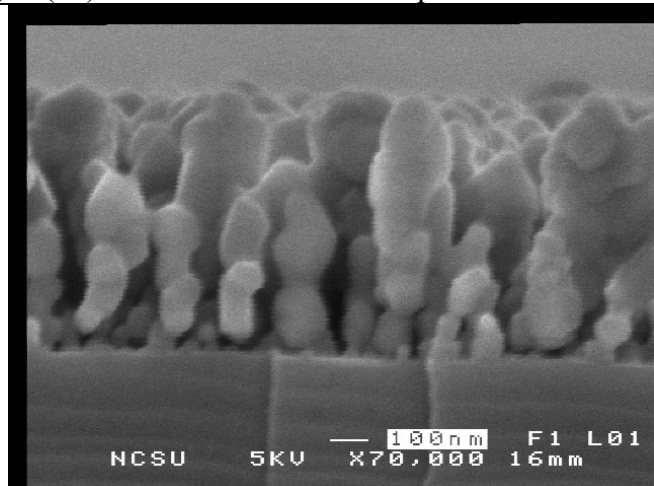
Figure 4-10 SEM Images of Ti Pillars Deposited at Various Flux Angles on Si(100)



(a) Ti(80) Pillar after 900° C Insertion anneal



(b) Ti(80) Pillars after 900° C Ramp Anneal



(c) Ti(76) Pillars after 900° C ramp anneal

Figure 4-11 SEM of Ti Pillars After 900°C Annealing

4.4 Annealing Conclusions and Future Work

The annealing studies on sculptured thin films served to illustrate the small scale “independence” associated with these structures. This ability for each structure to react independently to external forces, in this case high temperature annealing, allows for these films to react quite differently than conventional thin films. Some of the effects are straightforward in concept and results, while others were unexpected and difficult to qualify.

An example of a basic effect of the small-scale independence is the rapid oxidation and crystallization of the STF films with respect to their normal incidence (solid) counterparts. The highly porous pillar structure drastically reduces the diffusion pathways for oxygen throughout the film. As a consequence, the Ti STF films oxidized more quickly and thoroughly than the solid films which had only incidental surface oxidation for the same annealing time. Also, with the TiO_x pillar formations, the crystallization of the films was strongly evident even with annealing times of 5 minutes.

The TiO_x (Anatase) films produced clear anatase XRD patterns after 450 °C annealing in oxygen or air. Once the anatase pillars are formed, they show a high degree of temperature stability upon subsequent heat treatments with respect to the anatase-rutile transformation. The onset of the rutile transformation does not occur to a significant degree below 900 °C in air, with measurable amounts of anatase still present even after one hour at 1200 °C. These values are among the highest temperatures reported for this transformation. Similar results were found for annealing in a reducing environment. The independence of the structures

contributes to this stability. The known triggers for rutile formation at lower temperatures are significant oxygen vacancies in the oxide or an initial amount of the rutile phase in the films. The reduction in the oxygen diffusion pathways likely leads to a more complete initial oxidation, limiting the number of vacancies. The presence of the rutile phase can initiate a transformation throughout a continuous film, but isolated columns are not affected by a transformation in a neighboring pillar unless the pillars are initially in contact or become so during the process. This transformation resistance has potential applications in extending the temperature operation range of anatase based sensors.

The pillars deposited with reactive deposition (TiO_x films) did not display any significant crystallinity when deposited at glancing angles. However, the titanium pillars deposited at pressures below 10^{-6} Torr did exhibit a relationship between the flux angle of incidence and the preferred crystal orientation. The differences in orientation were most pronounced between the films deposited at normal incidence and those deposited at glancing angles. Yet the relationship was readily apparent across the limited range (76° - 82°) available with the NCSU e-beam system for glancing angles. In fact, the depositions at $\alpha = 76^\circ$ produced films with an anomalous XRD peak at a 2θ value near 31.5° for all of the substrates involved in the study. This peak is not easily identifiable from the standard powder diffraction patterns for the Ti, Ti-O, Ti-N, or Ti-Si material systems. Additional materials characterization using TEM, Raman spectroscopy, or EDS would be beneficial to identify the materials or phase present in these pillars.

The change in preferred orientation also was apparent with the subsequent oxidation of the Ti pillars, as different Ti starting orientations produced rutile phase titania with different preferred orientations. The differences were slight across the glancing angle range, yet there exists substantial variations between the rutile orientation XRD patterns produced by the oxidation of glancing angle Ti pillars, by the oxidation of normal incidence Ti films, and by the oxidation/crystallization of the TiO_x pillars.

Finally, the SEM images of the Ti pillars after high temperature (900 °C) annealing in air illustrated the titanium oxidation process from the unique perspective of having most of the surface of the structure exposed to oxygen and thus a very short diffusion path through any oxide film. The shapes of the thicker pillars ($\alpha = 76^\circ$) become distended and rounded. The thinner pillars ($\alpha = 80^\circ$) appear visually to have melted for the rapid (insertion) heating process, while the same pillars maintain greater shape integrity when the annealing process is ramped more slowly to the final temperature. The additional oxidation which occurs during the ramp may stabilize the pillar formation. The remaining features show some sign of oxidation and regrowth for both ramp rates. However, the data is too limited to state without qualification a reduced melting point process has occurred, especially as the XRD patterns do confirm the presence of rutile TiO_2 .

Chapter 5

Sensor Formation Using Sculptured Thin Films

This chapter investigates the use of nano-scale metal oxide semiconductor (MOS) films for gas sensors with particular attention focused on the titania system. For most thin film MOS sensors, the sensing mechanism is based on the interaction of the surrounding atmosphere with the sensor surface. Therefore, increasing the available surface area should increase the sensitivity of the sensor. The basic premise of this dissertation lies in using the GLancing Angle Deposition (GLAD) techniques to increase and control the surface area of metal oxide films and thereby increase the sensitivity of sensors based on these films.

The first section of the chapter reviews the types of sensors which utilize the TiO₂ material systems. Also, the designs for sensors fabricated using GLAD techniques reported in literature are discussed with respect to their various attributes. The second section covers the design of sensor structures fabricated for this research. In addition, the characterization of the sensors required the design and fabrication of a suitable test chamber. The chapter concludes the results of the initial sensor tests, an analysis of the factors affecting the results, and proposals for further characterization.

5.1 Titania Gas Sensors

The details of gas sensors based on semi conducting metal oxide films was covered in depth in Chapter 1, but a quick review is provided here for continuity. Metal oxide films are commonly used in two types of sensors; 1) the MOS conduction sensor, or 2) humidity sensors. The MOS conduction sensor is based on the interaction of oxygen species at the surface of the film. The humidity sensors are generally either capacitance sensors (using mostly insulating metallic oxides) based on the dipole nature of water adsorbed by the films, or optical sensors (using transparent oxides) which rely on changes in the transmission characteristics of the films due to humidity.

For an n-type semiconducting oxide, the ionic adsorption of oxygen specie (either singly or doubly ionized) at the surface effectively reduces the carrier (electron) concentration in the sensor material. Therefore, the resistance of the material increases. The presence of a reducing gas in the ambient, i.e. CO or a hydrocarbon, reduces the amount of adsorbed oxygen species on the surface, which allows the electrons to return to the active carrier concentration (thus decreasing the resistance). TiO_2 is widely used as a material for MOS gas sensors for hydrogen[11, 125, 128-131], CO[126, 132], methanol[13, 77, 133], and ethanol[13, 134, 135]. A recent literature review ranked TiO_2 as the 4th most published MOS material.[6]

Most TiO_2 humidity sensors are capacitance-based and rely on the proton-conducting water layers adsorbed on the porous surface.[136, 137] Anatase has a higher water adsorption

capacity than rutile, and is generally preferred as a humidity sensor for that reason.[79] Due to the differences in the material properties of rutile and anatase, proper characterization of a new test structure requires solid control of the phase formation during fabrication.

5.2 Sculptured Thin Film as Gas Sensors

The use of sculptured thin films (STFs) as gas sensors has been widely discussed as a potential application, but publication has been mostly limited to a small number of papers concentrating on humidity sensors based on the capacitive response of insulating oxides. [67, 68, 138, 139] However, these investigations have utilized several innovative methods for the physical design of the sensor. Each of these designs could be used with different oxide materials (i.e. TiO_2) and potentially different measurement techniques than described in the papers. This section looks at the designs previously utilized and their results, advantages, and drawbacks.

The simplest of these STF sensor designs is also the most recently published.[139] Vertical pillars of aluminum oxide (2.5 μm in height) were deposited onto Cr-Au interdigitated electrode (IDE) structures that had been patterned onto borofloat substrates. Five sensors were made by varying the deposition angle of incidence, α , to values of 60° , 75° , 78° , 81° , and 85° . The substrate rotation was kept constant. As described in detail in Chapter 2, this deposition scheme produces films that are relatively dense (at $\alpha = 60^\circ$) to increasingly porous with a columnar (vertical post) nanostructure. The cross-sectional and planar view SEM

images of these films are shown in Figure 5-1.[139] The increasing porosity can be clearly seen between the films with $\alpha = 60^\circ$ (a, b); $\alpha = 78^\circ$ (c, d) and $\alpha = 85^\circ$ (e, f).

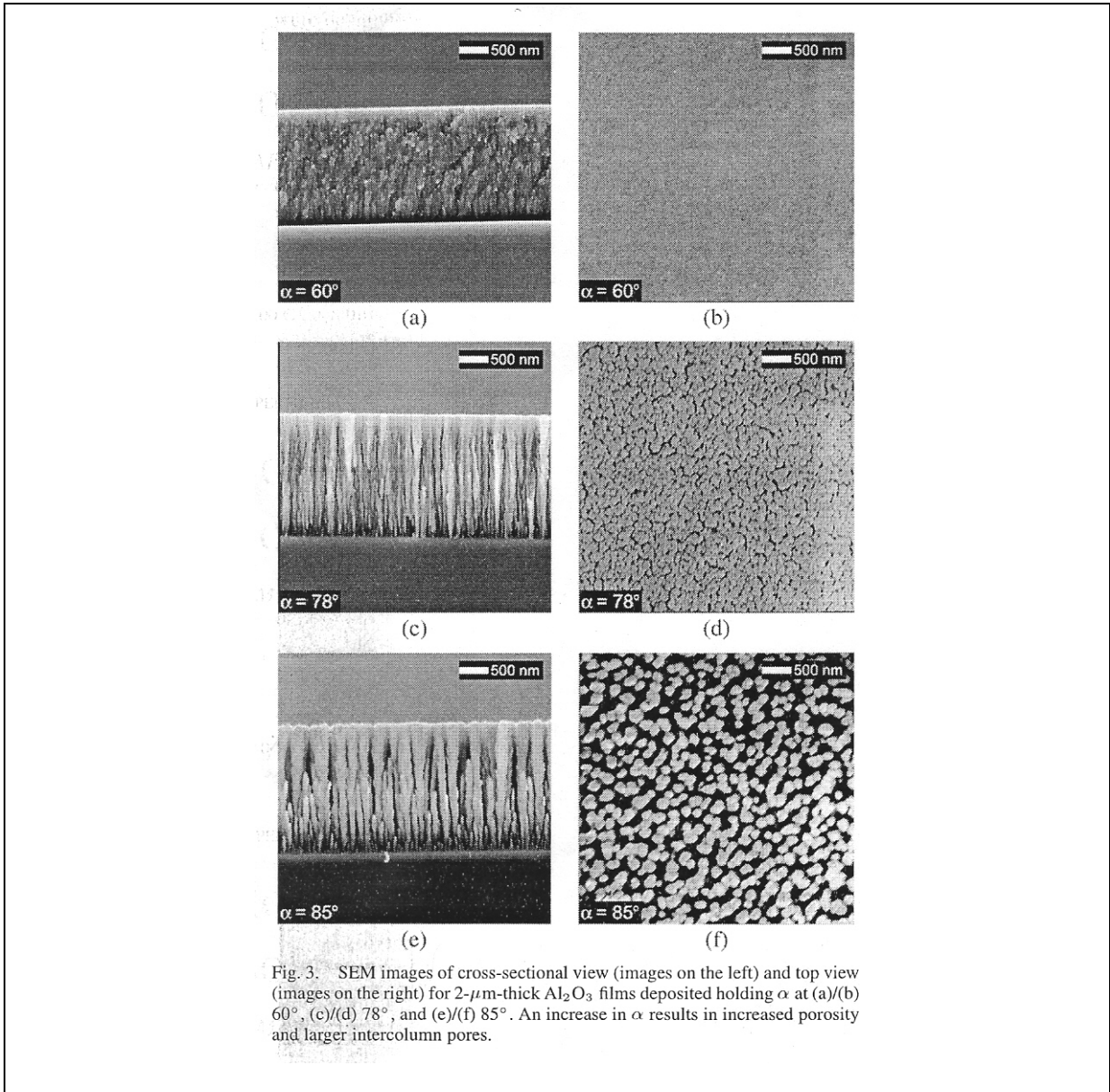


Fig. 3. SEM images of cross-sectional view (images on the left) and top view (images on the right) for 2- μ m-thick Al_2O_3 films deposited holding α at (a)/(b) 60° , (c)/(d) 78° , and (e)/(f) 85° . An increase in α results in increased porosity and larger intercolumn pores.

Figure 5-1 Open Vertical Post Capacitance Humidity Sensor Fabricated by Increasing the Angle of Incidence. Panels indicate values of α from 60° (a, b) to 78° (c, d) and to 85° (e, f) [139]

The capacitive responses of these films[139] to changes in relative humidity (RH) were consistent with previously work on the effect of pore size on the response of anodized alumina humidity sensors.[12] Increasing the pore size (in the STF case- the voids between the pillars) narrows the range where the sensors are responsive. Also, the range shifts to higher values of relative humidity. The most porous STF sensors ($\alpha = 85^\circ$) tested were not measurably sensitive for values below 80% RH, but the capacitance increased by a factor of 20 between 80% and 90% RH. The response and desorption times were extremely fast for these sensors with the fastest (most porous) desorption times averaging 40 ms.

The second type of STF capacitive humidity sensor uses the original STF deposition solely as a template.[138] The sensor material, in this case HPR504 photo resist, was formed around the nanostructures. Initially, a 1.4 μm thick film of SiO_2 helices were deposited ($\alpha = 85^\circ$) on a solid Cr electrode layer. Then the photo resist was spun onto the structures forming a solid composite by filling the voids between the SiO_2 helices. After exposing and curing the resist, the original helices were removed using a buffered oxide etch. Finally, a thin Ti layer was evaporated onto the remaining resist structure to provide a top electrode. Due to the helical nature of the original SiO_2 pillars, the internal voids were shielded from the evaporation process and a porous structure remains. This type of film structure has been described as Perforated Thin Films (PTFs) and has also been used to create porous catalytic electrodes using metals.[140] The humidity response of the PTF sensor was similar to the response of the open vertical post sensors discussed in the previous paragraphs in that the PTF sensor was very insensitive at low values ($< 60\%$) of relative humidity, but were very sensitive

across the higher humidity ranges. The typical response times of 175 ms were slower than the open post structure, but still very rapid.

The final capacitive sensor design presented was also the first one published was the original impetus for this dissertation topic. The design consists of porous STF structures situated between metal electrodes.[67, 68, 138] Similar vertical posts are deposited (SiO_2 , 2.3 μm tall, $\alpha = 85^\circ$) on a solid layer of electrode material (Al in this case). However, during the end of the deposition, α is changed *in-situ* towards a normal incidence to deposit a denser “capping” layer. A thin layer of electrode material (Al or Au) can then be deposited on this capping layer without making a direct short to the base electrode. By depositing a very thin ($\sim 30\text{nm}$) electrode layer that is electrically continuous, yet physically porous, one can allow for diffusivity of the sensor gas (or water vapor) through the top electrode. The results for this type of sensor have been excellent, with the change in capacitance of more than 4 orders of magnitude over the range of 15% to 85% relative humidity. The physical design and the capacitive response for a typical vertical post-capping layer sensor is shown in Figure 5-2.[67] The sensor response time for this configuration was reported as 3 sec, which is slower than the other two designs[67], but the response time was improved by minimizing the capping layer dimensions.[138]

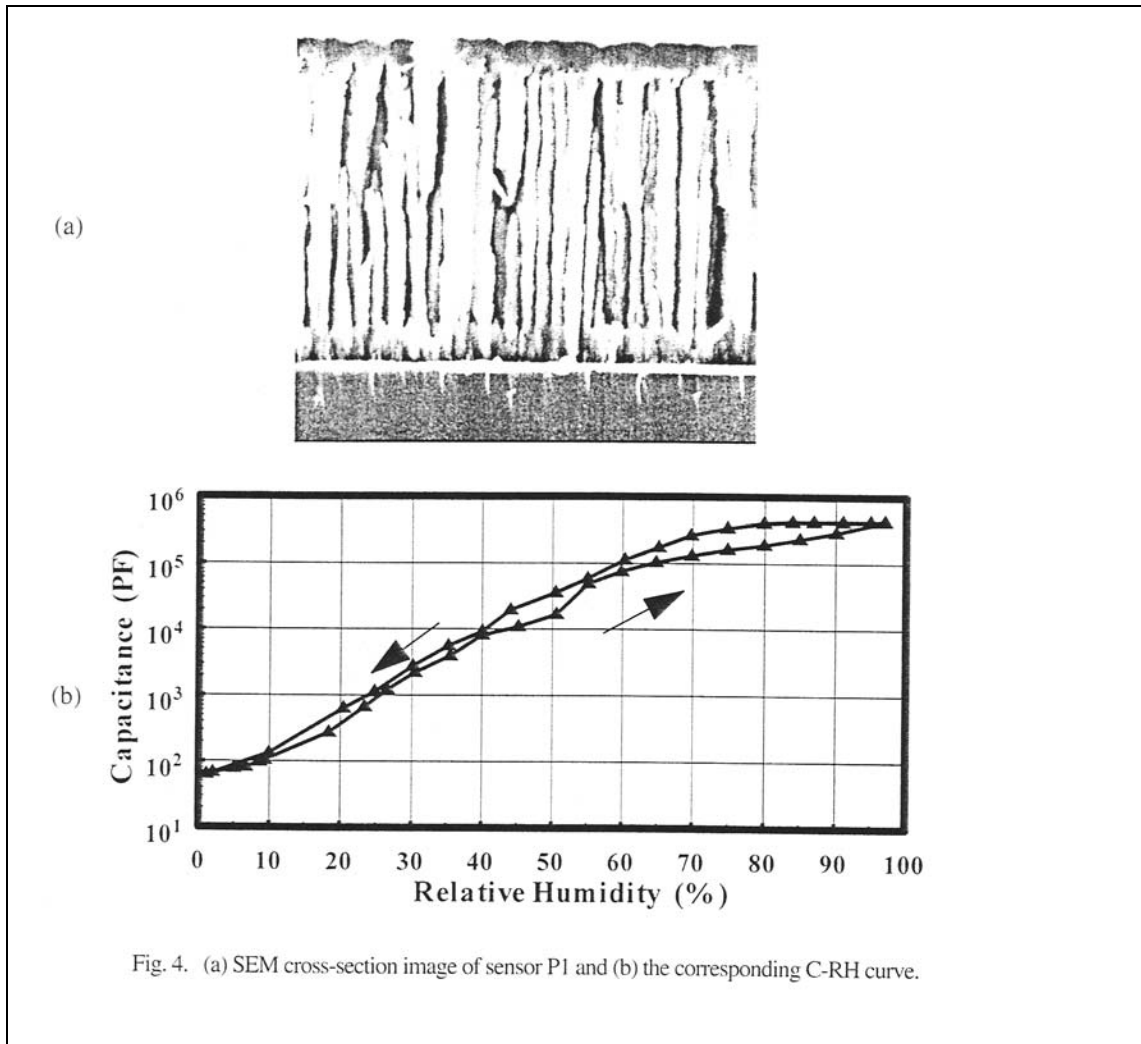


Figure 5-2 Vertical Post--Capping Layer Capacitance Humidity Sensor (a) SEM Image (b) Humidity Response[67]

These three STF humidity sensor designs represent the published STF test structures specifically used for gas sensing. Of the three designs, the simplest design is the open vertical post-IDE sensor. It did exhibit increased sensitivity vis-à-vis the increasing porosity (film surface area), and had the fastest response time. However, the range of sensitivity is directly related to the lateral pore size (in effect, the distance between the poles) since the electrode

path is horizontally orientated. The PTF sensor may be useful, and is similar in response to the open post sensor, but it is not directly based on the STF structures (or on metal oxides). Therefore, it was presented primarily as a discussion point. The vertical post-capping layer sensor demonstrated the most sensitive response for a capacitive humidity sensor. Also, the vertical positioning of the electrodes allows for the posts to be contacted axially. This type of contact formation would more easily allow direct conductance or spectroscopic impedance measurements. However, the fabrication and qualification of the capping layer is significantly more difficult than the other designs. The capping layer requires either very thick films (several microns) or the use of a goniometer stage and is not a viable design for this project.

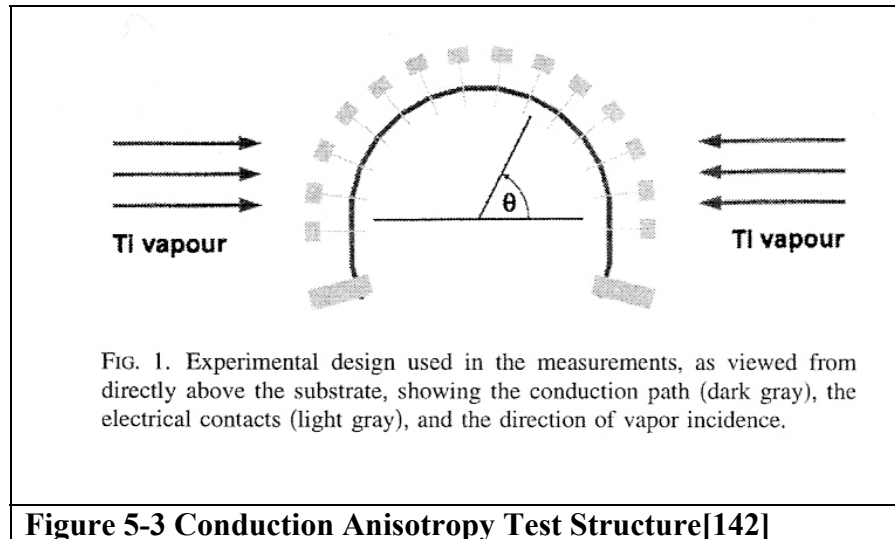
Capacitance measurements are not the only way of characterizing STF formations (or their interaction with the environment). Although the intent of their research was not towards gas sensor design, recent publications investigating the electrical properties of porous STFs describe novel test structures which could be modified into a MOS conductivity sensor.[141, 142] The first study measured the effect of the deposition angle and the number of chevron arms on the mechanical and electrical properties of Cr films.[141] The electrical characterization used simple four-point probe resistivity measurements. With this test structure, any conduction anisotropy which exists with respect to the primary chevron orientation averaged out. But even with chevron films, structural anisotropic elements exist in the growth plane parallel to the flux angle of incidence. These elements are related to the crystal texturing described in Chapter 4. Therefore, the second study concentrated on chevron

test structures designed to directly address and measure the effects of the structural anisotropy on the directional conductivity of the chevron films.[142]

An important facet of the open vertical post structure is that each post is essentially isolated physically from its neighbors, although some points of contact can occur as the posts become thicker. However, the chevron films not only extend toward each neighbor along the primary flux axis, but also broaden (flatten) as each leg lengthens. Physical contact between nearest neighbors is much more prevalent than in the post structures. This contact factor was obvious in the annealing studies which showed visible damage and contraction for annealed chevron films even at low temperatures (~ 500 °C), while the isolated vertical posts maintained structural integrity.[112] Therefore, significant conduction pathways can exist along the horizontal plane for the chevron type structure. The test structure used by Vick, *et al.* for the conduction anisotropy measurements had a top view as shown in Figure 5-3.[142]

The dark grey is the conduction path through the chevron films. This path was lithographically created by depositing the STFs in a trench patterned in a very shallow (130 nm) resist layer followed by a liftoff process. The Cr/Au metal contacts (light gray) are sputtered through proximity masks. A critical factor in this design is the use of a bimaterial chevron layer. The first 10 chevrons are SiO₂, and the second 10 chevrons are the Ti conducting layer. The bilayer formation serves to isolate the conducting layers in the large chevron formation from the initial “scrub” layer that exists in GLAD depositions. In the scrub layer, the shadowing effects are just beginning to affect the structure and the nearly

continuous layer may provide a conduction pathway. Also, the structural anisotropies in the chevron formation that were the focus of this effort are more significant with thicker films.



The conduction measurements showing the directional dependence of the resistivity in these chevron films are shown in Figure 5-4.[142] The more porous films (more oblique α) have a significantly higher degree of anisotropy, and correspondingly a significantly higher resistivity. Also, the authors concluded the native oxide formation on the titanium chevrons played an increasingly significant role as the porosity of the films increased. These results are not unexpected when the potential conduction pathways through the highly porous films are considered. But more importantly, these types of conductivity measurements could be adapted for MOS gas sensor measurements using chevron films instead of pillars to gain conduction paths parallel to the substrate.

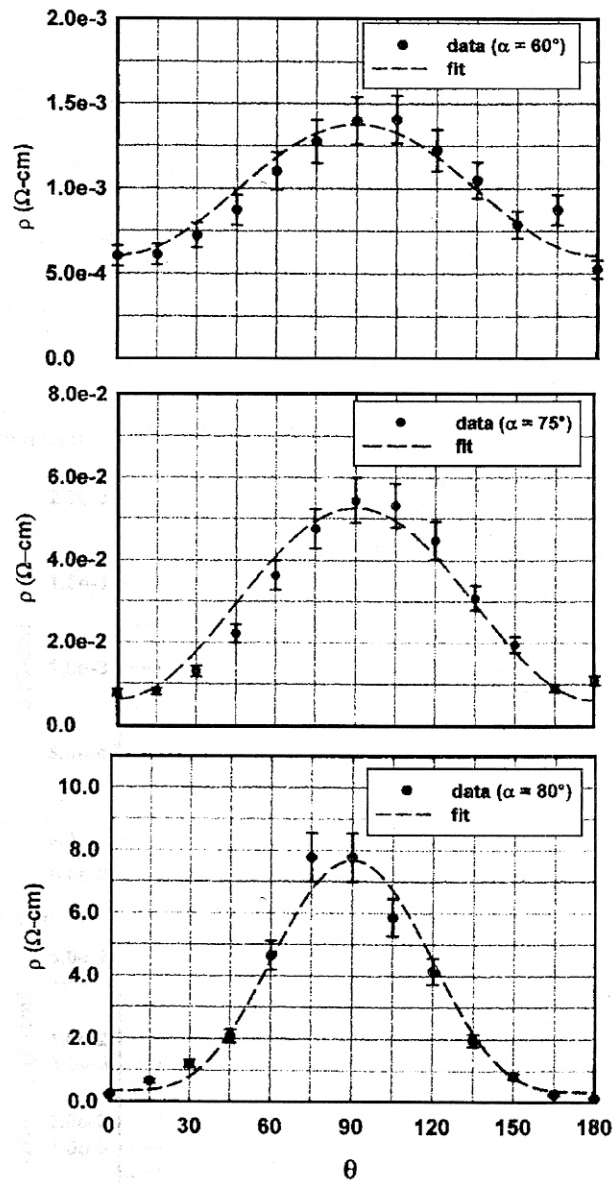


FIG. 2. Directional dependence of resistivity is shown for the samples deposited at $\alpha=60^\circ$, 75° , and 80° . The dashed curves represent polynomial fits in $\cos^2(\theta)$.

Figure 5-4 Conduction anisotropy demonstrated by the directional dependence of the chevron films resistivity[142]

5.3 Sensor Design

Several factors combined to limit the options available for the initial STF sensor designs. The most elegant design for these types of sensors uses the solid “capping layer” formation. This formation allows vertically oriented structures, e.g. pillars or helices, to be connected in parallel using top and bottom electrodes. With this type of structure, the area dimensions of the electrodes, and the thickness of the active films can be precisely controlled. Furthermore, vertical isolation of the sensor pathway reduces any affect of parallel capacitance as may exist through the substrate with a horizontal design. The vertical design also limits the effect of any conduction pathway in the initial “scrub layer”. These factors make characterization of any capacitance measurements (and by extension the sensor response) significantly more direct. Unfortunately, the e-beam deposition system used for this research does not possess the capability to change the flux angle of incidence *in-situ*, and therefore cannot create the smooth transition to a capping layer shown in Figure 5-2. As a result, the sensor design was limited to a horizontal path between electrical contacts.

The need to use a horizontal measurement path forced the focus toward a conductive sensor design, i.e. the traditional MOS sensor operation as opposed to the capacitive humidity sensors using STF formations described earlier in the section. Fortunately, the focus in recent years on nano-scale crystalline materials fabrication has renewed interest in micro-scale sensors. This interest has to several recent discoveries using nano-scale anatase TiO₂ as a conductive sensor. Varghese published an important paper (over 40 citations to date) in 2003 which demonstrated a hydrogen sensor based on anatase nano-tubes with a measured

sensitivity, $S = (R_0 - R_{\text{gas}})/R_{\text{gas}}$, of nearly 10^3 for 1000 ppm H_2 in nitrogen.[11] Also, nano-sized titania sensors produced by dip coating have shown promise for sensing simple alcohols as ethanol, methanol, and n-propanol.[13] This sensitivity to simple organic compounds (alcohols) indicates the sensor design may be used for more complex volatile organic compounds (VOCs). The detection and qualification of complex VOCs is the fundamental aspect of e-nose development.

One of the major difficulties in characterizing the conductive film sensors is the large resistances associated with the films. The resistance of a semiconducting bar with contacts at each end is:

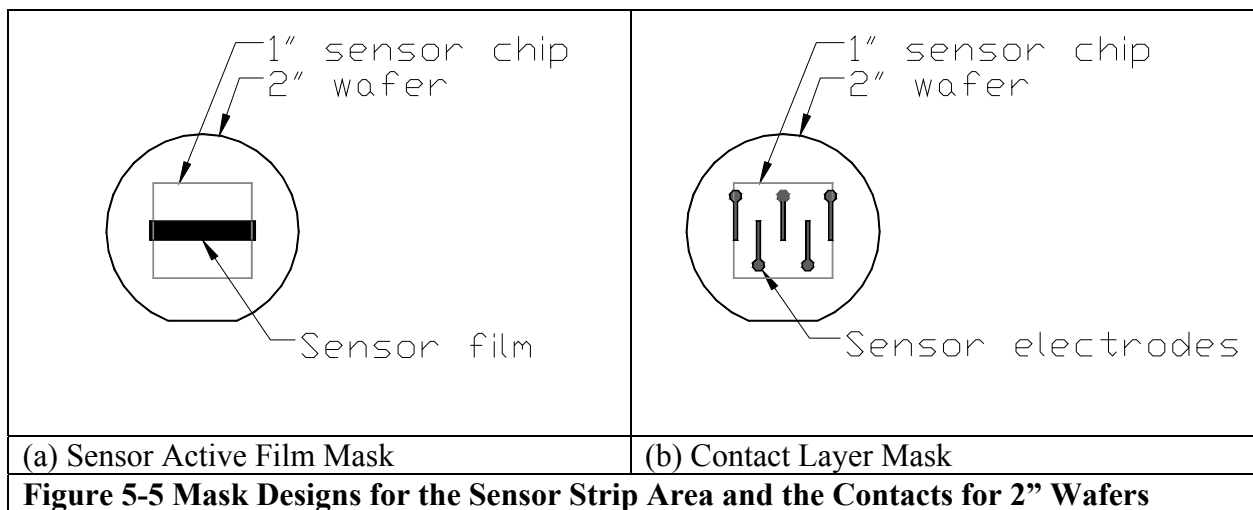
$$R = \rho L/wt \quad [\text{Eq. 5-1}]$$

where R is the resistance, ρ is the resistivity of the material, L is the length of the film from contact to contact, w is the width of the film, and t is the film thickness. Since the resistance is inversely proportional the thickness, the resistance of semiconducting thin film ($< 1 \mu\text{m}$) sensors can easily reach the megaohm range. One method commonly used to reduce a sensor resistance is to use an InterDigitated Array (IDA) for the contacts. With an IDA contact design, the width of the contact is increased dramatically, while the length between contacts is kept very short. Unfortunately, the highly oblique angle necessary to deposit the STFs limits the ability to deposit the films between closely spaced electrode formations. Therefore, an alternative sensor design is required for these sensors.

A transmission line design was chosen for the initial (alpha) sensor. With this design, multiple contacts are defined along an extended line of film. The contacts at the end of the lines are used to drive a constant current through the film, while the voltages are measured at the contacts distributed along the bulk of the film. The structure (Figure 5-3) used for the anisotropic conductivity measurements previously discussed is an example of a transmission line sensor.[142] For the initial (alpha) sensor, the sensor strip was a straight line rectangle, 5mm wide and 25 mm in length. The contacts were 1 mm wide cross-strips with 4 mm separation between contacts. The design allows measurements of several different lengths of sensors (to pick a convenient resistance range) as well as the insurance of additional sensors if one section of the line is damaged. The masks used to define the active film strip area and the contacts for 2" wafers are shown in Figure 5-5. A similar mask with (4) sensors has been created for use with 3" wafers.

The fabrication of the alpha sensor started with AZ5214E photoresist spun at 6000 rpm on a 2" n-type silicon wafer with a 100 nm thermal oxide layer grown by the vendor. The thickness of the resist was measured to be ~1200 nm by a Dektak profilometer. The mask in Figure 5-5(a) was used to define an open strip area in the resist. The chevron formation was deposited using the TiO_x (Anatase) process detailed in Table 4-1. The flux angle of incidence was 80° . The wafer was oriented with the flux direction parallel to the long axis of the strip. The wafer was rotated 180° after every 3000\AA of deposition as measured by the normal incidence crystal monitor. A total of seven rotations produced 4 complete chevron layers for a total deposition of $2.4\ \mu\text{m}$ (by crystal monitor). After the deposition, acetone was used as the photoresist solvent for a lift-off of the film outside the strip area. After successive

methanol and DI water rinses, the samples were dried for at least 24 hours and then annealed for one hour at 450 °C in oxygen. Nickel contacts were deposited by e-beam evaporation atop the films at normal incidence through a proximity shadow mask machined to the specifications in Figure 5-5(b). The contact depositions were 1000Å as measured by the crystal monitor. The top-down contact design was successfully utilized with chevron STFs in the conduction anisotropy experiments published by Vick.[142]



5.4 Sensor Test Chamber

In order to characterize the sensor with respect to gas concentration, a test chamber was fabricated. The major design elements for a gas sensor test chamber are small size, atmospheric integrity, ease of electrical connections, and the ability to modulate the sensor temperature. Temperature modulation is a key factor in qualifying MOS gas sensor response. The sensor chamber design is shown in Figure 5-6. A pyrolytic graphite and pyrolytic boron-

nitride heating stage is centered in the chamber. The heater element can produce sensor temperatures in excess of 450 °C at 30% power from a 120V Variac power supply. The heater element has a very low thermal mass which allows the temperature to be lowered quickly. The chamber volume excluding the heater element is 143cc. The heater element power is provided through connections at the bottom of the chamber, while the electrical connections to the sensor enter through the chamber sides just above the sensor level. One thermocouple probe contacts the substrate surface to measure the sensor temperature. A second thermocouple mounted below the heating element monitors the chamber wall temperature. The top of the chamber is sealed with a 1/8 in. viton o-ring.

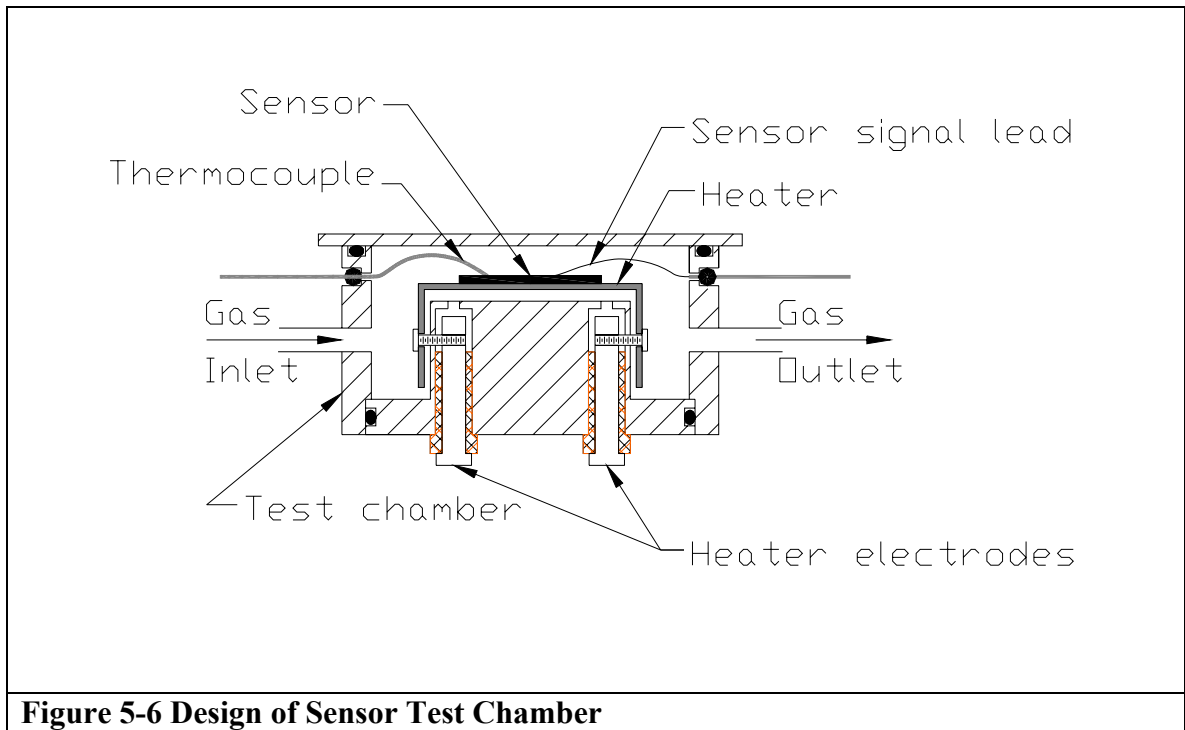


Figure 5-6 Design of Sensor Test Chamber

5.5 Sensor Materials Characterization

The first step in the sensor characterization is confirming the physical and material properties of the chevron sensor films. As discussed earlier, the chevron films were deposited with the $\text{TiO}_x(\text{A})$ process at a flux angle of 80° . Figure 5-7 shows the as deposited SEM images of the chevron formation deposited at the same conditions as the alpha sensors. The images are (a) the edge view, (b) a 30° planar view, and (c) a high magnification view (140KX) of the top leg of one chevron. The total thickness of the formation is approximately 1500 nm or $\sim 63\%$ of the total normal incidence deposition (crystal monitor).

A key aspect of the alpha sensor is the ability to create an anatase structure via post deposition anneals. Typically, STF structures which are in contact with their neighbors exhibit more structural damage via sintering during an anneal step. Some film damage may be beneficial to the sensor performance as the sintering will increase the contact between neighboring chevrons. But too much film contraction would destroy the STF chevron formation. For this sensor, an optimal anneal would (1) create an anatase film, (2) increase the number of horizontal conduction paths through the film, and (3) still maintain a recognizable chevron structure. Figure 5-8 shows SEM images (edge view, 30° planar view, and 140KX on a chevron leg) for the chevron film after a one hour anneal at 450°C in oxygen. These images are analogous to those in Figure 5-6. From the edge view (a), some damage is visible in the foreground area. However, for films with significant contact between the features, the cleave process to prepare the sample for SEM can produce more damage near the cleave area. The 30° planar view (b) confirms a recognizable chevron structure still

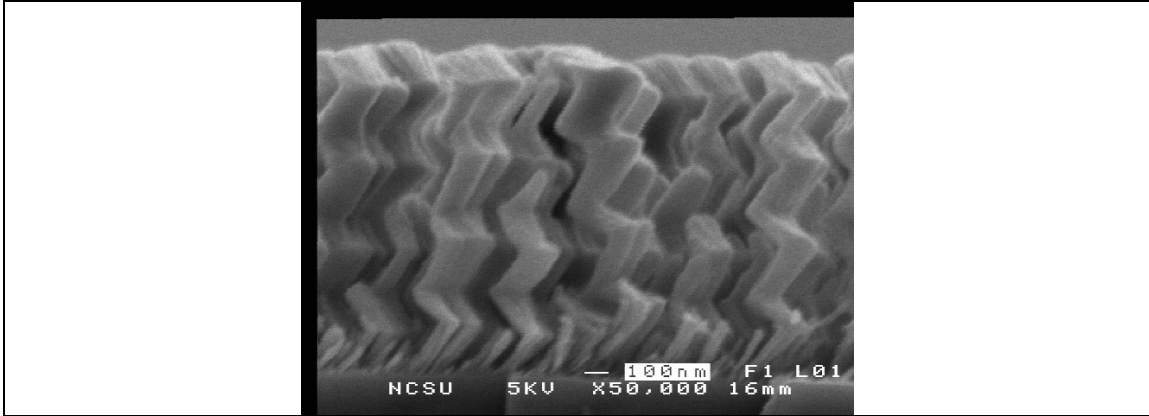


Figure 5-7(a) Edge View SEM Image of the As Deposited 4-layer Chevron Formation Used for the Alpha Sensor

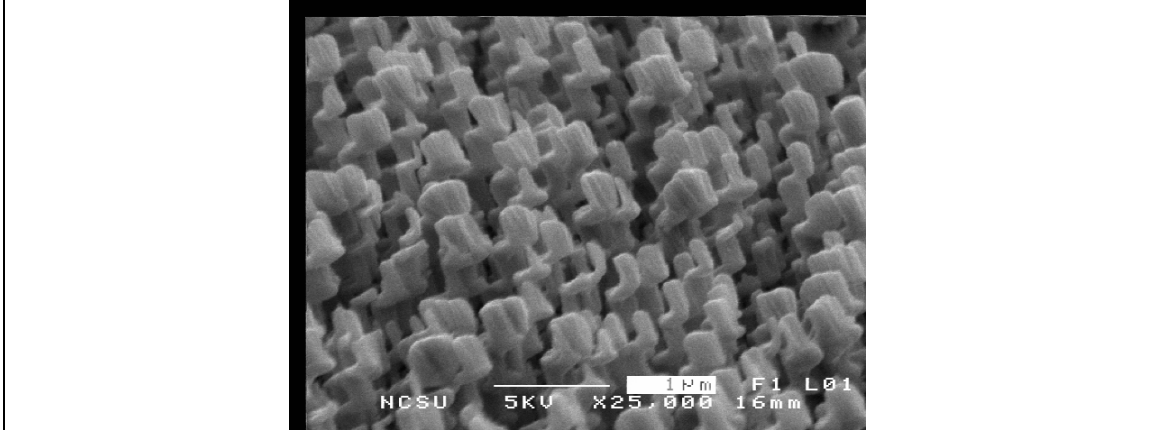


Figure 5-7(b) Planar View (30°) SEM Image of the As Deposited 4-layer Chevron Formation Used for the Alpha Sensor

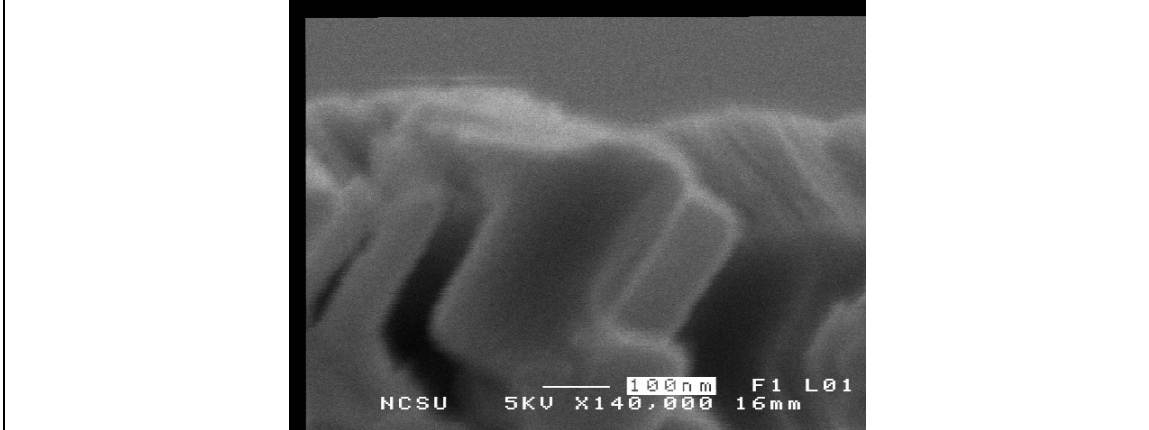


Figure 5-7(c) High Magnification View (140KX) SEM of a Single Chevron Formation Used for the Alpha Sensor

Figure 5-7 SEM Images of Chevron Formation

exists across the entire viewing range, although some localized sintering has occurred. The high magnification image, (c), of the chevron leg illustrates striations along the primary growth axis of the leg. The striations probably indicate grain boundaries between long anatase crystals.

The materials characterization of the alpha sensor films was conducted with XRD measurements. Figure 5-9 (a-c) contains the XRD patterns for the alpha chevron formation. Panel (a) shows the XRD data for the as deposited film. As expected from the $\text{TiO}_x(\text{A})$ pillar characterizations, the as deposited sample has very little crystallinity. Panel (b) exhibits the XRD data for the sample after a one hour anneal at 450°C in oxygen. The XRD pattern is consistent with the pillar formations detailed in earlier chapters with the well-defined anatase (101) peak at 25.2° . The final panel (c) shows the same sample as in panel (b), but after a subsequent anneal for one hour at 750°C in 5% H_2/N_2 forming gas. The forming gas anneal simulates sensor operation in a harsh reducing environment and as a result serves to test the integrity of the anatase films under these conditions. The data shows only a small amount of rutile formation is evident from the small peak forming near 27.4° which would indicate rutile (110).

5.6 Sensor Electrical Characterization

The initial sensor characterization focused on the response of the sensor response in air, argon, and 5% H_2/Ar forming gas. Mass flow controllers were connected on the argon (1000 sccm) and forming gas (200 sccm) lines order to vary the concentration of the hydrogen in

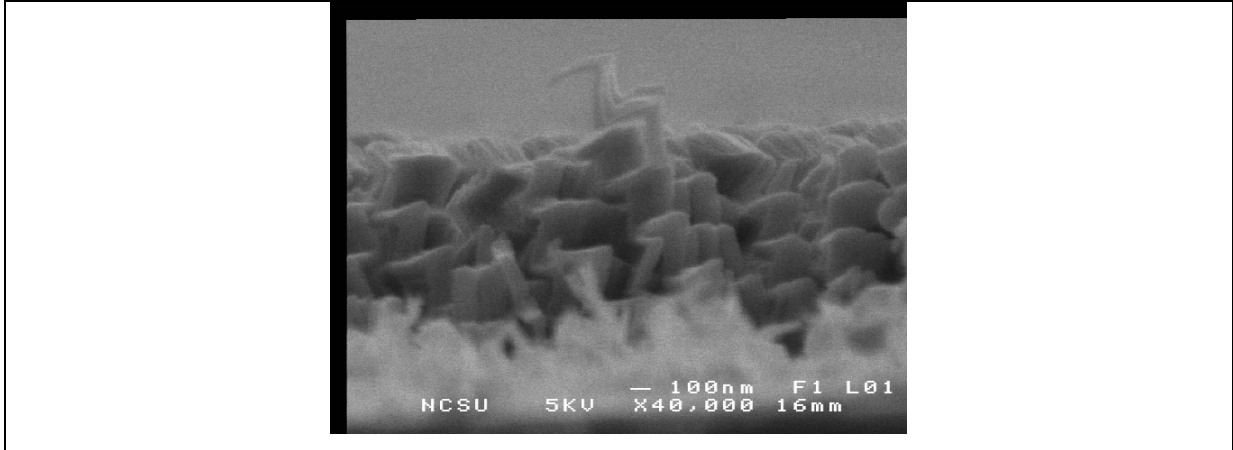


Figure 5-8(a) Edge View SEM Image of the 4-layer Chevron Formation Used for the Alpha Sensor After 1 hour, 450 °C Anneal in Oxygen

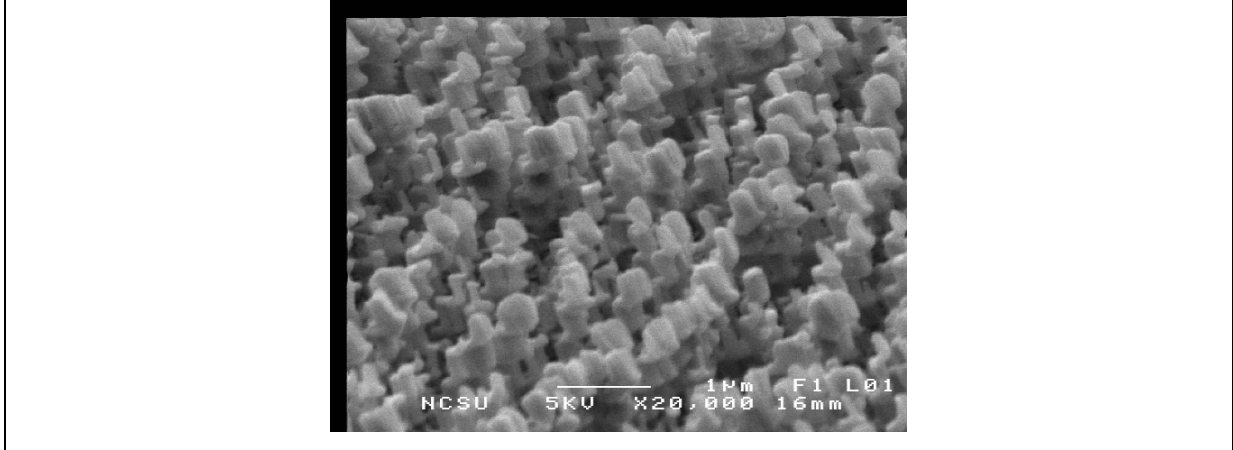


Figure 5-8(b) Planar (30°) View SEM Image of the 4-layer Chevron Formation Used for the Alpha Sensor After 1 hour, 450 °C Anneal in Oxygen

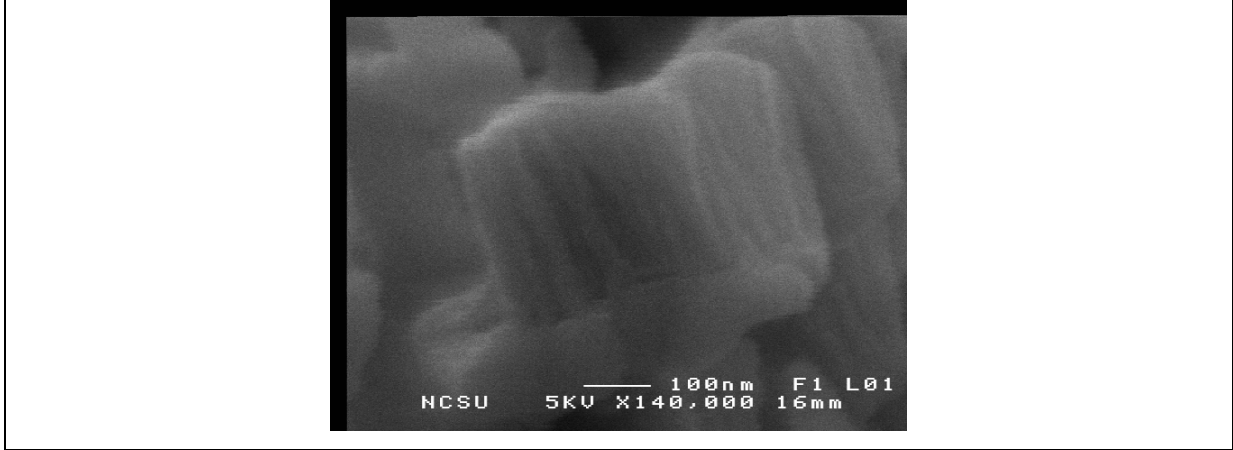
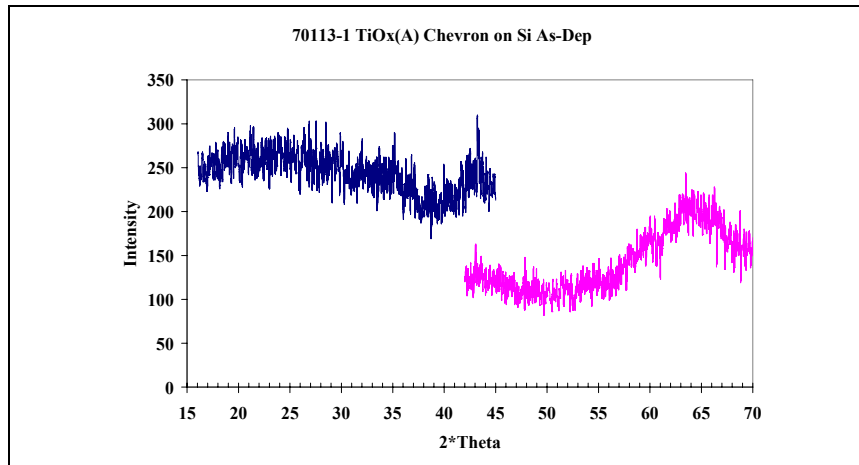
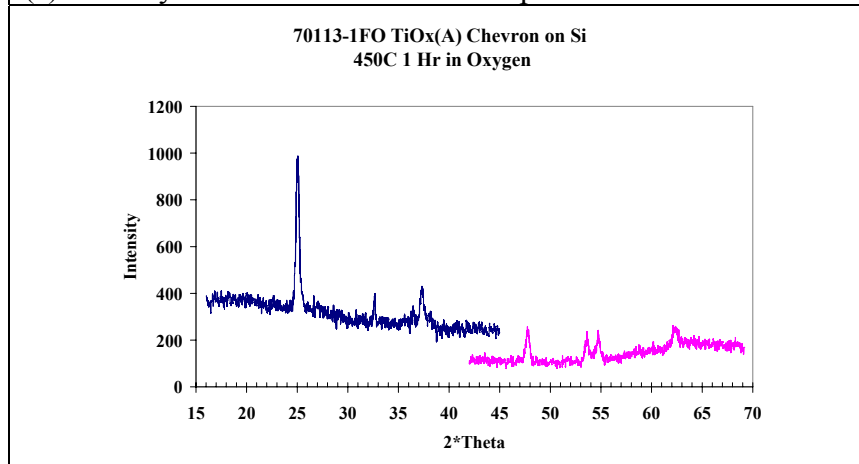


Figure 5-8(c) High Magnification View (140KX) SEM Image of Chevron Formation Used for the Alpha Sensor After 1 hour, 450 °C Anneal in Oxygen

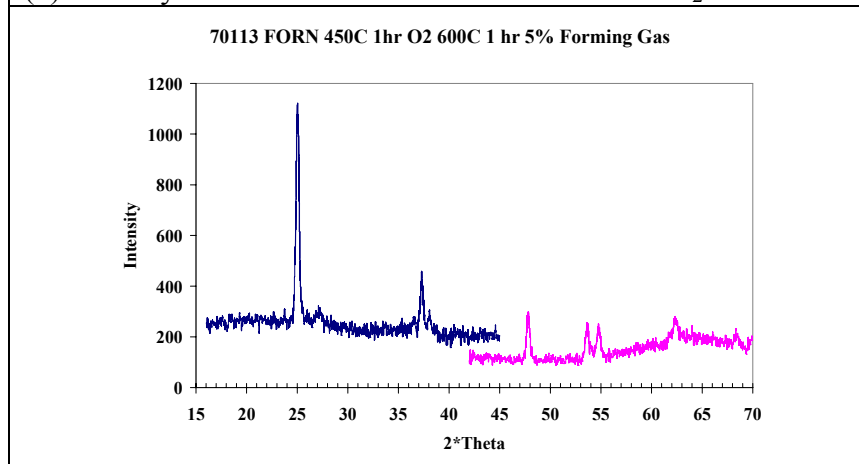
Figure 5-8 SEM of Anatase Chevron Formation



(a) Four layer chevron formation as-deposited



(b) Four layer chevron formation 1 hour anneal in O₂



(c) Four layer chevron formation 1 hour anneal in O₂—
subsequent anneal 1 hour in 5% H₂/N₂ Forming Gas

**Figure 5-9 XRD Patterns For Four Layer Chevron
Formation Used For The Alpha Sensor**

the sensor stream below the 5% range. The electrical connections to the sensor through the chamber walls proved to be quite challenging. Initially, the wires were supposed to contact the nickel pads via spring tensions, but this was quickly identified as problematic. The second solution was to solder the wires to the nickel contacts using indium metal. This connection was used for the initial data presented.

For the initial tests, a single 4 mm long section of the sensor strip was used due to concerns over the potentially high resistance of the films. Constant current was provided by a Keithley 224 current source. Voltage measurements were taken with an HP 3465A voltmeter. The current ranges were 0.2-1.0 μA . The sample was heated with open loop power settings and allowed to stabilize within a small temperature range. The resistance versus temperature curve for a current of 1.0 μA with the top plate of the chamber removed (to test in air) is shown in Figure 5-10. The resistance values were much higher than expected for the films. However, the increase in the resistance as a function of temperature in air is consistent with MOS sensor operation. At temperatures in the 200-400 $^{\circ}\text{C}$ range, $(\text{O}_2)^{\cdot-}$ oxygen species are likely to desorb and be replaced by species with higher charge density ($\text{O}^{\cdot-}$ or O^{-2}) on the sensor surface.[6] For an n-type sensor material (anatase), the additional loss of electrons increases the resistance.

The next set of measurements were taken with the chamber sealed and an argon flow of 200 sccm. The argon flowed for 3 hours to condition the test chamber. The outlet of the chamber is run through a bubbler to minimize back diffusion of air. Figure 5-11 shows the resistance versus temperature curve for a current of 1.0 μA . Initially, the resistance was in the 10 $\text{M}\Omega$

range consistent with the values in air. Around 208 °C, the resistance dropped quickly to the 2 MΩ range and then decreased further with respect to an increase in temperature. Initially, this drop in resistance was reversible, but as can be seen from the graph, after the temperature reached 400 °C, the subsequent decreasing temperature curve had a large amount of hysteresis. After 70° C was reached, increasing the temperature produced results along the same line as the decreasing temperature data in the graph. One additional factor was the introduction of 5% H₂ forming gas at the 400 °C temperature (this will be discussed in the next paragraph) before the decreasing temperature data was taken. After the sensor had cooled, the argon flow was reduced to 5 sccm (the minimum to keep the outlet bubbling). After 12 hours, additional testing again showed higher initial resistance, with a decrease after 200 °C, but the effect was not as pronounced. The stability of the voltages was inconsistent for several flow and temperature conditions.

As mentioned, at 400 °C hydrogen was introduced in increasing steps from 1000 ppm to a maximum of 5%. The heater was operating in an open loop mode. Any increase in the hydrogen content decreased the temperature of the sensor, which produced a corresponding increase in the resistance. However, after adjusting the power setting to regain the initial temperature, the initial resistance also recovered. Additional hydrogen testing over the multiple temperatures from 200 °C to 450 °C produced similar results.

The hysteresis evident in Figure 5-11 may have several causes, but two options are likely. Both nickel and indium will form oxides, so the initial contact between the wire, indium solder, and nickel pad may have contained a large contact resistance. At room temperature,

the wire contact was easily dislodged however from the pad and had to be re-soldered several times with more indium. Indium melts in the 200 °C range where the initial drop in resistance was seen, which may have resulted in better electrical contact across the connection. After cooling, the stress from the wire tension may have slightly dislodged the contact, followed by a repeating cycle of melt-resistance drop. The other option is the large scale desorption of $(O_2)^-$ described earlier. The introduction of hydrogen at 400 °C would have further acted to reduce the background oxygen in the chamber and limit any adsorption effect over the short time frame. However, overnight the argon flow was reduced to a low level. Although the bubbler would limit back diffusion of air, the vacuum integrity of the chamber is unknown, especially at the measurement feedthroughs. Also, the argon is not ultra-high (semiconductor grade) so over 12 hours the background oxygen may have been replenished enough to again affect the sensor performance.

The insensitivity to hydrogen is not unexpected given the choice of contact material. The first choice of the author was platinum, as it is used in over 90% of the papers reviewed by the author for use with TiO_2 . The only other electrode materials reported are palladium, chrome, gold, or a combination of chrome/gold. Platinum is especially prevalent for hydrogen sensors as the sensing mechanism may be related to the Schottky barrier height between the Pt and the anatase. In any case, the catalytic effect of platinum on the dissolution of hydrogen enhances any attempt at a hydrogen sensor. However, concerns over the robustness of the sculptured thin film to a sputtering process and cost issues lead to the use of nickel for the prototype alpha sensor.

5.7 Sensor Conclusions and Future Work

Test structures using sculptured thin films have been fabricated. The sensor demonstrates a response to a large change in ambient oxygen in the resistance versus temperature data. The evaporation of contacts (top-down) through a shadow mask did make sufficient contact with the sensor film to see a response versus temperature in both argon and air. A large hysteresis effect associated with the temperature response may be related to problems with the wire connection to the contact pads. The sensor response to hydrogen from 0-5% in argon was indistinguishable from the temperature response caused by the high thermal conductivity of the hydrogen.

Several enhancements have already been made to the sensor test system. A temperature controller has been connected to heater stage to counter the effect of changes in the gas conductivity automatically. A bubbler has been fabricated on the front end of the gas inlet to use for humidity, alcohol, or more complex VOC sensing. Future sensors of this type for hydrogen should utilize platinum contacts.

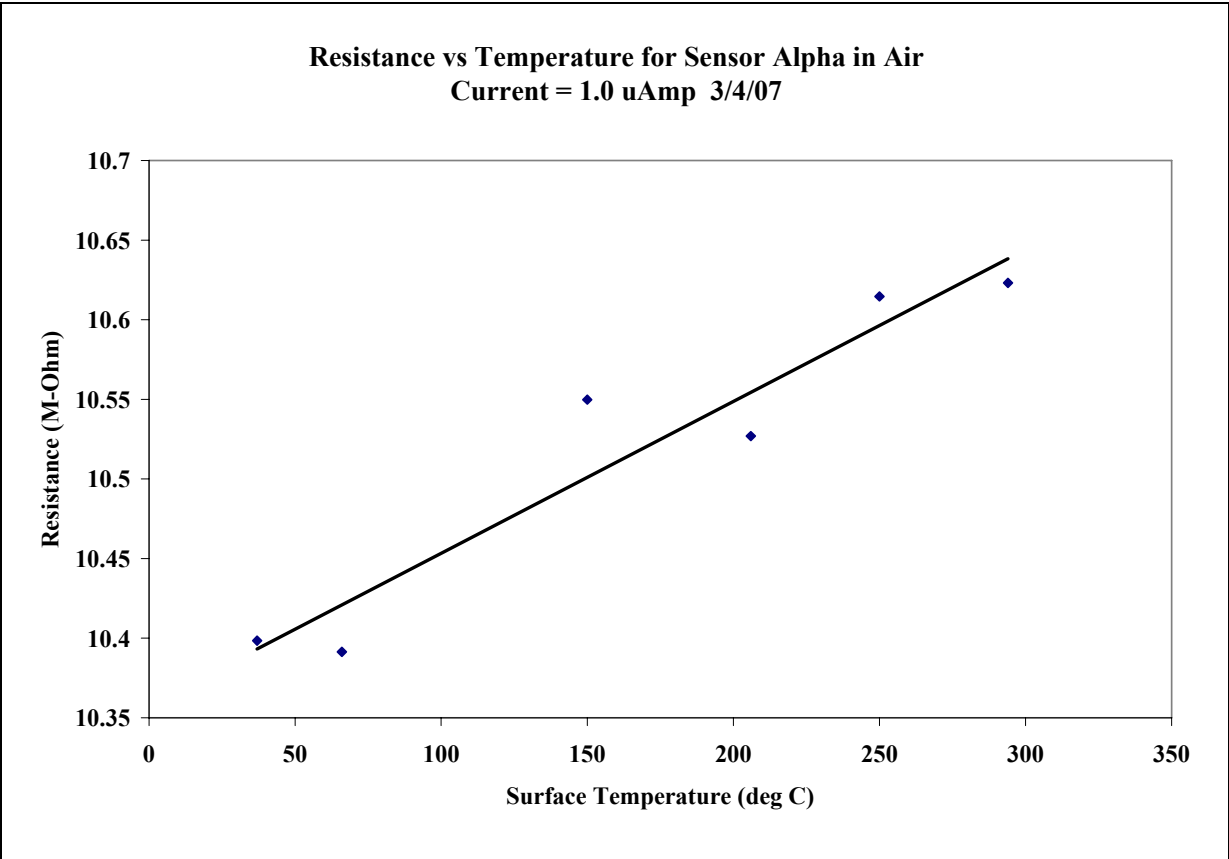
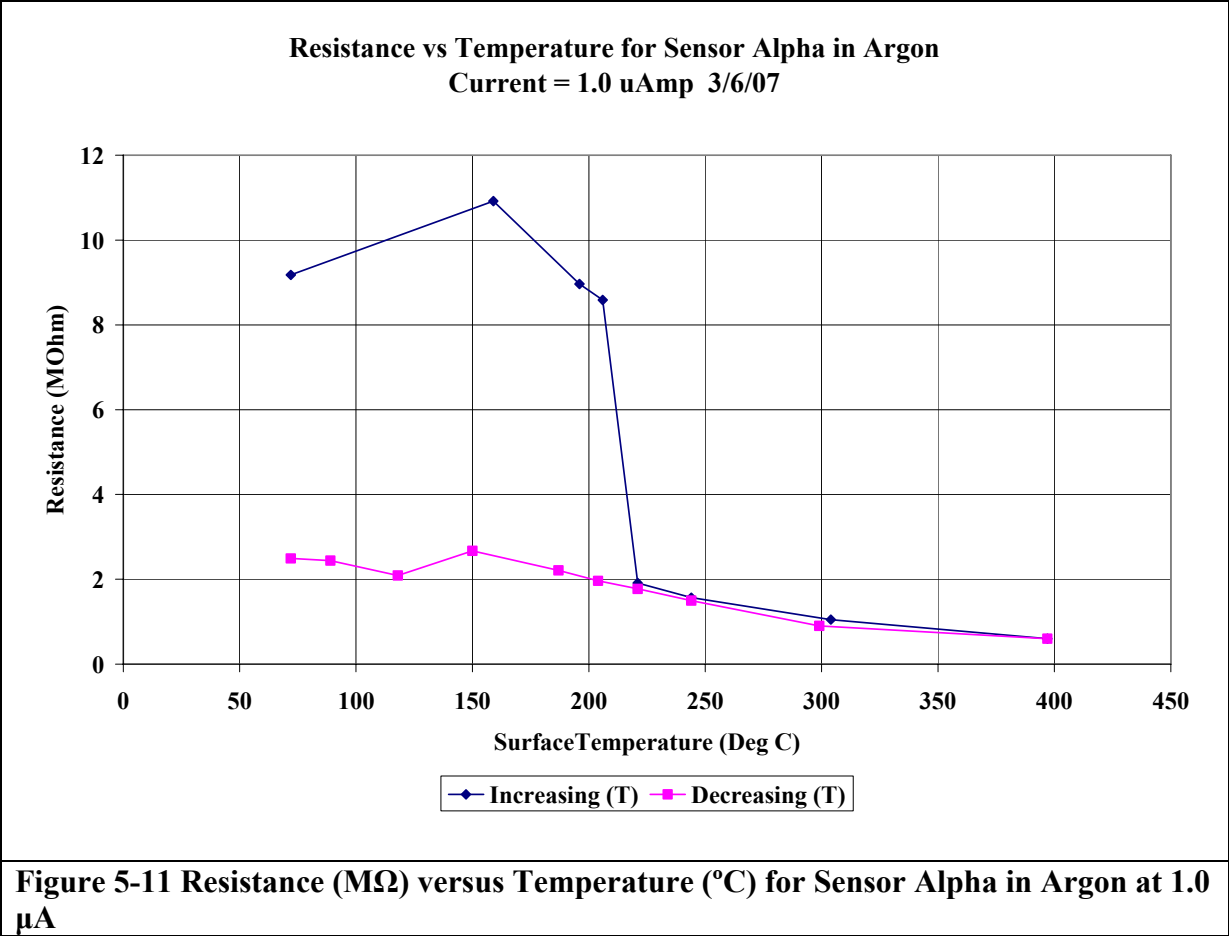


Figure 5-10 Resistance (MΩ) versus Temperature (°C) Data at 1.0 μA for Alpha Sensor in Air



Chapter 6

Conclusions and Future Work

6.1 Conclusions

The main goal of this research has been the application of glancing angle deposition techniques to create highly porous sculptured thin films (STF) structures for use as gas sensors. The glancing angle technique utilizes physical vapor depositions at highly oblique ($>70^\circ$) angles of incidence to form porous film structures. The dual e-beam evaporator in the NCSU BioMedical MicroSensors Laboratory (BMMSL) was modified with a new wafer stage mounted for glancing angle depositions. The angle of incidence can be varied from 76° to 82° using a set screw when the substrate is loaded. The stage can be rotated using a magnetic rotational drive mounted to an electrical motor. Process conditions including the deposition rate, rotation speed, and flux angle were investigated to produce pillar and chevron formations.

The Ti-TiO₂ materials system was chosen as the metal oxide semiconductor (MOS) sensor material. The existence of two stable TiO₂ polymorphic phases in anatase and rutile which have both been widely used as sensors provided flexibility in the fabrication and design of the sensor. As both phases have different materials properties, it is desirable to control the anatase/rutile percentage in the sensor films. A combination of initial deposition conditions and post deposition annealing/oxidation treatments was determined to optimize the formation of the respective phases.

The glancing angle technique has been shown to produce films with preferred crystal orientations and texturing which differ based on the angle of incidence. A series of experiments looked at the effect of the angle of incidence, the deposition conditions, and the substrate material on the crystal structure of the STF structures. Additionally, a series of annealing/oxidation experiments investigated the response of the isolated STF structures with respect to oxidation times, crystal structure, and the anatase-rutile transformation.

A conductive MOS sensor was designed based on an anatase chevron formation. The sensor was fabricated using nickel contacts along a transmission line layout. Following the fabrication of a sensor test chamber, the sensor response was characterized versus temperature for inert, oxidizing, and reducing atmospheres.

The primary results of this research are summarized below:

- Thin film pillars and chevrons were fabricated using the glancing angle deposition techniques with pillar widths on the order of 50-200 nm.
- Deposition conditions/annealing conditions were identified to produce TiO_x films which were more likely to create either anatase or rutile phase pillars
- The critical deposition parameter for anatase formation is an increased oxygen partial pressure to minimize the number of oxygen vacancies in the TiO_x films prior to annealing.
- The crystalline structure of the deposited titanium films does depend on the deposition angle of incidence.

- An unidentified XRD peak at a 2θ value of 31.5° was present for all of the titanium depositions at an angle of 76° . Further materials characterization is necessary to identify the crystalline structure and/or composition of these films
- The annealing studies revealed the anatase pillar formations are stable with respect to rutile transformation at higher temperatures than normally reported. This stability is likely due to the small scale system independence of each STF structure.
- The high temperature oxidation of the titanium pillars produced rutile pillars with markedly different XRD patterns (preferred crystal orientation) than the TiO_x pillar formations.
- The SEM images of the titanium films after a high temperature annealing revealed a unique film topography which is not readily explained. More investigation is needed to describe the sintering/oxidation process with these small scale pillars.
- An anatase sensor chevron was fabricated with top-down evaporated nickel contacts. Initial characterization showed a working thin film conductive device with a measurable difference in the temperature response in an oxidizing versus a reducing atmosphere.
- The sensor electrical response to hydrogen was indistinguishable to the temperature response induced by the change in thermal conductivity of the gas. The nickel contact may not be a viable design for a hydrogen sensor.

6.2 Future Work

The primary limitation of the dual e-beam system used for this work is the inability to change the angle of incidence during the deposition process. This *in-situ* ability is critical to the

formation of advanced STF formations, including a smooth transition to a solid capping layer. This modification would greatly enhance the capability to create novel sensor designs, including those utilizing optically responsive films.

The limited materials characterization (SEM and XRD) available for this research discovered several anomalous factors which could not be adequately identified solely by these techniques. Confirmation/qualification of the physical reasons for these anomalies through additional materials characterization could produce graphic insights into nano-scale materials properties.

Finally, the concept of the STF conductivity sensor was shown with response to oxygen and argon. However, improvements in the electrical contact to the nickel pads should allow a more comprehensive analysis. Also, the affect of variations in sensor material (anatase/rutile), sensor design (chevron/pillar), chamber conditions (temperature modulation), and measurement technique (impedance spectroscopy) on the sensor response opens up significant avenues for research.

Bibliography

- [1] J. W. Gardner and P. N. Bartlett, *Electronic Noses: Principles and Applications*. Oxford, New York: Oxford University Press, 1999.
- [2] R. Dutta, D. Morgan, N. Baker, J. W. Gardner, and E. L. Hines, "Identification of *Staphylococcus aureus* infections in hospital environment: electronic nose based approach," *Sensors and Actuators B-Chemical*, vol. 109, pp. 355-362, 2005.
- [3] P. Gouma, G. Sberveglieri, R. Dutta, J. W. Gardner, and E. L. Hines, "Novel materials and applications of electronic noses and tongues," *MRS Bulletin*, vol. 29, pp. 697-700, 2004.
- [4] R. Dutta, K. R. Kashwan, M. Bhuyan, E. L. Hines, and J. W. Gardner, "Electronic nose based tea quality standardization," *Neural Networks*, vol. 16, pp. 847-853, 2003.
- [5] J. W. Gardner, H. W. Shin, E. L. Hines, and C. S. Dow, "An electronic nose system for monitoring the quality of potable water," *Sensors and Actuators B-Chemical*, vol. 69, pp. 336-341, 2000.
- [6] G. Eranna, B. C. Joshi, D. P. Runthala, and R. P. Gupta, "Oxide materials for development of integrated gas sensors - A comprehensive review," *Critical Reviews in Solid State and Materials Sciences*, vol. 29, pp. 111-188, 2004.
- [7] B. Dick, M. J. Brett, and T. Smy, "Controlled growth of periodic pillars by glancing angle deposition," *Journal of Vacuum Science & Technology B*, vol. 21, pp. 23-28, 2003.
- [8] K. Robbie and M. J. Brett, "Sculptured thin films and glancing angle deposition: Growth mechanics and applications," *Journal of Vacuum Science & Technology a-Vacuum Surfaces and Films*, vol. 15, pp. 1460-1465, 1997.
- [9] N. Savage, B. Chwieroth, A. Ginwalla, B. R. Patton, S. A. Akbar, and P. K. Dutta, "Composite n-p semiconducting titanium oxides as gas sensors," *Sensors and Actuators B-Chemical*, vol. 79, pp. 17-27, 2001.

- [10] W. T. Moon, K. S. Lee, Y. K. Jun, H. S. Kim, and S. H. Hong, "Orientation dependence of gas sensing properties of TiO₂ films," *Sensors and Actuators B-Chemical*, vol. 115, pp. 123-127, 2006.
- [11] O. K. Varghese, D. W. Gong, M. Paulose, K. G. Ong, and C. A. Grimes, "Hydrogen sensing using titania nanotubes," *Sensors and Actuators B-Chemical*, vol. 93, pp. 338-344, 2003.
- [12] O. K. Varghese and C. A. Grimes, "Metal oxide nanoarchitectures for environmental sensing," *Journal of Nanoscience and Nanotechnology*, vol. 3, pp. 277-293, 2003.
- [13] L. P. Sun, L. H. Huo, H. Zhao, S. Gao, and J. G. Zhao, "Preparation and gas-sensing property of a nanosized titania thin film towards alcohol gases," *Sensors and Actuators B-Chemical*, vol. 114, pp. 387-391, 2006.
- [14] T. Karabacak, G. C. Wang, and T. M. Lu, "Quasi-periodic nanostructures grown by oblique angle deposition," *Journal of Applied Physics*, vol. 94, pp. 7723-7728, 2003.
- [15] H. Alouach and G. J. Mankey, "Texture orientation of glancing angle deposited copper nanowire arrays," *Journal of Vacuum Science & Technology A*, vol. 22, pp. 1379-1382, 2004.
- [16] K. D. Harris, D. Vick, T. Smy, and M. J. Brett, "Column angle variations in porous chevron thin films," *Journal of Vacuum Science & Technology a-Vacuum Surfaces and Films*, vol. 20, pp. 2062-2067, 2002.
- [17] T. Karabacak, G. C. Wang, and T. M. Lu, "Physical self-assembly and the nucleation of three-dimensional nanostructures by oblique angle deposition," *Journal of Vacuum Science & Technology A*, vol. 22, pp. 1778-1784, 2004.
- [18] J. Lintymer, J. Gavaille, N. Martin, and J. Takadoum, "Glancing angle deposition to modify microstructure and properties of sputter deposited chromium thin films," *Surface & Coatings Technology*, vol. 174, pp. 316-323, 2003.
- [19] R. Messier and A. Lakhtakia, "Sculptured thin films - II. Experiments and applications," *Materials Research Innovations*, vol. 2, pp. 217-222, 1999.

- [20] M. Suzuki and Y. Taga, "Integrated sculptured thin films," *Japanese Journal of Applied Physics Part 2-Letters*, vol. 40, pp. L358-L359, 2001.
- [21] R. Messier, T. Gehrke, C. Frankel, V. C. Venugopal, W. Otano, and A. Lakhtakia, "Engineered sculptured nematic thin films," *Journal of Vacuum Science & Technology a-Vacuum Surfaces and Films*, vol. 15, pp. 2148-2152, 1997.
- [22] H. Vankranenburg and C. Lodder, "Tailoring Growth and Local Composition by Oblique-Incidence Deposition - a Review and New Experimental-Data," *Materials Science & Engineering R-Reports*, vol. 11, pp. 295-354, 1994.
- [23] I. Petrov, P. B. Barna, L. Hultman, and J. E. Greene, "Microstructural evolution during film growth," *Journal of Vacuum Science & Technology A*, vol. 21, pp. S117-S128, 2003.
- [24] B. A. Movchan and Demchish.AV, "Study of Structure and Properties of Thick Vacuum Condensates of Nickel, Titanium, Tungsten, Aluminium Oxide and Zirconium Dioxide," *Physics of Metals and Metallography-Ussr*, vol. 28, pp. 83-&, 1969.
- [25] J. A. Thornton, "High-Rate Thick-Film Growth," *Annual Review of Materials Science*, vol. 7, pp. 239-260, 1977.
- [26] R. Messier and J. E. Yehoda, "Geometry of Thin-Film Morphology," *Journal of Applied Physics*, vol. 58, pp. 3739-3746, 1985.
- [27] P. B. Barna and M. Adamik, "Fundamental structure forming phenomena of polycrystalline films and the structure zone models," *Thin Solid Films*, vol. 317, pp. 27-33, 1998.
- [28] N. Young and J. Kowal, "Optically Active Flourite Films," *Nature*, vol. 183, pp. 104-105, 1959.
- [29] M. Levichkova, V. Mankov, N. Starbov, D. Karashanova, B. Mednikarov, and K. Starbova, "Structure and properties of nanosized electron beam deposited zirconia thin films," *Surface & Coatings Technology*, vol. 141, pp. 70-77, 2001.

- [30] Nieuwenh.Jm and H. B. Haanstra, "Microfractography of Thin Films," *Philips Technical Review*, vol. 27, pp. 87-&, 1966.
- [31] T. Motohiro and Y. Taga, "Thin-Film Retardation Plate by Oblique Deposition," *Applied Optics*, vol. 28, pp. 2466-2482, 1989.
- [32] R. T. Kivaisi, "Optical-Properties of Obliquely Evaporated Aluminum Films," *Thin Solid Films*, vol. 97, pp. 153-163, 1982.
- [33] B. A. Orlowski, W. E. Spicer, and A. D. Baer, "Obliquely Deposited Amorphous-Germanium Films," *Thin Solid Films*, vol. 34, pp. 31-34, 1976.
- [34] O. R. Monteiro, A. Vizir, and G. Brown, "Multilayer thin-films with chevron-like microstructure," *Journal of Physics D-Applied Physics*, vol. 31, pp. 3188-3196, 1998.
- [35] K. Robbie, L. J. Friedrich, S. K. Dew, T. Smy, and M. J. Brett, "Fabrication of Thin-Films with Highly Porous Microstructures," *Journal of Vacuum Science & Technology a-Vacuum Surfaces and Films*, vol. 13, pp. 1032-1035, 1995.
- [36] K. Robbie, M. J. Brett, and A. Lakhtakia, "First Thin-Film Realization of a Helicoidal Bianisotropic Medium," *Journal of Vacuum Science & Technology a-Vacuum Surfaces and Films*, vol. 13, pp. 2991-2993, 1995.
- [37] R. M. A. Azzam, "Chiral Thin Solid Films - Method of Deposition and Applications," *Applied Physics Letters*, vol. 61, pp. 3118-3120, 1992.
- [38] R. Messier, "Collaboration between Lakhtakia and Robbie," W. Kiether, Ed., 2002.
- [39] K. Robbie, J. C. Sit, and M. J. Brett, "Advanced techniques for glancing angle deposition," *Journal of Vacuum Science & Technology B*, vol. 16, pp. 1115-1122, 1998.
- [40] K. Robbie, C. Shafai, and M. J. Brett, "Thin films with nanometer-scale pillar microstructure," *Journal of Materials Research*, vol. 14, pp. 3158-3163, 1999.

- [41] F. Liu, M. T. Umlor, L. Shen, J. Weston, W. Eads, J. A. Barnard, and G. J. Mankey, "The growth of nanoscale structured iron films by glancing angle deposition," *Journal of Applied Physics*, vol. 85, pp. 5486-5488, 1999.
- [42] T. Smy, D. Vick, M. J. Brett, S. K. Dew, A. T. Wu, J. C. Sit, and K. D. Harris, "Three-dimensional simulation of film microstructure produced by glancing angle deposition," *Journal of Vacuum Science & Technology A*, vol. 18, pp. 2507-2512, 2000.
- [43] T. Smy, D. Walkey, K. D. Harris, and M. J. Brett, "Thin film microstructure and thermal transport simulation using 3D-films," *Thin Solid Films*, vol. 391, pp. 88-100, 2001.
- [44] M. Suzuki and Y. Taga, "Numerical study of the effective surface area of obliquely deposited thin films," *Journal of Applied Physics*, vol. 90, pp. 5599-5605, 2001.
- [45] R. N. Tait, T. Smy, and M. J. Brett, "Modeling and Characterization of Columnar Growth in Evaporated-Films," *Thin Solid Films*, vol. 226, pp. 196-201, 1993.
- [46] D. Vick, T. Smy, and M. J. Brett, "Growth behavior of evaporated porous thin films," *Journal of Materials Research*, vol. 17, pp. 2904-2911, 2002.
- [47] D. Vick, T. Smy, B. Dick, S. Kennedy, and M. J. Brett, "Growth behavior of engineered porous thin films - measurement and modeling," presented at Mat. Res. Soc. Symp., 2001.
- [48] I. Hodgkinson, Q. H. Wu, and J. Hazel, "Empirical equations for the principal refractive indices and column angle of obliquely deposited films of tantalum oxide, titanium oxide, and zirconium oxide," *Applied Optics*, vol. 37, pp. 2653-2659, 1998.
- [49] Paritosh and D. J. Srolovitz, "Shadowing effects on the microstructure of obliquely deposited films," *Journal of Applied Physics*, vol. 91, pp. 1963-1972, 2002.
- [50] I. Hodgkinson and Q. H. Wu, "Ion-beam control of thin-film microstructural columnar angle," *Modern Physics Letters B*, vol. 15, pp. 1328-1331, 2001.

- [51] B. Dick, M. J. Brett, and T. Smy, "Investigation of substrate rotation at glancing-incidence on thin-film morphology," *Journal of Vacuum Science & Technology B*, vol. 21, pp. 2569-2575, 2003.
- [52] D. Liu, F. Zhang, Z. H. Zheng, D. Z. Wang, and X. H. Liu, "Structural characteristics of rutile films prepared by direct deposition and neon ion beam assisted deposition," *Nuclear Instruments & Methods in Physics Research Section B-Beam Interactions with Materials and Atoms*, vol. 140, pp. 361-366, 1998.
- [53] B. Dick, M. J. Brett, T. Smy, M. Belov, and M. R. Freeman, "Periodic submicrometer structures by sputtering," *Journal of Vacuum Science & Technology B*, vol. 19, pp. 1813-1819, 2001.
- [54] J. C. Sit, D. Vick, K. Robbie, and M. J. Brett, "Thin film microstructure control using glancing angle deposition by sputtering," *Journal of Materials Research*, vol. 14, pp. 1197-1199, 1999.
- [55] J. Lintymer, N. Martin, J. M. Chappe, P. Delobelle, and J. Takadoum, "Nanoindentation of chromium zigzag thin films sputter deposited," *Surface & Coatings Technology*, vol. 200, pp. 269-272, 2005.
- [56] D. Vick, L. J. Friedrich, S. K. Dew, M. J. Brett, K. Robbie, M. Seto, and T. Smy, "Self-shadowing and surface diffusion effects in obliquely deposited thin films," *Thin Solid Films*, vol. 339, pp. 88-94, 1999.
- [57] M. Malac and R. F. Egerton, "Observations of the microscopic growth mechanism of pillars and helices formed by glancing-angle thin-film deposition," *Journal of Vacuum Science & Technology A*, vol. 19, pp. 158-166, 2001.
- [58] E. Main, T. Karabacak, and T. M. Lu, "Continuum model for nanocolumn growth during oblique angle deposition," *Journal of Applied Physics*, vol. 95, pp. 4346-4351, 2004.
- [59] T. Karabacak, J. P. Singh, Y. P. Zhao, G. C. Wang, and T. M. Lu, "Scaling during shadowing growth of isolated nanocolumns," *Physical Review B*, vol. 68, 2003.

- [60] M. Malac, R. F. Egerton, M. J. Brett, and B. Dick, "Fabrication of submicrometer regular arrays of pillars and helices," *Journal of Vacuum Science & Technology B*, vol. 17, pp. 2671-2674, 1999.
- [61] B. Dick, J. C. Sit, M. J. Brett, I. M. N. Votte, and C. W. M. Bastiaansen, "Embossed polymeric relief structures as a template for the growth of periodic inorganic microstructures," *Nano Letters*, vol. 1, pp. 71-73, 2001.
- [62] M. O. Jensen and M. J. Brett, "Periodically structured glancing angle deposition thin films," *IEEE Transactions on Nanotechnology*, vol. 4, pp. 269-277, 2005.
- [63] D. X. Ye, T. Karabacak, B. K. Lim, G. C. Wang, and T. M. Lu, "Growth of uniformly aligned nanorod arrays by oblique angle deposition with two-phase substrate rotation," *Nanotechnology*, vol. 15, pp. 817-821, 2004.
- [64] D. X. Ye, T. Karabacak, R. C. Picu, G. C. Wang, and T. M. Lu, "Uniform Si nanostructures grown by oblique angle deposition with substrate swing rotation," *Nanotechnology*, vol. 16, pp. 1717-1723, 2005.
- [65] Y. P. Zhao, D. X. Ye, G. C. Wang, and T. M. Lu, "Novel nano-column and nano-flower arrays by glancing angle deposition," *Nano Letters*, vol. 2, pp. 351-354, 2002.
- [66] M. Seto, K. Westra, and M. Brett, "Arrays of self-sealed microchambers and channels," *Journal of Materials Chemistry*, vol. 12, pp. 2348-2351, 2002.
- [67] A. T. Wu and M. J. Brett, "Sensing humidity using nanostructured SiO posts: Mechanism and optimization," *Sensors and Materials*, vol. 13, pp. 399-431, 2001.
- [68] A. T. Wu, M. Seto, and M. J. Brett, "Capacitive SiO humidity sensors with novel microstructures," *Sensors and Materials*, vol. 11, pp. 493-505, 1999.
- [69] D. X. Ye, Y. P. Zhao, G. R. Yang, Y. G. Zhao, G. C. Wang, and T. M. Lu, "Manipulating the column tilt angles of nanocolumnar films by glancing-angle deposition," *Nanotechnology*, vol. 13, pp. 615-618, 2002.
- [70] M. O. Jensen and M. J. Brett, "Embedded air and solid defects in periodically structured porous thin films," *Nanotechnology*, vol. 16, pp. 2639-2646, 2005.

- [71] M. O. Jensen and M. J. Brett, "Functional pattern engineering in glancing angle deposition thin films," *Journal of Nanoscience and Nanotechnology*, vol. 5, pp. 723-728, 2005.
- [72] M. O. Jensen and M. J. Brett, "Porosity engineering in glancing angle deposition thin films," *Applied Physics a-Materials Science & Processing*, vol. 80, pp. 763-768, 2005.
- [73] M. J. Colgan, B. Djurfors, D. G. Ivey, and M. J. Brett, "Effects of annealing on titanium dioxide structured films," *Thin Solid Films*, vol. 466, pp. 92-96, 2004.
- [74] P. Morrow, F. Tang, T. Karabacak, P. I. Wang, D. X. Ye, G. C. Wang, and T. M. Lu, "Texture of Ru columns grown by oblique angle sputter deposition," *Journal of Vacuum Science & Technology A*, vol. 24, pp. 235-245, 2006.
- [75] T. Karabacak, J. S. DeLuca, P. I. Wang, G. A. Ten Eyck, D. Ye, G. C. Wang, and T. M. Lu, "Low temperature melting of copper nanorod arrays," *Journal of Applied Physics*, vol. 99, 2006.
- [76] J. Arbiol, J. Cerda, G. Dezanneau, A. Cirera, F. Peiro, A. Cornet, and J. R. Morante, "Effects of Nb doping on the TiO₂ anatase-to-rutile phase transition," *Journal of Applied Physics*, vol. 92, pp. 853-861, 2002.
- [77] E. Barborini, G. Bongiorno, A. Forleo, L. Francioso, P. Milani, I. N. Kholmanov, P. Piseri, P. Siciliano, A. M. Taurino, and S. Vinati, "Thermal annealing effect on nanostructured TiO₂ microsensors by supersonic cluster beam deposition," *Sensors and Actuators B-Chemical*, vol. 111, pp. 22-27, 2005.
- [78] M. C. Carotta, M. Ferroni, D. Gnani, V. Guidi, M. Merli, G. Martinelli, M. C. Casale, and M. Notaro, "Nanostructured pure and Nb-doped TiO₂ as thick film gas sensors for environmental monitoring," *Sensors and Actuators B-Chemical*, vol. 58, pp. 310-317, 1999.
- [79] L. L. W. Chow, M. M. F. Yuen, P. C. H. Chan, and A. T. Cheung, "Reactive sputtered TiO₂ thin film humidity sensor with negative substrate bias," *Sensors and Actuators B-Chemical*, vol. 76, pp. 310-315, 2001.

- [80] Z. Dai, H. Naramoto, K. Narumi, and S. Yamaoto, "Epitaxial growth of rutile films on Si (100) substrates by thermal oxidation of evaporated titanium films in argon flux," *Journal of Physics-Condensed Matter*, vol. 11, pp. 8511-8516, 1999.
- [81] F. Edelman, A. Rothschild, Y. Komem, V. Mikhelashvili, A. Chack, and F. Cosandey, "Structure and properties of TiO₂ thin films for gas sensors," *Solid State Phenomena*, vol. 67-8, pp. 269-275, 1999.
- [82] M. Ferroni, V. Guidi, G. Martinelli, G. Roncarati, E. Comini, G. Sberveglieri, A. Vomiero, and G. D. Mea, "Coalescence inhibition in nanosized titania films and related effects on chemoresistive properties towards ethanol," *Journal of Vacuum Science & Technology B*, vol. 20, pp. 523-530, 2002.
- [83] P. I. Gouma, P. K. Dutta, and M. J. Mills, "Structural stability of titania thin films," *Nanostructured Materials*, vol. 11, pp. 1231-1237, 1999.
- [84] B. S. Jeong, J. D. Budai, and D. P. Norton, "Epitaxial stabilization of single crystal anatase films via reactive sputter deposition," *Thin Solid Films*, vol. 422, pp. 166-169, 2002.
- [85] V. Mikhelashvili and G. Eisenstein, "Optical and electrical characterization of the electron beam gun evaporated TiO₂ film," *Microelectronics Reliability*, vol. 41, pp. 1057-1061, 2001.
- [86] V. Mikhelashvili and G. Eisenstein, "Effects of annealing conditions on optical and electrical characteristics of titanium dioxide films deposited by electron beam evaporation," *Journal of Applied Physics*, vol. 89, pp. 3256-3269, 2001.
- [87] R. van de Krol and A. Goossens, "Structure and properties of anatase TiO₂ thin films made by reactive electron beam evaporation," *Journal of Vacuum Science & Technology A*, vol. 21, pp. 76-83, 2003.
- [88] J. Nair, P. Nair, F. Mizukami, Y. Oosawa, and T. Okubo, "Microstructure and phase transformation behavior of doped nanostructured titania," *Materials Research Bulletin*, vol. 34, pp. 1275-1290, 1999.

- [89] B. I. Lee, X. Y. Wang, R. Bhave, and M. Hu, "Synthesis of brookite TiO₂ nanoparticles by ambient condition sol process," *Materials Letters*, vol. 60, pp. 1179-1183, 2006.
- [90] A. Fahmi, C. Minot, B. Silvi, and M. Causa, "Theoretical-Analysis of the Structures of Titanium-Dioxide Crystals," *Physical Review B*, vol. 47, pp. 11717-11724, 1993.
- [91] B. S. Jeong, D. P. Norton, and J. D. Budai, "Conductivity in transparent anatase TiO₂ films epitaxially grown by reactive sputtering deposition," *Solid-State Electronics*, vol. 47, pp. 2275-2278, 2003.
- [92] M. Kosmulski, "The significance of the difference in the point of zero charge between rutile and anatase," *Advances in Colloid and Interface Science*, vol. 99, pp. 255-264, 2002.
- [93] H. Tang, K. Prasad, R. Sanjines, P. E. Schmid, and F. Levy, "Electrical and Optical-Properties of TiO₂ Anatase Thin-Films," *Journal of Applied Physics*, vol. 75, pp. 2042-2047, 1994.
- [94] A. L. Linsebigler, G. Q. Lu, and J. T. Yates, "Photocatalysis on TiO₂ Surfaces - Principles, Mechanisms, and Selected Results," *Chemical Reviews*, vol. 95, pp. 735-758, 1995.
- [95] H. Z. Zhang and J. F. Banfield, "Understanding polymorphic phase transformation behavior during growth of nanocrystalline aggregates: Insights from TiO₂," *Journal of Physical Chemistry B*, vol. 104, pp. 3481-3487, 2000.
- [96] F. Zhang, Z. H. Zheng, X. Z. Ding, Y. J. Mao, Y. Chen, Z. Y. Zhou, S. Q. Yang, and X. H. Liu, "Highly oriented rutile-type TiO₂ films synthesized by ion beam enhanced deposition," *Journal of Vacuum Science & Technology a-Vacuum Surfaces and Films*, vol. 15, pp. 1824-1827, 1997.
- [97] P. I. Gouma and M. J. Mills, "Anatase-to-rutile transformation in titania powders," *Journal of the American Ceramic Society*, vol. 84, pp. 619-622, 2001.
- [98] Y. Hu, H. L. Tsai, and C. L. Huang, "Phase transformation of precipitated TiO₂ nanoparticles," *Materials Science and Engineering a-Structural Materials Properties Microstructure and Processing*, vol. 344, pp. 209-214, 2003.

- [99] Y. Hu, H. L. Tsai, and C. L. Huang, "Effect of brookite phase on the anatase-rutile transition in titania nanoparticles," *Journal of the European Ceramic Society*, vol. 23, pp. 691-696, 2003.
- [100] C. C. Ting, S. Y. Chen, and D. M. Liu, "Structural evolution and optical properties of TiO₂ thin films prepared by thermal oxidation of sputtered Ti films," *Journal of Applied Physics*, vol. 88, pp. 4628-4633, 2000.
- [101] D. G. Syarif, A. Miyashita, T. Yamaki, T. Sumita, Y. Choi, and H. Itoh, "Preparation of anatase and rutile thin films by controlling oxygen partial pressure," *Applied Surface Science*, vol. 193, pp. 287-292, 2002.
- [102] D. Wicaksana, A. Kobayashi, and A. Kinbara, "Process Effects on Structural-Properties of TiO₂ Thin-Films by Reactive Sputtering," *Journal of Vacuum Science & Technology a-Vacuum Surfaces and Films*, vol. 10, pp. 1479-1482, 1992.
- [103] F. Zhang and X. H. Liu, "Effect of O₂ pressure on the preferred orientation of TiO₂ films prepared by filtered arc deposition," *Thin Solid Films*, vol. 326, pp. 171-174, 1998.
- [104] H. Alouach and G. J. Mankey, "Epitaxial growth of copper nanowire arrays grown on H-terminated Si(110) using glancing-angle deposition," *Journal of Materials Research*, vol. 19, pp. 3620-3625, 2004.
- [105] H. Alouach and G. J. Mankey, "Critical height and growth mode in epitaxial copper nanowire arrays fabricated using glancing angle deposition," *Applied Physics Letters*, vol. 86, 2005.
- [106] H. Alouach, H. Fujiwara, and G. J. Mankey, "Magnetocrystalline anisotropy in glancing angle deposited Permalloy nanowire arrays," *Journal of Vacuum Science & Technology A*, vol. 23, pp. 1046-1050, 2005.
- [107] F. Tang, T. Karabacak, P. Morrow, C. Gaire, G. C. Wang, and T. M. Lu, "Texture evolution during shadowing growth of isolated Ru columns," *Physical Review B*, vol. 72, 2005.
- [108] F. J. Humphreys, Matherly, M., *Recrystallization and related annealing phenomena*. New York: Pergamon, 1995.

- [109] Y. L. Brama, Y. Sun, S. R. K. Dangeti, and M. Mujahid, "Response of sputtered titanium films on silicon to thermal oxidation," *Surface & Coatings Technology*, vol. 195, pp. 189-197, 2005.
- [110] G. K. Kiema and M. J. Brett, "Effect of thermal annealing on structural properties and electrochemical performance of carbon films with porous microstructure," *Journal of the Electrochemical Society*, vol. 151, pp. E194-E198, 2004.
- [111] E. Schubert, J. Fahlteich, T. Hoche, G. Wagner, and B. Rauschenbach, "Chiral silicon nanostructures," *Nuclear Instruments & Methods in Physics Research Section B-Beam Interactions with Materials and Atoms*, vol. 244, pp. 40-44, 2006.
- [112] M. Suzuki, T. Ito, and Y. Taga, "Morphological stability of TiO₂ thin films with isolated columns," *Japanese Journal of Applied Physics Part 2-Letters*, vol. 40, pp. L398-L400, 2001.
- [113] Z. Dohnalek, G. A. Kimmel, D. E. McCready, J. S. Young, A. Dohnalkova, R. S. Smith, and B. D. Kay, "Structural and chemical characterization of aligned crystalline nanoporous MgO films grown via reactive ballistic deposition," *Journal of Physical Chemistry B*, vol. 106, pp. 3526-3529, 2002.
- [114] F. Tang, C. Gaire, D. X. Ye, T. Karabacak, T. M. Lu, and G. C. Wang, "AFM, SEM and in situ RHEED study of Cu texture evolution on amorphous carbon by oblique angle vapor deposition," *Physical Review B*, vol. 72, 2005.
- [115] T. Karabacak, P. I. Wang, G. C. Wang, and T. M. Lu, "Phase transformation of single crystal beta-tungsten nanorods at elevated temperatures," *Thin Solid Films*, vol. 493, pp. 293-296, 2005.
- [116] J. P. Singh, T. Karabacak, D. X. Ye, D. L. Liu, C. Picu, T. M. Lu, and G. C. Wang, "Physical properties of nanostructures grown by oblique angle deposition," *Journal of Vacuum Science & Technology B*, vol. 23, pp. 2114-2121, 2005.
- [117] J. Kim, Z. Dohnalek, and B. D. Kay, "Structural characterization of nanoporous Pd films grown via ballistic deposition," *Surface Science*, vol. 586, pp. 137-145, 2005.
- [118] D. L. Douglass and Vanlandu, J., "Structure and Morphology of Oxide Films During Initial Stages of Titanium Oxidation," *Acta Metallurgica*, vol. 14, pp. 491-&, 1966.

- [119] K. R. Lawless and A. T. Gwathmey, "The Structure of Oxide Films on Different Faces of a Single Crystal of Copper," *Acta Metallurgica*, vol. 4, pp. 153-163, 1956.
- [120] K. T. Lee, H. T. Jeong, J. A. Szpunar, and H. G. Kim, "The influence of substrate texture on the oxidation kinetics of copper," in *Textures of Materials, Pts 1 and 2*, vol. 408-4, *Materials Science Forum*, 2002, pp. 1019-1024.
- [121] C. C. Ting, S. Y. Chen, and D. M. Liu, "Preferential growth of thin rutile TiO₂ films upon thermal oxidation of sputtered Ti films," *Thin Solid Films*, vol. 402, pp. 290-295, 2002.
- [122] H. C. Chen, C. C. Lee, C. C. Jaing, M. H. Shiao, C. J. Lu, and F. S. Shieu, "Effects of temperature on columnar microstructure and recrystallization of TiO₂ film produced by ion-assisted deposition," *Applied Optics*, vol. 45, pp. 1979-1984, 2006.
- [123] S. H. Woo and C. K. Hwangbo, "Effects of annealing on the optical, structural, and chemical properties of TiO₂ and MgF₂ thin films prepared by plasma ion-assisted deposition," *Applied Optics*, vol. 45, pp. 1447-1455, 2006.
- [124] Q. N. Zhao, C. L. Li, and X. J. Zhao, "The effect of oxygen partial pressure and annealing on morphology and optical properties of TiO₂ films coated on glass," *Rare Metal Materials and Engineering*, vol. 33, pp. 309-312, 2004.
- [125] L. D. Birkefeld, A. M. Azad, and S. A. Akbar, "Carbon-Monoxide and Hydrogen Detection by Anatase Modification of Titanium-Dioxide," *Journal of the American Ceramic Society*, vol. 75, pp. 2964-2968, 1992.
- [126] P. K. Dutta, M. Frank, G. W. Hunter, and M. George, "Reactively sputtered titania films as high temperature carbon monoxide sensors," *Sensors and Actuators B-Chemical*, vol. 106, pp. 810-815, 2005.
- [127] P. K. Dutta, A. Ginwalla, B. Hogg, B. R. Patton, B. Chwioroth, Z. Liang, P. Gouma, M. Mills, and S. Akbar, "Interaction of carbon monoxide with anatase surfaces at high temperatures: Optimization of a carbon monoxide sensor," *Journal of Physical Chemistry B*, vol. 103, pp. 4412-4422, 1999.

- [128] X. Y. Du, Y. Wang, Y. Y. Mu, L. L. Gui, P. Wang, and Y. Q. Tang, "A new highly selective H-2 sensor based on TiO₂/PtO-Pt dual-layer films," *Chemistry of Materials*, vol. 14, pp. 3953-3957, 2002.
- [129] G. C. Mather, F. M. B. Marques, and J. R. Frade, "Detection mechanism of TiO₂-based ceramic H-2 sensors," *Journal of the European Ceramic Society*, vol. 19, pp. 887-891, 1999.
- [130] G. K. Mor, M. A. Carvalho, O. K. Varghese, M. V. Pishko, and C. A. Grimes, "A room-temperature TiO₂-nanotube hydrogen sensor able to self-clean photoactively from environmental contamination," *Journal of Materials Research*, vol. 19, pp. 628-634, 2004.
- [131] H. Tang, K. Prasad, R. Sanjines, and F. Levy, "TiO₂ Anatase Thin-Films as Gas Sensors," *Sensors and Actuators B-Chemical*, vol. 26, pp. 71-75, 1995.
- [132] S. A. Akbar and L. B. Younkman, "Sensing mechanism of a carbon monoxide sensor based on anatase titania," *Journal of the Electrochemical Society*, vol. 144, pp. 1750-1753, 1997.
- [133] G. S. Herman, Z. Dohnalek, N. Ruzycski, and U. Diebold, "Experimental investigation of the interaction of water and methanol with anatase-TiO₂(101)," *Journal of Physical Chemistry B*, vol. 107, pp. 2788-2795, 2003.
- [134] E. Comini, G. Sberveglieri, M. Ferroni, V. Guidi, and G. Martinelli, "Response to ethanol of thin films based on Mo and Ti oxides deposited by sputtering," *Sensors and Actuators B-Chemical*, vol. 93, pp. 409-415, 2003.
- [135] L. R. Skubal, N. K. Meshkov, and M. C. Vogt, "Detection and identification of gaseous organics using a TiO₂ sensor," *Journal of Photochemistry and Photobiology a-Chemistry*, vol. 148, pp. 103-108, 2002.
- [136] Z. Chen and C. Lu, "Humidity sensors: A review of materials and mechanisms," *Sensor Letters*, vol. 3, pp. 274-295, 2005.
- [137] C. Y. Lee and G. B. Lee, "Humidity sensors: A review," *Sensor Letters*, vol. 3, pp. 1-15, 2005.

- [138] K. D. Harris, A. Huizinga, and M. J. Brett, "High-speed porous thin film humidity sensors," *Electrochemical and Solid State Letters*, vol. 5, pp. H27-H29, 2002.
- [139] J. J. Steele, J. P. Gospodyn, J. C. Sit, and M. J. Brett, "Impact of morphology on high-speed humidity sensor performance," *Ieee Sensors Journal*, vol. 6, pp. 24-27, 2006.
- [140] K. D. Harris, J. R. McBride, K. E. Nietering, and M. J. Brett, "Fabrication of porous platinum thin films for hydrocarbon sensor applications," *Sensors and Materials*, vol. 13, pp. 225-234, 2001.
- [141] J. Lintymer, N. Martin, J. M. Chappe, P. Delobelle, and J. Takadoun, "Influence of zigzag microstructure on mechanical and electrical properties of chromium multilayered thin films," *Surface & Coatings Technology*, vol. 180-81, pp. 26-32, 2004.
- [142] D. Vick and M. J. Brett, "Conduction anisotropy in porous thin films with chevron microstructures," *Journal of Vacuum Science & Technology A*, vol. 24, pp. 156-164, 2006.